TECHNISCHE
UNIVERSITÄT
WIEN

VIENNA
UNIVERSITY OF
TECHNOLOGY

DISSERTATION

Simulation of Arterial Blood Flow with the Lattice Boltzmann Method

ausgeführt zum Zwecke der Erlangung des akademischen Grades eines
Doktors der technischen Wissenschaften unter der Leitung von

Ao.Univ.Prof. Dipl.-Ing. Dr. Felix Breitenecker
E101 - Institut für Analysis und Scientific Computing

eingereicht an der Technischen Universität Wien
bei der Fakultät für Mathematik und Geoinformation

von

Dipl.-Ing. Johannes Daniel Leitner

Matrikelnummer: 9725800
Blumauergasse 1c/3
1020 Wien

_____   _____
Datum   Unterschrift

Acknowledgement

First I want to thank the Austrian Research Centers for funding this work and particulary Siegfried Wassertheurer who supervised the work over the last three years and always helped with constructive advices.

Special thanks are regarded to Professor Felix Breitenecker who supported this thesis and has made scientific work even more interesting by traveling to conferences from Odessa (east) to Bilbao (west) or by holding the yearly instructive summer school in the Tuscany.

Furthermore I want to thank my family and friends for their encouragement, especially Bella for reading and correcting the work as well as my co-workers at Biomedical Engineering for the good company and their tremendous brain-power.

Kurzfassung

Da kardiovaskuläre Erkrankungen die häufigste Todesursache in den westlichen Industriestaaten sind, wird auf diesem Gebiet bereits intensiv geforscht. Diese Arbeit beschäftigt sich mit der Simulation von Blutfluss in den großen Arterien, wobei besonders auf die lokalen Strömungseigenschaften des dynamischen Flusses eingegangen wird. Bei den charakteristischen Geschwindigkeiten und Längen, die dabei auftreten, ist es möglich, Blut als eine Newtonsche Flüssigkeit zu betrachten. Solche Flüssigkeiten können mit den Navier-Stokes Gleichungen beschrieben werden. Diese Gleichungen müssen im Allgemeinen numerisch gelöst werden, was anhand der Lattice Boltzmann Methode geschieht.

Lattice Boltzmann Methoden sind explizite numerische Verfahren, die durch einen Bottom-up-Ansatz hergeleitet werden können und häufig in der Strömungsmechanik zur Anwendung kommen. Ziel dieser Arbeit ist es, diese Methode auf den kardiovaskulären Bereich anzuwenden. Dafür muss das Verfahren um eine neue Randbedingung erweitert werden, welche die Elastizität der Arterienwände beschreibt. Dadurch ist es möglich, die Methode in der Blutflusssimulation einzusetzen, wobei auf die in technischen Anwendungen unüblichen Reynoldszahlen, auf die Elastizität der Gefäße und auf die kompliziert verzweigte Geometrie Rücksicht genommen wird.

Die vorgestellten Verfahren und Randbedingungen wurden in Java implementiert und außerdem wurde eine Softwareumgebung erstellt, die den Benutzer in den folgenden Aufgaben unterstützt: Zunächst bei der Erfassung der Daten, wobei geometrische Randwerte patientenspezifisch durch Magnet

Resonanz Angiographie gewonnen werden sollen. Weiters beim Platzieren beliebiger Randwerte, vor allem von geeigneten dynamischen Ein- und Ausflüssen und anschließend bei der Interpretation und Visualisierung der Ergebnisse. Dabei können die Ergebnisse entweder nach Matlab exportiert werden oder mit direkter Volumsvisualisiserung oder mit geometrie-basierten Verfahren dargestellt werden.

Abstract

Cardiovascular diseases are the most frequent cause of death in the western industrial countries, therefore recently a lot of research is done in this area. This work focuses on blood flow simulation in large arteries where the local properties of the dynamic flow are under investigation. The characteristic velocities and lengths that thereby occur make it possible to approximate blood as a Newtonian fluid. Therefore the flow can be described by the Navier-Stokes equations. These equations in general must be calculated numerically, which is done with the Lattice Boltzmann method.

Lattice Boltzmann methods are explicit numerical schemes that are derived with a bottom-up approach and are widely used in fluid mechanical applications. The aim of this work is to apply this method to the cardiovascular domain. For this reason the procedure is extended for a new boundary condition, which describes the properties of elastic vessel walls. Hence it is possible to use the method in blood flow simulation with regard to relevant Reynolds numbers, elasticity and the complex branching of the vessels.

The proposed methods and boundary conditions have been implemented in Java and a software environment has been created supporting the user with the following tasks: First with data acquisition, where geometrical boundary conditions shall be derived patient specific from magnetic resonance angiography. Further with the setting of arbitrary boundary conditions, particularly with feasible in- and outflow profiles, and finally with the interpretation and visualization of the results. The results can be either exported to Matlab or visualized by direct volume visualization or geometry-based methods.

Contents

Chapter 1

Introduction

The chapter gives a short survey to physiology, modeling and simulation. First a short description of the cardiovascular system is given, then the fundamental terms of simulation and modeling are introduced. Finally the objectives and requirements of blood flow simulation are presented, preliminary works are examined and the aim of this work is described in detail.

1.1 Physiology of the arterial system

The cardiovascular system transports blood to the cells to provide them with oxygen and nutrients as well as to dispose pollutants like carbon dioxide. The circulation is extremely powerful, in example the heart beats on average 115200 times in one day transporting approximately 7200 liters of blood. In this section only a short introduction can be given, for a complete survey on the topic the reader may refer to [1].

The heart is the driving force of blood flow. It consists of four chambers, two pairs respectively each consisting of atrium and ventricle, see figure 1.1. From the left ventricle the blood is pumped into the aorta and enters the systemic cycle. From the right ventricle it is pumped into the pulmonary cycle. From the heart the blood branches to the arterioles, which are small vessels with a diameter between 20-100 μm, and passes on to the capillaries where the mass transfer occurs. In the systemic cycle oxygen and nutrients are delivered and carbon dioxide is loaded, while in the pulmonary cycle the blood is loaded with oxygen and the carbon dioxide is disposed. After this exchange the blood returns through the veins where the oxygen-rich blood from the pulmonary cycle enters the left atrium and the carbon dioxide-rich blood enters the right atrium.

The cardiovascular system has a blood volume of approximately five liters. The veins hold the majority of the blood, while the arteries' high pressure system holds only a small proportion [2], see table 1.1.

	pressure (mmHg)	blood volume (ml)
arterial systemic	100	1000
veneous systemic	2	3500
arterial pulmonar	15	100
veneous pulmonar	5	400

Table 1.1: *Pressure in the arterial and venous system*
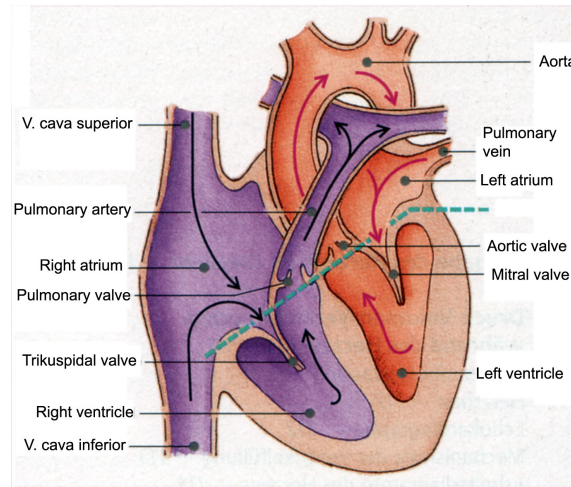
Figure 1.1: *The heart [3]*

In the following section some aspects are described in more detail. Starting point is the heart which is the source of blood flow. Then the systemic arteries are examined, which are important concerning cardiovascular diseases. Subsequently the physiology of blood is described and in the last section the most common cardiovascular diseases are summarized.

1.1.1 Heart

The heart pumps blood through the vascular system with contraction by periodic stimulation of its muscles. Its septum divides it into two sections each containing two chambers the atrium and the more muscular ventricle, see figure 1.1. During the expansion of the heart, the diastolic phase, in each cycle the two ventricles are filled with blood from the left and right atria respectively. In the systolic phase the heart contracts. The mitral and trikuspidal valve prohibit a backflow into the atrium. Thus the blood has to exceed from the left ventricle into the aorta and from the right ventricle into the pulmonary artery. The ejection continues until the flow decelerates and the aortic and pulmonary valves close. The sinus node controls the synchronous contraction of the ventricles. The cardiac cycle takes approximately 0.7 s, the systole endures between 0.2-0.3 s and the diastole 0.5-0.7 s.
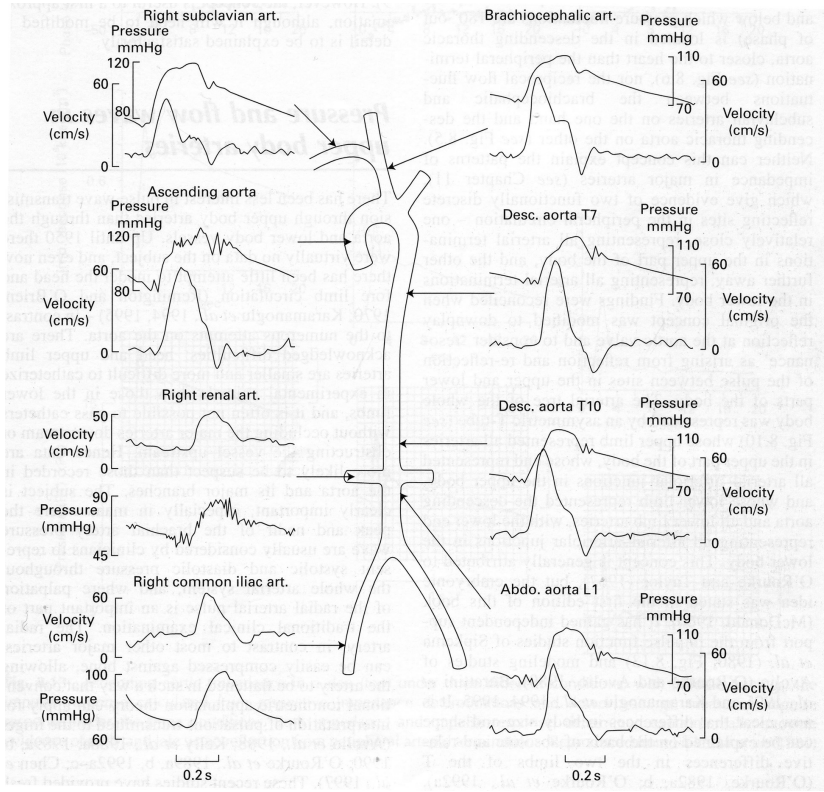
Figure 1.2: *Velocity and pressure over one cardiac cycle in the main arteries [4].*

1.1.2 Systemic arteries

The blood is pumped from the heart into the aorta. In the aorta the pressure fluctuation is approximately between 70 mmHg and 110 mmHg. This is much less than in the ventricle where the pressure fluctuates approximately between 0 mmHg and 120 mmHg. This is possible because of the elasticity of the aorta which is responsible for the so called Windkessel effect. The Windkessel effect is often described with the analogy to a hand pumped fire engine. The fireman pumps water into a air chamber with periodic injections at high pressure. The chamber has a high mean pressure and therefore the water streams out in a steady flow.

A schematic illustration of the main branches of the aorta with velocity and pressure profiles is given in figure 1.2. Except for the aorta and iliac all large
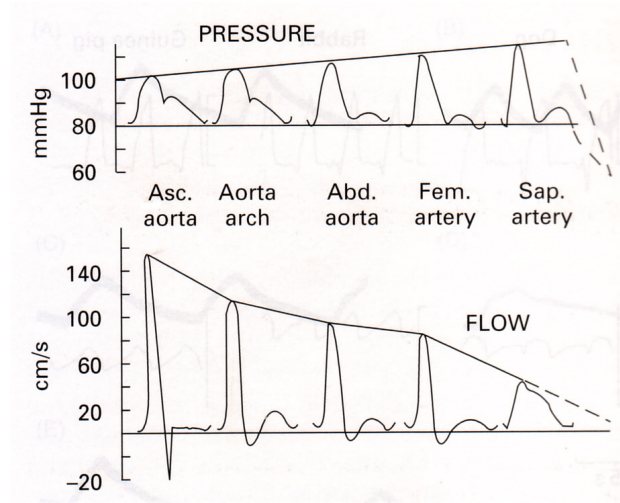
Figure 1.3: *Pressure and velocity profiles moving away from the heart [4].*

arteries are curved and branched in complicated ways. Only relatively few straight segments exist where the fluid mechanics of long tubes apply [5]. This can be a problem in blood flow simulation because the inflow profile is not known and must be chosen in a realistic way. This problem will be discussed in chapter 4.1.2. Going down the vessel tree the mean pressure stays approximately the same in the large arteries, while the maxima of the pressure profiles increase and the minima decrease. The flow oscillation on the other hand diminishes which is an effect of the reflection in small peripheral vessel, see figure 1.3.

1.1.3 Blood

Blood is a suspension of formed elements in plasma. Those elements make up to 45% of the blood and are red cells, white cells and platelets. The majority are the red cells which mainly influence the mechanical properties of blood. They can be described as elastic biconcave discs with a diameter of 8 μm and a thickness of 1 μm at the center and 2-3 μm at the edge. The white blood cells are larger than the red blood cells. Because they are far less in number than the red cells they do not effect the mechanical properties of

blood. Platelets are rounded cells with a diameter of 2-4 μm. They are not important for mechanical properties of blood but they play a significant role in blood clotting and in the later stages of the development of arteriosclerosis. Plasma itself is a suspension of large molecules. It can be regarded as a Newtonian fluid on the characteristic scales of motion and shear stress that are encountered in the blood vessels.

Blood can be assumed as a homogeneous fluid when the microstructure of blood is very small in comparison to the characteristic length under investigation. In this case blood can be described with the Navier-Stokes equations. This approximation is often used in large vessels, commonly it is assumed that the suspension has a density of 1.052 $\frac{g}{cm^3}$ and a kinematic viscosity of 0.04 $\frac{cm^2}{s}$ [5].

1.1.4   Cardiovascular diseases

Cardiovascular diseases are the most frequent cause of death in the western industrial countries [6] [7]. In this section the most common diseases are summarized.

- Hypertension: The definition of the WHO of hypertension is that the blood pressure at the arm at the height of the heart is higher than 160 mmHg in the systole or 95 mmHg in the diastole. Persistent hypertension is an important risk factor for cardiovascular diseases. It can lead to strokes, heart failure and arterial aneurysm and is a leading cause of chronic renal failure.

- Thrombosis and embolism: Thrombosis is the generation of a blood clot on a vessel wall. The blood clot grows fast and then closures the vessel. The blood clot is then called a thrombus. When the thrombus detaches it is transported through the vessels until it again blocks a vessel. The transported blood clot is called embolus. One of the most common recognized scenarios is called coronary thrombosis, where a coronary artery is blocked causing myocardial infarction commonly called a heart attack.

- Atherosclerosis: The disease is affecting arterial blood vessels and is caused by the formation of multiple plaques within the arteries. As a result the artery becomes less elastic, which weakens the Windkessel effect and therefore burdens the whole cardiovascular system. Another problem of atherosclerosis is that the atheromatous plaques can lead to plaque ruptures and stenosis, which is a narrowing of the arteries. This causes either insufficient blood supply to the organs or an increased blood pressure when the same blood volume has to be transported through the narrowed vessels.

1.2   Modeling and simulation

In this section basic terms of modeling and simulation will be introduced and its appliance in medicine will be discussed. For a more detailed presentation on modeling and simulation the reader may refer to [8] and [9].

Simulation is the replication of a dynamic process for gaining insights that can be transferred to the real world. Therefore a fragment of reality, a system, is described with a model. A system is a set of objects which are connected by interdependence and interaction. According to this a model is the description of a concrete system and a mathematical model is the description of a concrete system in terms of equations. The model is then implemented in a suitably programming language. In a stricter sense simulation is the experimentation with a computer model used to get insights about the properties of the system. Possible objectives are predictions of the time behavior of the system or the detection and analysis of system properties.

Modeling and simulation in medicine is becoming increasingly important and is applied to many different areas in medicine. In the following some of the applications are summarized.

- Prediction of the course of a disease: If the time behavior of a disease can be predicted by computer simulation a computer aided treatment planning is possible.

- Prediction of the effects of an operation: The effects on operational interferences are simulated which can enable a preoperation planning.

- Teaching: Experiments with a model can help to understand complex coherence.

- Prediction of measurement: Many significant parameters cannot be measured directly, but sometimes it is possible to calculate those parameters using simulation.
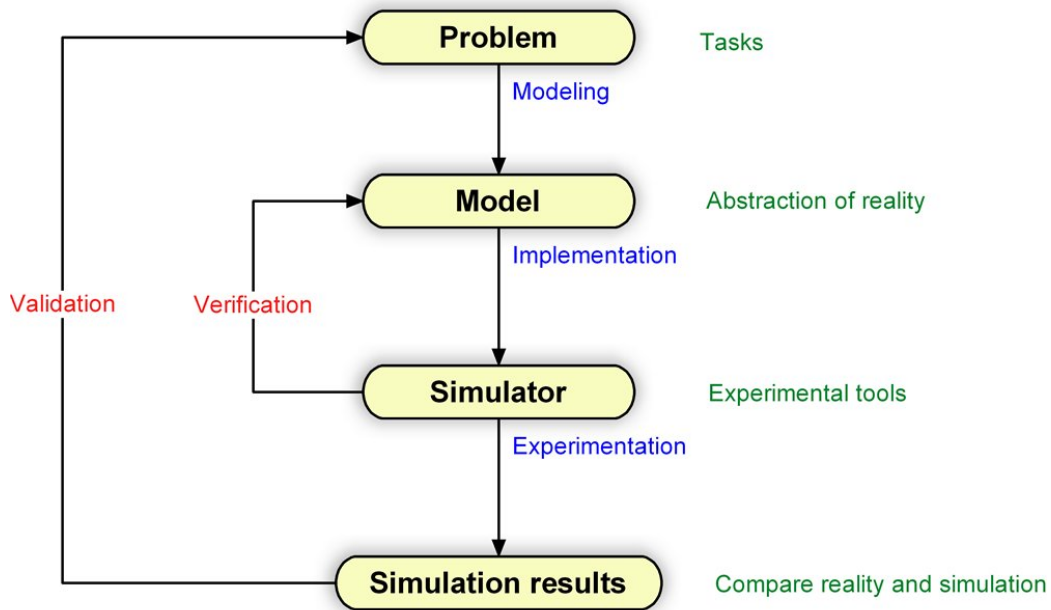
Figure 1.4: *Modeling as an iterative process*

The construction of a model takes several steps and is an iterative process, see figure 1.4. First the system under investigation must be restricted. As few characteristics of the system as possible should be used to describe the task. If too many characteristics are considered the system becomes too complex and its description more difficult. On the other hand the inclusion of too little characteristics causes that the system does not capture essential system properties. The complexity of the system depends on the one hand of the complexity of the system under investigation and on the other hand on the level of detail which is needed for the predetermined task.

Modeling and simulation is mostly performed on computers, hence a huge amount of computer codes exist to support several tasks that occur in the method simulation. These tasks are [10]:

1. Formulation of the problem

2. Data collection and data acquisition

3. Mathematical modeling

4. Computer implementation

5. Model validation

6. Model identification

7. Experiments with the model

8. Representation of results

9. Interpretation of results

Experimentations with the model (7) are usually in the time domain if the system under investigation is dynamic. For computer programs different terms are used showing which tasks are supported. A Simulation Software or a Simulation Language support the steps (4, 7, 8). A Simulator supports also the data acquisition and the modeling process, thus (2, 3, 4, 7, 8). A Simulation System additionally supports identification, thus (2, 3, 4, 6, 7, 8). Finally a Simulation Environment adds features for validation, thus supporting almost every step (2, 3, 4, 5, 6, 7, 8).

1.3   Problem formulation

In this section the main objectives of the thesis are given and the main tasks in the development of a feasible blood flow simulator are presented. A short overview on previous works is given and a link to those models is established.

1.3.1   Motivation

As pointed out in section 1.1.4 nowadays a big amount of deaths in industrial countries can be ascribed to diseases of the cardiovascular system like atherosclerosis, hypertension or cardiac insufficiency. Therefore a lot of research is done in this area trying to comprehend the complex physiological behavior of the cardiovascular system.

In recent years computer performance increased enormously making it possible to calculate flows in three dimensions in arbitrary geometries which are derived from tomographic images. The simulation of blood flow in these realistic geometries can help to understand the causes of certain diseases, predict their influence on the cardiovascular system and simulate the effects of surgery. Some interesting applications of blood flow simulation in three dimensions are:

- Vascular surgery planning: The effects of surgical procedures as shunts, artery bypasses [11] or stents [12] are simulated. The aim is to find an optimal treatment.

- Arteriosclerosis: It is well known that the formation of plaque is related to wall shear stress, see for example [13] [14] [15]. On the one hand areas of risk can be determined by examining the flow fields. On the other hand the effects of arteriosclerosis can be examined in the simulation.

- Stenosis of the vascular type are often associated with turbulent flow over the narrowed blood vessel. The local flow field within the stenosis can be examined [16].

- Effect of compliance: The elasticity of the vessel walls alters the speed of wave propagation and therefore the flow and pressure fields in the arteries [17] [18] . The influence of elasticity on the flow and shear stress patterns is of major interest.

1.3.2 Simulation on different scales

A lot of research concerning the cardiovascular system has been done at the Austrian Research Centers over the last years. It has started with a program simulating static arterial blood flow in the human arterial system by Martin Suda [19] [20]. This model has been extended by Christian Almeder to a dynamic model with a rough network of the whole body existing of approximately 140 arteries [21]. Michael Wibmer has worked on finite volume methods for describing the wave propagation through this arterial network [22]. These models have been extensively examined by Johannes Kropf [23] and extended for new termination models at the cut off from the arterial tree [24].

The models presented above are one dimensional global models describing the whole cardiovascular system. In this work a model for local blood flow in three dimensions will be proposed. The global models are extremely powerful and can simulate a multitude of different physiological sceneries. For this reason it is important that a connection between the two approaches is established [25]. The data from the one dimensional models can be used as an input to the three dimensional model. Therefore in- and outflow profiles for the three dimensional model are derived from pressure or flow contours from the one dimensional model, see figure 1.5.

This approach tries to combine the benefits of both methods. Global aspects can be examined with the one dimensional model. When the local mechanical properties of blood flow are of interest the full three dimensional flow is calculated in a certain region. The geometry of this region of interest can be derived from patient specific tomographic data. In the next section the
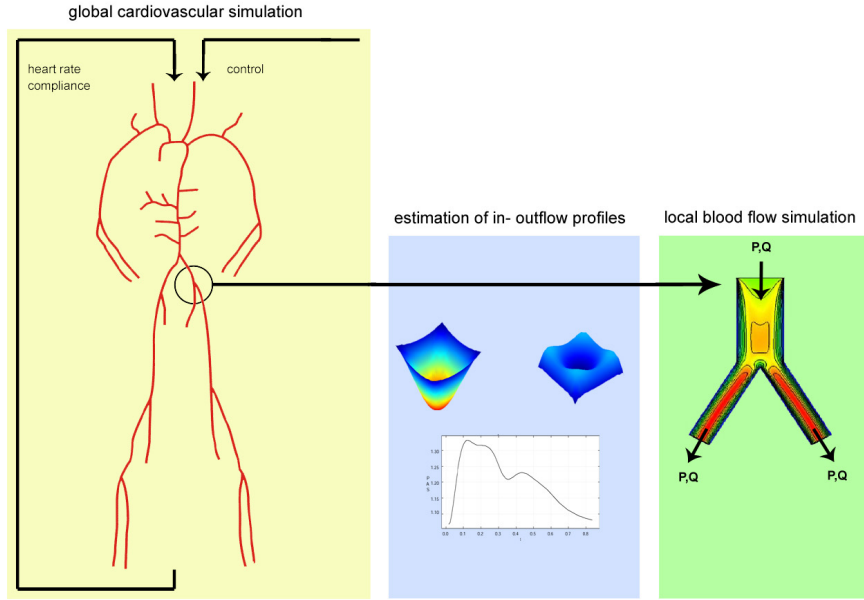
Figure 1.5: *The connection between local and global models in blood flow simulation*

requirements on a simulation environment calculating the three dimensional flows are discussed.

1.3.3   A simulator for blood flow

In this work a simulation environment has been developed simulating blood flow in three spatial dimension with patient specific geometrical boundary conditions and in- and outflow conditions from global cardiovascular models. The software environment supports the user in the following steps:

- Data acquisition. From tomographic images which are usually exported in the DICOM format a lattice is generated, which is a representation of the geometrical boundaries and which is used for computation.

- Experiments. Different flows can be simulated by the choice of different in- and outflow profiles. These flow profiles can be taken either from

global cardiovascular models or from measured data.

- Changing the predetermined geometry: It is possible to alter the geometry to investigate the effects on the flow and pressure fields. Of special interest is the placement of a shunt which is a major intervention changing the pressure ratio of the whole domain. Goal is to find the optimal size and position for a shunt.

- The effects of elasticity can be investigated by the usage of the boundary condition describing elastic walls [26] as described in section 4.2.

- Representation and interpretation: The results of the simulation can be visualized and analyzed in different ways. During the simulation the flow is visualized with direct volume methods like maximum intensity and first hit projection. Additionally the results of the simulation can be examined afterwards with geometry based methods like stream ribbons or the flow can be animated with particle based representations.

In the following chapter the fluid dynamics of blood flow will be investigated. Main focus of this work lies in the numerical treatment of the occurring Navier-Stokes equations. This topic is examined in the next two chapters. First the Lattice Boltzmann methods are introduced and second feasible boundary conditions for blood flow simulation are developed. Finally the implementation of these methods are discussed and the resulting software is presented.

Chapter 2

Fluid dynamics

In this work blood flow is modeled with the aid of the Navier-Stokes equations. These equations govern the behavior of fluids, which are liquids and gases. The main difference between liquids and gases is that gases can be easily compressed, whereas liquids are almost incompressible.

The first section of this chapter is an introduction to fluid dynamics. It provides a short explanation of the governing physical equations, which are used in the following chapters. The main focus lies on the incompressible Navier-Stokes equations and its derivation. Topics which can be neglected for blood flow simulation like thermodynamics are skipped.

The second section shows in which way the Navier-Stokes equations apply to blood flow simulation and describes the kinematic similarity of flows on different scales. Further it presents two important analytical solutions of the Navier-Stokes equations: Poiseuille and Womersley flows. They can be used to validate hemodynamical models and to gain insight about basic laws of hemodynamics.

2.1 Basic equations of fluid dynamics

First fundamental terms of fluid dynamics will be introduced. Then the Euler and Navier-Stokes equations will be derived from more basic physical principles. The most important tensors like the stress tensor and the momentum flux tensor will be explained in detail because they are needed for numerical considerations in the following chapters. The introduction is very compact, a short but complete instruction to fluid dynamics can be found in [27]. More detailed work about fluid dynamics are in example [28] or especially for incompressible fluids [29].

2.1.1 Fundamental terms

A physical flow is described with a velocity field $\mathbf{u} = \mathbf{u}(\mathbf{x}, t)$ a pressure field $p = p(\mathbf{x}, t)$ and a density distribution $\rho = \rho(\mathbf{x}, t)$. Thus at a time t and a position $\mathbf{x}$ in space, a certain velocity vector and the scalar values of pressure and density are given. With a spatial domain $\Omega \subseteq \mathbb{R}^N$ and temporal domain $I \subseteq \mathbb{R}$ these mappings are given by

$$
\begin{aligned}
\mathbf{u} &: \Omega \times I \to \mathbb{R}^N \\
p &: \Omega \times I \to \mathbb{R} \\
\rho &: \Omega \times I \to \mathbb{R}.
\end{aligned}
\tag{2.1}
$$

Figure 2.1 shows a velocity field and figure 2.2 the corresponding pressure field of a so called 'Von Karman vortex street' behind an obstacle describing an incompressible fluid in two spatial dimensions ($N = 2$).

A special case occurs when a flow does not change over time. Those flows are called steady flow, thus

$$
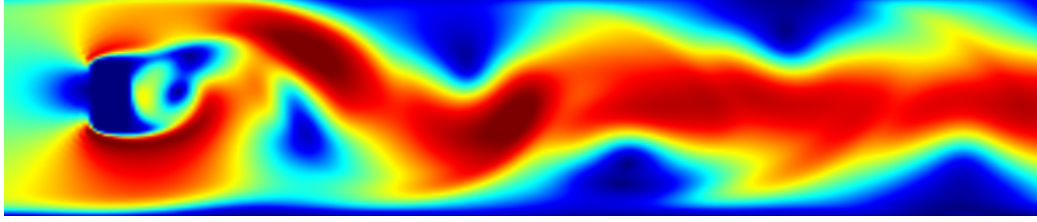\frac{\partial \mathbf{u}}{\partial t} = 0.
\tag{2.2}
$$

Figure 2.1: *The velocity field of a Von Karman vortex street, the colors represent* $|\mathbf{u}(\mathbf{x}, t_0)|$ *at a fixed time* t_0
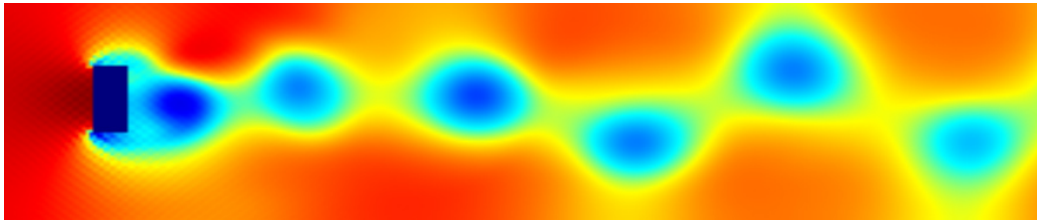
Figure 2.2: *The pressure field of a Von Karman vortex street, the colors represent* $p(\mathbf{x}, t_0)$ *at a fixed time* t_0

An example of a steady flow is the Poiseuille flow, which is discussed in section 2.2.3.

For the visualization of two dimensional flows stream lines are often used, see figure 2.3. A stream line is a curve $\mathbf{x}(s)$ that has the same tangential direction as the velocity field at a fixed time t_0, meaning

$$
\begin{aligned}
\mathbf{x} \quad &: \quad I \subseteq \mathbb{R} \to \mathbb{R}^N \\
\frac{\partial}{\partial s} \mathbf{x}(s) \quad &= \quad \mathbf{u}(\mathbf{x}(s), t_0), \quad \forall s \in I,
\end{aligned}
\tag{2.3}
$$

where s is the parameter along the stream line.

In the governing equations of fluid dynamics the substantial derivative is of major importance. It is defined as

$$
\frac{D}{Dt} f(\mathbf{x}, t) = \frac{d}{dt} f(\mathbf{x}(t), t)
\tag{2.4}
$$
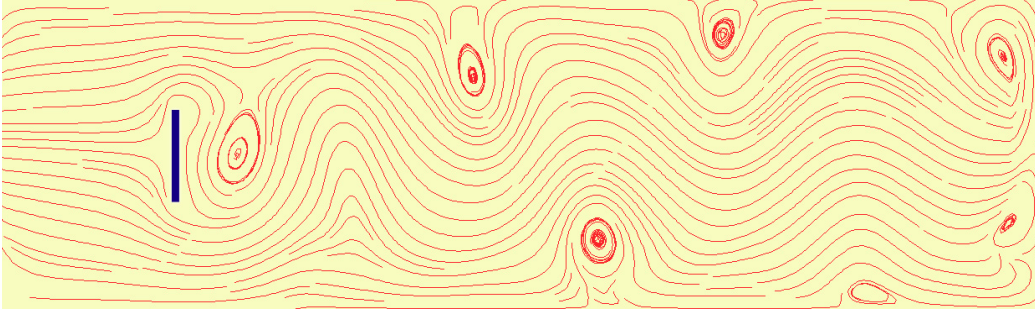
Figure 2.3: *Stream lines of a flow field* $\mathbf{u}(\mathbf{x}, t_0)$ *at a fixed time* t_0

with $\mathbf{x} : I \subseteq \mathbb{R} \to \mathbb{R}^N$ and an arbitrary map $f : \Omega \times I \to \mathbb{R}^N$. If the chain rule in several variables is applied to formula 2.4 and the fact that $\dot{\mathbf{x}} = \mathbf{u}$ is used, it follows that

$$\frac{Df}{Dt} = \frac{\partial f}{\partial t} + (\mathbf{u} \cdot \nabla)f. \tag{2.5}$$

In the case of steady flow the substantial derivative describes the change along a stream line. In time dependent flows it can be interpreted as the change while following the fluid. As a result the acceleration in a fluid is given by

$$\frac{D\mathbf{u}}{Dt} = \frac{\partial \mathbf{u}}{\partial t} + (\mathbf{u} \cdot \nabla)\mathbf{u} \tag{2.6}$$

The following two terms often arise in fluid dynamics:

- The term

$$(\mathbf{u} \cdot \nabla)f = 0 \tag{2.7}$$

  indicates that f is constant along a stream line.

- The term

$$\frac{Df}{Dt} = 0 \tag{2.8}$$

Engineering		Fluid Dynamics
conservation of mass	$\Rightarrow$	continuity equation
Newton's second law	$\Rightarrow$	momentum equation
laws of thermodynamics	$\Rightarrow$	energy equation

Table 2.1: *Terms of engineering and the corresponding terms in fluid dynamics*

expresses that f is constant over time in every point.

This section has described fundamental terms which frequently occur in fluid dynamics. The following sections will describe the most important equations which govern the behavior of fluids.

2.1.2 Reynolds Transport Theorem

The Reynolds transport theorem is fundamental in formulating the laws of fluids and is used to derive them from basic laws of engineering and physics, see table 2.1.

The Reynolds transport theorem for an arbitrary extensive property f is given by

$$\frac{D}{Dt} \int_{\Omega_t} f(\mathbf{x}, t) d\mathbf{x} = \int_{\Omega_t} \{\frac{\partial}{\partial t} f + \nabla \cdot (f\mathbf{u})\}(\mathbf{x}, t) d\mathbf{x}, \qquad (2.9)$$

where Ω_t is a time dependent control volume. To show that this equation is valid, first the time dependent domain Ω_t is transformed to a time independent domain Ω_0:

$$\frac{D}{Dt} \int_{\Omega_t} f(\mathbf{x}, t) d\mathbf{x} = \frac{D}{Dt} \int_{\Omega_0} \{f|J|\}(\mathbf{y}, t) d\mathbf{y}, \qquad (2.10)$$

where

$$J = \left(\frac{\partial g_\alpha}{\partial x_\beta}\right)_{\alpha\beta} \quad \text{with} \quad \alpha, \beta = 1 \dots N \qquad (2.11)$$

is the Jacobian of the transformation with

$$y_\alpha(t) = g_\alpha(\mathbf{x}, t). \tag{2.12}$$

On the time independent domain Ω_0 integration and differentiation can be interchanged and the differentiation is performed:

$$\frac{D}{Dt} \int_{\Omega_0} \{f|J|\}(\mathbf{y}, t) d\mathbf{y} = \int_{\Omega_0} \{\frac{Df}{Dt}|J| + f\frac{D|J|}{Dt}\}(\mathbf{y}, t) dy. \tag{2.13}$$

With

$$\frac{D|J|}{Dt} = |J|(\nabla \cdot \mathbf{u}) \tag{2.14}$$

the integral can be transformed backwards to the time dependent domain:

$$\int_{\Omega_0} \{\frac{Df}{Dt}|J| + f|J|(\nabla \cdot \mathbf{u})\}(\mathbf{y}, t) d\mathbf{y} =$$
$$\int_{\Omega_t} \{\frac{Df}{Dt} + f(\nabla \cdot \mathbf{u})\}(\mathbf{x}, t) d\mathbf{x}. \tag{2.15}$$

Using the substantial derivative (equation 2.5) it follows that

$$\int_{\Omega_t} \{\frac{Df}{Dt} + f(\nabla \cdot \mathbf{u})\}(\mathbf{x}, t) d\mathbf{x} =$$
$$\int_{\Omega_t} \{\frac{\partial f}{\partial t} + (\mathbf{u} \cdot \nabla)f + f(\nabla \cdot \mathbf{u})\}(\mathbf{x}, t) d\mathbf{x} =$$
$$\int_{\Omega_t} \{\frac{\partial f}{\partial t} + \nabla \cdot (f\mathbf{u})\}(\mathbf{x}, t) d\mathbf{x}, \tag{2.16}$$

which proves the Reynolds transport theorem (equation 2.9).

This is a pure formal proof of the transport theorem. A nice physical interpretation of the theorem can be given by applying the divergence theorem on the last term of the Reynolds transport theorem:

$$\int_{\Omega_t} \{\nabla \cdot (f\mathbf{u})\}(\mathbf{x}, t) d\mathbf{x} = \int_{\partial\Omega_t} \{f\mathbf{u} \cdot \mathbf{n}\}(\mathbf{s}, t) d\mathbf{s}. \tag{2.17}$$
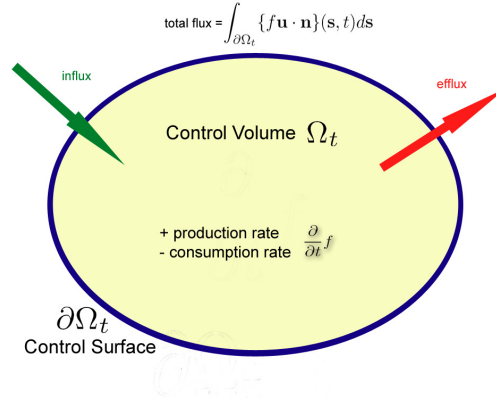
Figure 2.4: *Influx and efflux of a control volume*

Thus the transport theorem can be stated as:

$$\frac{D}{Dt}\int_{\Omega_t} f(\mathbf{x},t)d\mathbf{x} = \int_{\Omega_t}\{\frac{\partial}{\partial t}f\}(\mathbf{x},t)d\mathbf{x} + \int_{\partial\Omega_t}\{f\mathbf{u}\cdot\mathbf{n}\}(\mathbf{s},t)d\mathbf{s}. \qquad (2.18)$$

This equation is called the Reynolds transport theorem in general form. It can be read as rate of change of f following the fluid equals the rate of change within the volume plus the net flux of f through the surface $\partial\Omega_t$, see figure 2.4.

The Reynolds transport theorem applies to an arbitrary extensive property of a fluid. It is used in the two following sections first to derive the continuity equation, where it is applied to the density of the fluid, and secondly the momentum equation, where it is applied to the fluids momentum.

2.1.3 Continuity equation

The mass of a fluid over a time dependent area Ω_t is the integral over its density. The mass of the fluid stays the same over time, hence

$$const = \int_{\Omega_0} \rho(\mathbf{x},0)d\mathbf{x} = \int_{\Omega_t} \rho(\mathbf{x},t)d\mathbf{x} \qquad (2.19)$$

for all $t \geq 0$. The substantial derivative (equation 2.4) of equation 2.19 and the use of the Reynolds transport theorem shows that

$$0 = \int_{\Omega_t} \{\frac{\partial}{\partial t}\rho + \nabla \cdot (\rho\mathbf{u})\}(\mathbf{x}, t)d\mathbf{x} \qquad (2.20)$$

for all $t \geq 0$ and for arbitrary areas Ω_t. Thinking of small arbitrary areas Ω_t it is clear that the integrand must be zero, thus it follows that

$$\frac{\partial}{\partial t}\rho + \nabla \cdot \rho\mathbf{u} = 0. \qquad (2.21)$$

This equation is called 'continuity equation for compressible fluids'. For incompressible fluids meaning $\rho_{const} = \rho(\mathbf{x}, t)$ the equation simplifies to

$$\nabla \cdot \mathbf{u} = 0. \qquad (2.22)$$

This is the 'continuity equation for incompressible fluids'.

2.1.4   Momentum Equation

The momentum of a rigid body is its mass times its velocity. The momentum of a fluid is defined over an area Ω_t as

$$\mathbf{j}(t) = \int_{\Omega_t} \{\rho\mathbf{u}\}(\mathbf{x}, t)d\mathbf{x}. \qquad (2.23)$$

The second law of Newton states that the change of momentum in respect to time equals the forces acting on the fluid. Forces can be divided into body forces and surface forces:

- Body forces can be expressed by force per density, thus on an area Ω_t the body force is given by

$$\text{body force} = \int_{\Omega_t} \{\rho\mathbf{g}\}(\mathbf{x}, t)d\mathbf{x}. \qquad (2.24)$$
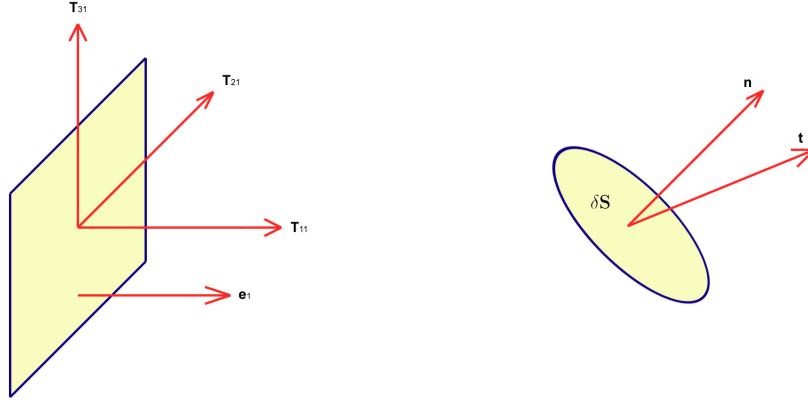
A common example is the gravitational force.

Figure 2.5: *The three components of the stress tensor $\sigma_{\alpha\beta}$ (left), the stress tensor* **t** *of a surface element* **dS** *(right)*

- Surface forces are forces that act on a surface of the area Ωt. They are expressed on a surface $\partial\Omega_t$ with the stress tensor $\boldsymbol{\sigma}$:

$$\text{surface force} = \int_{\partial\Omega_t} \{\boldsymbol{\sigma} \cdot \mathbf{n}\}(\mathbf{s}, t) d\mathbf{s}. \tag{2.25}$$

  Typical examples of surface forces are pressure and inner friction.

In three spatial dimensions the nine components of the stress tensor $\sigma_{\alpha\beta}$ are defined at any point in space relative to rectangular Cartesian coordinates. The stress tensor $\sigma_{\alpha\beta}$ describes the αth component of stress on a surface element $\delta\mathbf{S}$ which has a normal $\mathbf{n}$ pointing in the βth direction, see figure 2.5 (left). For an arbitrary surface element $\delta\mathbf{S}$ with unit normal $\mathbf{n}$ the stress vector $\mathbf{t}$ can be calculated using the summation convention, see figure 2.5 (right):

$$t_\alpha = \sigma_{\alpha\beta} n_\beta. \tag{2.26}$$

For more information about the summation convention as well as the tensor algebra and calculus the reader may refer to [30].

When the body and surface forces act on a fluid the second law of Newton, stating that the change of momentum in respect to time equals the forces acting on the fluid, takes the form

$$\frac{D}{Dt}\mathbf{j}(t) = \int_{\Omega_t} \{\rho\mathbf{g}\}(\mathbf{x},t)d\mathbf{x} + \int_{\partial\Omega_t} \{\boldsymbol{\sigma}\cdot\mathbf{n}\}(\mathbf{s},t)d\mathbf{s}. \qquad (2.27)$$

On the left hand side the transport theorem is used on every component $(\alpha = 1 \ldots N)$:

$$\frac{D}{Dt}j_\alpha(t) = \frac{D}{Dt}\int_{\Omega_t} \{\rho u_\alpha\}(\mathbf{x},t)d\mathbf{x} =$$

$$\int_{\Omega_t} \{\frac{\partial}{\partial t}\rho u_\alpha + \nabla\cdot(\rho u_\alpha\mathbf{u})\}(\mathbf{x},t)d\mathbf{x} =$$

$$\int_{\Omega_t} \{\frac{\partial}{\partial t}\rho u_\alpha + (\mathbf{u}\cdot\nabla)\rho u_\alpha + \rho u_\alpha(\nabla\cdot\mathbf{u})\}(\mathbf{x},t)d\mathbf{x}, \qquad (2.28)$$

and on the right hand side the divergence theorem is applied $(\alpha = 1 \ldots N)$:

$$\int_{\Omega_t} \{\rho g_\alpha\}(\mathbf{x},t)d\mathbf{x} + \int_{\partial\Omega_t} \{(\boldsymbol{\sigma}\cdot\mathbf{n})_\alpha\}(\mathbf{s},t)d\mathbf{s} = \qquad (2.29)$$

$$\int_{\Omega_t} \{\rho g_\alpha + (\nabla\cdot\boldsymbol{\sigma})_\alpha\}(\mathbf{x},t)d\mathbf{x}. \qquad (2.30)$$

Thus 2.27 takes the form

$$\int_{\Omega_t} \{\frac{\partial}{\partial t}\rho u_\alpha + (\mathbf{u}\cdot\nabla)\rho u_\alpha + \rho u_\alpha(\nabla\cdot\mathbf{u})\}(\mathbf{x},t)d\mathbf{x} = \qquad (2.31)$$

$$\int_{\Omega_t} \{\rho g_\alpha + (\nabla\cdot\boldsymbol{\sigma})_\alpha\}(\mathbf{x},t)d\mathbf{x}. \qquad (2.32)$$

This applies for all areas Ω_t and therefore yields into the momentum equation in general form:

$$\frac{\partial}{\partial t}\rho\mathbf{u} + (\mathbf{u}\cdot\nabla)\rho\mathbf{u} + \rho\mathbf{u}(\nabla\cdot\mathbf{u}) - \rho\mathbf{g} - \nabla\cdot\boldsymbol{\sigma} = 0. \qquad (2.33)$$

Often the momentum equation is used in combination with the continuity equation. In the incompressible case the general form in combination with the incompressible continuity equation (2.22) can be simplified into the incompressible momentum equation:

$$\frac{D\mathbf{u}}{Dt} = \frac{1}{\rho}(\nabla \cdot \boldsymbol{\sigma}) + \mathbf{g}. \tag{2.34}$$

The properties of these equations depend strongly on the stress tensor $\boldsymbol{\sigma}$. In the next two chapters two popular choices of $\boldsymbol{\sigma}$ are discussed in more detail. In combination with the continuity equation the first one leads to the Euler equations the second one to the Navier-Stokes equations.

2.1.5   Euler equations

The easiest choice for the stress tensor $\boldsymbol{\sigma}$ is to neglect all surface forces except for the pressure. In this case $\boldsymbol{\sigma}$ takes the form

$$\sigma(x,t)_{\alpha\beta} = -p(x,t)\delta_{\alpha\beta}, \tag{2.35}$$

where p is the pressure and $\delta_{\alpha\beta}$ the Kronecker symbol. Inserting $\boldsymbol{\sigma}$ into the momentum equation of general form (2.33) and using the continuity equation (2.21) the compressible Euler equations are obtained:

$$\frac{\partial}{\partial t}\rho\mathbf{u} + (\mathbf{u} \cdot \nabla)\rho\mathbf{u} + \rho\mathbf{u}(\nabla \cdot \mathbf{u}) = -\nabla p(\mathbf{x},t) + \rho\mathbf{g}$$
$$\frac{\partial}{\partial t}\rho + \nabla \cdot \rho\mathbf{u} = 0. \tag{2.36}$$

In addition an energy equation must be added relating pressure and energy and further a state equation relating pressure, density and energy, see for example [31].

For incompressible fluids the situation is easier. It is assumed that the density is constant $\rho_{const} = \rho(x,t)$. The incompressible Euler equations are obtained with the incompressible momentum equation (2.34) and the incompressible

continuity equation (2.22):

$$\begin{aligned}
\frac{D\mathbf{u}}{Dt} &= -\frac{1}{\rho}\nabla p(\mathbf{x}, t) + \mathbf{g} \\
\nabla \cdot \mathbf{u} &= 0.
\end{aligned} \tag{2.37}$$

Often it is convenient to rewrite the incompressible Euler equations in Cartesian coordinates. The resulting equation contains the momentum flux tensor, which is often needed in the derivation of numerical methods. Using tensor notation and neglecting body forces the incompressible Euler equations can be expressed as

$$\begin{aligned}
\frac{\partial}{\partial t}u_\alpha + u_\beta \frac{\partial}{\partial x_\beta}u_\alpha &= -\frac{1}{\rho}\frac{\partial}{\partial x_\alpha}p \\
\frac{\partial}{\partial x_\alpha}u_\alpha &= 0.
\end{aligned} \tag{2.38}$$

The momentum equation can be rewritten to

$$\begin{aligned}
\frac{\partial}{\partial t}u_\beta + u_\alpha \frac{\partial}{\partial x_\alpha}u_\beta + u_\beta \frac{\partial}{\partial x_\alpha}u_\alpha &= -\frac{1}{\rho}\frac{\partial}{\partial x_\alpha}\sigma_{\alpha\beta} \\
\frac{\partial}{\partial t}u_\beta + \frac{\partial}{\partial x_\alpha}(u_\alpha u_\beta) &= -\frac{1}{\rho}\frac{\partial}{\partial x_\alpha}\sigma_{\alpha\beta} \\
\frac{\partial}{\partial t}u_\beta &= -\left(\frac{\partial}{\partial x_\alpha}\sigma_{\alpha\beta} + \rho\frac{\partial}{\partial x_\alpha}(u_\alpha u_\beta)\right) \\
\frac{\partial}{\partial t}u_\beta &= -\frac{\partial}{\partial x_\alpha}\Pi_{\alpha\beta}.
\end{aligned} \tag{2.39}$$

Inserting the stress tensor $\sigma_{\alpha\beta}$ from 2.35 gives the momentum flux tensor of the incompressible Euler equation:

$$\Pi_{\alpha\beta} = \delta_{\alpha\beta}p + \rho u_\alpha u_\beta. \tag{2.40}$$

The momentum flux tensor describes the momentum flowing through a surface element $d\mathbf{S}$ with a unit normal $\mathbf{n}$. The momentum flux through $d\mathbf{S}$ can

be calculated, analog to equation 2.26, see figure 2.5, thus

$$f_\alpha = \Pi_{\alpha\beta} n_\beta. \tag{2.41}$$

The momentum flux tensor is important for understanding numerical schemes that are based on a regular cartesian lattice.

The incompressible Euler equations describe the behavior of ideal fluids. They capture a lot of important properties of fluids but cannot be used to describe viscous liquids like blood because they neglect inner friction. This means the stress tensor $\boldsymbol{\sigma}$ must be chosen accordingly.

2.1.6 Navier-Stokes equations

To obtain the Navier-Stokes equations from the momentum equation the stress tensor $\boldsymbol{\sigma}$ is selected as

$$\sigma_{\alpha\beta} = -p\delta_{\alpha\beta} + \mu\left(\frac{\partial u_\alpha}{\partial x_\beta} + \frac{\partial u_\beta}{\partial x_\alpha}\right), \tag{2.42}$$

where μ is the dynamic viscosity.

In 1845 Stokes deduced this choice of $\boldsymbol{\sigma}$ from three elementary hypothesis. Therefor the stress is divided into

$$\sigma_{\alpha\beta} = -p\delta_{\alpha\beta} + \sigma^D_{\alpha\beta}. \tag{2.43}$$

The resulting deformation tensor $\sigma^D_{\alpha\beta}$ must satisfy the following three properties:

1. Each $\sigma^D_{\alpha\beta}$ must be a linear function in the velocity gradients $\frac{\partial u_\alpha}{\partial x_\beta}$ with $\alpha, \beta = 1 \ldots N$.

2. Each $\sigma^D_{\alpha\beta}$ must vanish if the flow involves no deformation of fluid elements.

3. The relationship of $\sigma^D_{\alpha\beta}$ to the velocity gradients must be isotropic.

Note that the symmetric deformation tensor

$$\sigma_{\alpha\beta}^D = \mu \left(\frac{\partial u_\alpha}{\partial x_\beta} + \frac{\partial u_\beta}{\partial x_\alpha} \right) \tag{2.44}$$

exactly matches the described properties.

The incompressible momentum equation (2.34) with the choice of $\boldsymbol{\sigma}$ (see 2.42) and the incompressible continuity equation (2.22) are called the incompressible Navier-Stokes equations and are given by

$$\begin{aligned}
\frac{D\mathbf{u}}{Dt} &= -\frac{1}{\rho}\nabla p + \nu\Delta\mathbf{u} + \mathbf{g} \\
\nabla \cdot \mathbf{u} &= 0,
\end{aligned} \tag{2.45}$$

where $\nu = \frac{\mu}{\rho}$ is called the kinematic viscosity. The Navier-Stokes equations are the most important equations in fluid dynamic. They describe the behavior of Newtonian fluids, that are fluids which are incompressible, homogeneous and have the property that their shear stress is linearly proportional to the velocity gradient.

Obtaining analytical solutions is only possible in special cases. There is even no proof of existence for solutions of the incompressible Navier-Stokes equations in three spatial dimensions. Clay Mathematics Institute states that this is one of the most important unsolved mathematical problems.

The momentum flux tensor for the incompressible Navier-Stokes equations can be derived in analogy to the incompressible Euler equations that have been presented in the last section. The Navier-Stokes equations in tensor notation are given by

$$\begin{aligned}
\frac{\partial}{\partial t}u_\alpha + u_\beta\frac{\partial}{\partial x_\beta}u_\alpha &= -\frac{1}{\rho}\frac{\partial}{\partial x_\alpha}p + \nu\frac{\partial}{\partial x_\beta}\frac{\partial}{\partial x_\beta}u_\alpha \\
\frac{\partial}{\partial x_\alpha}u_\alpha &= 0.
\end{aligned} \tag{2.46}$$

Inserting the stress tensor $\sigma_{\alpha\beta}$ from 2.42 into 2.39 yields the momentum flux tensor for the incompressible Navier-Stokes equations:

$$\Pi_{\alpha\beta} = \rho u_{\alpha} u_{\beta} + \delta_{\alpha\beta} p - \mu \left(\frac{\partial u_{\alpha}}{\partial x_{\beta}} + \frac{\partial u_{\beta}}{\partial x_{\alpha}} \right). \qquad (2.47)$$

Using the momentum flux tensor the incompressible Navier-Stokes equations have the simple form

$$\begin{aligned}
\frac{\partial}{\partial t} u_{\beta} &= -\frac{\partial}{\partial x_{\alpha}} \Pi_{\alpha\beta} \\
\frac{\partial}{\partial x_{\alpha}} u_{\alpha} &= 0,
\end{aligned} \qquad (2.48)$$

which is favored when numerical schemes based on a regular cartesian lattice are investigated.

In this section the most important equations of fluid dynamics have been presented. The basic terms and definition will be used frequently within this work. In the next section the equations of fluid dynamic will be applied to blood flow simulation.

2.2   Simulation of blood flow with the Navier-Stokes equations

The equations which have been explained in the previous section will be used to describe dynamic blood flow through an artery tree. Blood flow is influenced by a lot of parameters. First it must be clarified to which extent the equations apply. Next the kinematic similarity of different flows is examined. Further analytical solutions which are relevant for blood flow simulation are presented. The last section describes in which way these results can be used for education with the objective to gain more insight about the basic principles in hemodynamics.

2.2.1   Presumptions

The incompressible Navier-Stokes equations apply for Newtonian fluids. These are fluids in which the shear stress is linearly proportional to the velocity gradient in the direction perpendicular to the plane of shear (see figure 2.5 and equation 2.42). The constant of proportionality is known as the dynamic viscosity μ. Further the fluid must be incompressible and homogeneous.

Blood is not a Newtonian fluid. It is inhomogeneous and viscosity is not constant (particulary in small vessels) and shows complex behavior. In this section it is discussed how far the Navier-Stokes equations are feasible to describe blood flow. When the Navier-Stokes equations are used two important assumptions must be made:

- Blood is homogeneous: In reality blood consists of plasma (55 percent) and cellular constituents (45 percent), see section 1.1.3 and figure 2.6. But if the internal diameter of the vessel under consideration is large compared with the size of red blood cells it behaves like a homogeneous fluid and can be treated as one. Thus the assumption that blood is homogeneous depends strongly on the scale of the problem. Normally inhomogeneous effects can be neglected in vessels with a diameter larger than 0.5 mm.
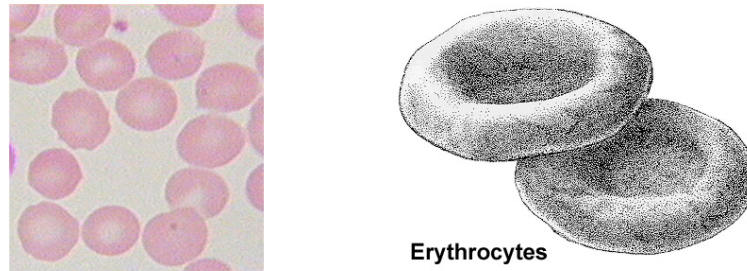
Figure 2.6: *Blood is a suspension of particles in plasma*

- The viscosity is the same at all rates of shear: In larger arteries (diameter > 0.5 mm) the viscosity is independent of the velocity gradient. On the contrary in smaller arteries viscosity is influenced by inhomogeneous effects and shows more complex behavior (for a discussion see [4] pp. 18-22).

The consequence of the these two arguments is that in larger vessels blood behaves like a Newtonian fluid and therefore it can be described with the Navier-Stokes equations. The dynamic viscosity of blood is commonly assumed to be 0.04 Poise, which offers a good approximation in large arteries [32] [5].

When solving the Navier-Stokes equations analytically (see section 2.2.3 and 2.2.4) properties of the flow field and boundary conditions must be stated. In the following some frequently used assumptions are discussed in detail.

1. The liquid does not slip at the wall: The assumption that the velocity is zero at the wall is often applied as boundary condition. This is used for example in Poiseuille flows, see equation 2.61. While this assumption is physically correct sometimes a slip at the wall is presumed to simulate a lower viscosity zone near the wall.

2. The flow is laminar: Under normal circumstances blood flow is laminar, but in large vessels with rates of flow above a critical value turbulence

can occur. The kinematic properties of flows are discussed in the next paragraph. Note that in case of laminar flow all points move parallel to the wall of the tube.

3. The rate of flow is steady: Blood flow in arteries is pulsatile. Nevertheless it is important to examine steady flows, because in some cases conclusions can be drawn from steady flow to the more complex pulsatile flow.

4. The tube is long compared to the region studied: Tubes are often examined in cylindrical coordinates and it is convenient to assume the z axis to have infinite length. This enables an analytically investigation of the flow field avoiding influences from in- and outlets. Thus the results are only realistic in vessels which are long compared to the region under investigation.

5. The tube is cylindrical in shape: In analytical calculations it is convenient to use a simplified geometry in combination with cylindrical coordinates. Of course vessels can have more complicated geometrical structure, but in many cases cylinders are a good approximation. Important insights can be gained investigating flows through idealized shapes.

6. The tube is rigid: It is easier to calculate flows in time independent geometries. During a systolic cycle the diameter of larger arteries varies from five to ten percent [33]. Normally the geometry is obtained from tomographic images which have an error in this order of magnitude. From this point of view the change of geometry can be neglected. But when the interest lies in the behavior of the fluid flow near the vessel wall, for example when the wall shear stress is under investigation, it seems important to include the effects of elasticity [34]. The reason for this is that elasticity influences the shear stress patterns at walls.

In this work blood will be treated as a Newtonian fluid with a viscosity of 0.04 Poise. Depending on the problem the presumptions and approximations from above will be applied.

2.2.2 Kinematic similarity of different flows

In this paragraph the kinematic similarity of different flows is examined. This considerations are of major importance for both physical experiments like flows in wind tunnels and for numerical experiments in computer fluid dynamics.

Two flows show similar behavior when the relation between their governing forces are the same. The forces which are related in the Navier-Stokes equations are:

$$
\frac{\partial \mathbf{u}}{\partial t} + \underbrace{(\mathbf{u} \cdot \nabla)\mathbf{u}}_{\text{vis inertiae}} = \overbrace{-\frac{1}{\rho}\nabla p}^{\text{pressure}} + \underbrace{\nu \Delta \mathbf{u}}_{\text{viscous force}} + \mathbf{g}. \tag{2.49}
$$

To estimate the magnitude of these forces first a characteristic flow speed U and a characteristic length L is chosen, meaning

$$
\begin{aligned}
|\mathbf{u}| &= O(U) \quad \text{and} \\
x_j &= O(L)
\end{aligned} \tag{2.50}
$$

with $j = 1 \ldots N$ and therefore

$$
\left| \frac{\delta \mathbf{u}}{\delta x_j} \right| = O\left(\frac{U}{L} \right). \tag{2.51}
$$

In this way the order of vis inertiae and viscous force are obtained:

$$
\begin{aligned}
|(\mathbf{u} \cdot \nabla)\mathbf{u}| &= O\left(\frac{U^2}{L} \right), \\
|\nu \Delta \mathbf{u}| &= O\left(\nu \frac{U}{L^2} \right).
\end{aligned} \tag{2.52}
$$

Now the relation between the two forces can be calculated:

$$\frac{|(\mathbf{u} \cdot \nabla)\mathbf{u}|}{|\nu \Delta \mathbf{u}|} = O\left(\frac{U^2}{L} \Big/ \nu \frac{U}{L^2}\right) = O\left(\frac{UL}{\nu}\right). \tag{2.53}$$

Thus two systems with characteristic speeds U_1 and U_2, characteristic lengths L_1 and L_2 and kinematic viscosities ν_1 and ν_2 are kinematic similar if

$$\frac{U_1 L_1}{\nu_1} \approx \frac{U_2 L_2}{\nu_2}. \tag{2.54}$$

The number

$$\mathrm{Re} = \frac{UL}{\nu} \tag{2.55}$$

is called Reynolds number. It characterizes kinematic properties of the flow. Note that the Reynolds number is dimensionless, in example $U = [\frac{cm}{s}]$, $L = [cm]$ and $\nu = [\frac{cm^2}{s}]$. A flow with a high Reynolds number is called turbulent ($\mathrm{Re} > 2300$), a low Reynolds number flow is called laminar ($\mathrm{Re} < 2100$).

2.2.3   Poiseuille flows

In general the Navier-Stokes equations cannot be solved analytically. There are only a few known solutions. For blood flow simulation Poiseuille flows and Womersley flows have proved to be of major importance. A lot of progress in understanding hemodynamics has been done by T. J. Pedley [5] and Y. C. Fung [32] [35] using analytical methods. These solutions can be used to explain basic properties of blood flow and to validate numerical methods that are applied to blood flow simulation.

Steady laminar flow through a rigid tube has been calculated independently by Hagen in 1839 and by Poiseuille in 1842. The resulting formula is called the Hagen-Poiseuille equation or often only Poiseuille equation. The equation states that the flow Q is dependent on the fourth power of the radius R, thus

$$Q = \frac{\pi R^4 (P_1 - P_2)}{8 \mu L} \tag{2.56}$$

with the pressure difference $(P_1 - P_2)$ and the tube length L with dynamic viscosity μ.

The Poiseuille equation has been stated before the Navier-Stokes equations and can be justified by basic physical arguments, see for example [4], pp. 12-15. In this section the velocity profile of such flows shall be derived directly from the Navier-Stokes equations in two and in three spatial dimensions. In the following derivation some presumptions from section 2.2.1 are applied.

The incompressible Navier-Stokes equations in two spatial dimensions without body forces are given by

$$
\begin{aligned}
\frac{\partial u_x}{\partial t} + u_x \frac{\partial u_x}{\partial x} + u_y \frac{\partial u_x}{\partial y} &= -\frac{1}{\rho}\frac{\partial p}{\partial x} + \nu \left(\frac{\partial^2 u_x}{\partial x^2} + \frac{\partial^2 u_x}{\partial y^2}\right) \\
\frac{\partial u_y}{\partial t} + u_x \frac{\partial u_y}{\partial x} + u_y \frac{\partial u_y}{\partial y} &= -\frac{1}{\rho}\frac{\partial p}{\partial y} + \nu \left(\frac{\partial^2 u_y}{\partial x^2} + \frac{\partial^2 u_y}{\partial y^2}\right) \\
\frac{\partial u_x}{\partial x} + \frac{\partial u_y}{\partial y} &= 0.
\end{aligned}
\tag{2.57}
$$

If a laminar steady flow is assumed the direction of the x axis the flow field is independent of x and there is no movement along the y axis (see figure 2.7), thus

$$
\begin{aligned}
u_x(x,y) &= u_x(y) \\
u_y(x,y) &= 0.
\end{aligned}
\tag{2.58}
$$

The flow field is inserted into equation 2.57. Note that the flow field has the properties $\frac{\partial u_x}{\partial x} = \frac{\partial u_y}{\partial x} = 0$ and $\frac{\partial u_y}{\partial y} = 0$. Therefore the problem simplifies to

$$
\begin{aligned}
\frac{\partial u_x}{\partial t} &= -\frac{1}{\rho}\frac{\partial p}{\partial x} + \nu \frac{\partial^2 u_x}{\partial y^2} \\
0 &= -\frac{1}{\rho}\frac{\partial p}{\partial y}.
\end{aligned}
\tag{2.59}
$$

Thus there is no change of pressure in y direction and since we assume steady flow $\frac{\partial u_x}{\partial t} = 0$. The pressure gradient is set to $\frac{\partial p}{\partial x} = \frac{P_1 - P_2}{L}$ and the resulting
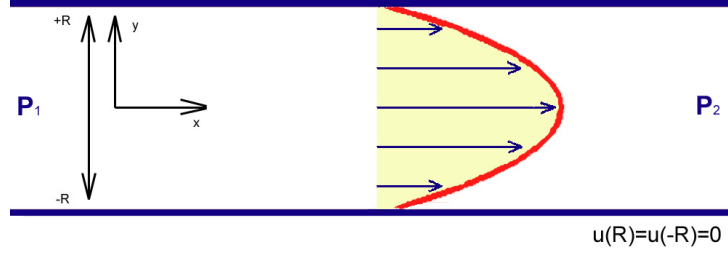
Figure 2.7: *The parabolic velocity profile of a Poiseuille flow*

ordinary differential equation in y is given by

$$\frac{1}{\rho}\frac{P_1 - P_2}{L} = \nu\frac{\partial^2}{\partial y^2}u_x(y). \tag{2.60}$$

The boundary conditions

$$u_x(R) = u_x(-R) = 0 \tag{2.61}$$

describe that there is no movement at the bounding walls. This is often called a no-slip condition. The solution of equation 2.60 with 2.61 is given by

$$u_x(y) = \frac{(R^2 - y^2)(P_1 - P_2)}{2\rho\nu L} = \frac{(R^2 - y^2)(P_1 - P_2)}{2\mu L}, \tag{2.62}$$

which is the parabolic velocity profile of a Poiseuille flow, see figure 2.7. The Poiseuille profile is often used for a simple verification of numerical methods in two dimensions.

The classical Poiseuille equation (equation 2.56) applies only in three spatial dimension. It can be easily obtained by applying the same arguments to the incompressible Navier-Stokes equations in cylindrical polar coordinates

which are given by

$$
\frac{\partial u_r}{\partial t} + (\mathbf{u} \cdot \nabla)u_r - \frac{u_\varphi^2}{r} = -\frac{1}{\rho}\frac{\partial p}{\partial r} + \nu(\nabla^2 u_r - \frac{u_r}{r^2} - \frac{2}{r^2}\frac{\partial u_\varphi}{\partial \varphi})
$$
$$
\frac{\partial u_\varphi}{\partial t} + (\mathbf{u} \cdot \nabla)u_\varphi + \frac{u_r u_\varphi}{r} = -\frac{1}{\rho r}\frac{\partial p}{\partial \varphi} + \nu(\nabla^2 u_\varphi + \frac{2}{r^2}\frac{\partial u_r}{\partial \varphi} - \frac{u_\varphi}{r^2})
$$
$$
\frac{\partial u_z}{\partial t} + (\mathbf{u} \cdot \nabla)u_z = -\frac{1}{\rho}\frac{\partial p}{\partial z} + \nu\nabla^2 u_z
$$
$$
\frac{1}{r}\frac{\partial (r u_r)}{\partial r} + \frac{1}{r}\frac{\partial u_\varphi}{\partial \varphi} + \frac{\partial u_z}{\partial z} = 0 \tag{2.63}
$$

with

$$
(\mathbf{u} \cdot \nabla) = u_r\frac{\partial}{\partial r} + \frac{u_\varphi}{r}\frac{\partial}{\partial \varphi} + u_z\frac{\partial}{\partial z} \tag{2.64}
$$
$$
\nabla^2 = \frac{1}{r}\frac{\partial}{\partial r}\left(r\frac{\partial}{\partial r}\right) + \frac{1}{r^2}\frac{\partial^2}{\partial \varphi^2} + \frac{\partial^2}{\partial z^2}. \tag{2.65}
$$

Again a laminar flow following its z axis is assumed:

$$
u_r = 0
$$
$$
u_\varphi = 0
$$
$$
u_z = u_z(r, t). \tag{2.66}
$$

Inserting the flow field into the equations 2.63 the Navier-Stokes equations take the form

$$
0 = -\frac{1}{\rho}\frac{\partial p}{\partial r}
$$
$$
0 = -\frac{1}{\rho r}\frac{\partial p}{\partial \varphi}
$$
$$
\frac{\partial u_z}{\partial t} = -\frac{1}{\rho}\frac{\partial p}{\partial z} + \nu\frac{1}{r}\frac{\partial}{\partial r}\left(r\frac{\partial}{\partial r}\right)u_z. \tag{2.67}
$$

When steady flow $\frac{\partial u_z}{\partial t} = 0$ is assumed and a constant pressure gradient

$\frac{\partial p}{\partial z} = \frac{P_1 - P_2}{L}$ is given the following equation is obtained:

$$\frac{1}{\mu}\frac{P_1 - P_2}{L} = \frac{1}{r}\frac{\partial}{\partial r}\left(r\frac{\partial}{\partial r}\right)u_z. \tag{2.68}$$

If the no-slip boundary condition $u_z(R) = 0$ is applied, the solution of the differential equation is given by

$$u_z(r) = \frac{(R^2 - r^2)(P_1 - P_2)}{4\mu L}. \tag{2.69}$$

Integrating u_z over one slice gives the flow Q resulting the Poiseuille equation:

$$Q = \int_0^R 2\pi r u_z(r)dr = \frac{\pi R^4(P_1 - P_2)}{8\mu L}. \tag{2.70}$$

As discussed in section 2.2.1 the elasticity of the vessel wall effects the shear stress pattern of the fluid. The Poiseuille theory of laminar flows can be easily extended to elastic tubes. Normally Hook's law is used for the description of elasticity. But vessel walls do not obey Hook's law and therefore and easier approach can be used. The following approximation has been proposed by Y. C. Fung [32], who assumed a linear pressure radius relationship

$$r(z) = r_0 + \alpha\frac{p(z)}{2}, \tag{2.71}$$

where r_0 is the tube radius when transmural pressure $p(z)$ is zero and α is the compliance constant. When the derivative in respect to z is taken, thus

$$\frac{\delta r(z)}{\delta z} = \frac{\alpha}{2}\frac{\delta p}{\delta z}, \tag{2.72}$$

the pressure gradient can be inserted into the pressure flow relationship. The pressure flow relationship is calculated analog to equation 2.70 but with a pressure gradient dependent of the location z. The flow Q is equal in every subsection of the tube, thus it is independent of z. The pressure flow

relationship is obtained by integrating 2.69 or respectively 2.62 over one cross section. In three dimension the result is

$$\frac{\delta p}{\delta z} = \frac{8\mu}{\pi a^4} Q \tag{2.73}$$

and in two dimensions it is

$$\frac{\delta p}{\delta z} = \frac{3\mu}{2a^3} Q. \tag{2.74}$$

The equations 2.73 and 2.74 are inserted into the pressure radius relationship 2.72 and integrated in respect to z. Using equation 2.71 the following radius flow relationship is obtained in three dimensions:

$$r(z) = \sqrt[5]{\frac{20\mu\alpha}{\pi} Qz + c_1}, \tag{2.75}$$

respectively in two dimensions:

$$r(z) = \sqrt[4]{12\mu\alpha Qz + c_2}. \tag{2.76}$$

The integration constant c can be calculated from the boundary condition, thus $c_1 = r(0)^5$ and $c_2 = r(0)^4$. The flow radius relationship is plotted in figure 2.8 for different flows. The approximation of elastic walls is often used to validate numerical methods that can handle elasticity, see section 4.2.

2.2.4   Womersley flows

Blood flow is not steady hence the theory of Poiseuille flows cannot be applied. J. R. Womersley studied laminar incompressible flows through a rigid tube with a pulsating flow and therefore time dependent pressure gradient, see [36], [37] and [38]. In these works the incompressible Navier-Stokes equations in cylindrical polar coordinates (equation 2.63) are used as starting point.

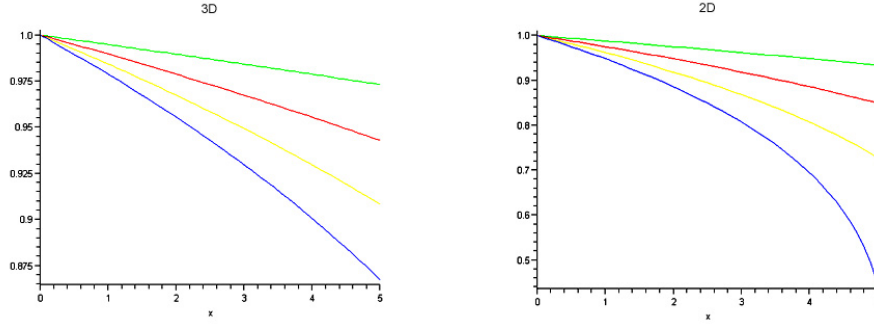Again laminar flow is assumed, thus from the Navier-Stokes equations in

Figure 2.8: *The vesseel radius $r(z)$ in an elastic tube for different flows $Q = \{1, 2, 3, 4\}$ with $\alpha = 0.1, r_0 = 1, \mu = 0.04$*

cylindrical polar coordinates equation 2.67 is obtained, which is the starting point of the following considerations. This equation is rewritten to

$$\frac{1}{\nu}\frac{\partial u_z(r,t)}{\partial t} = -\frac{1}{\rho\nu}\frac{\partial p(t)}{\partial z} + \frac{1}{r}\frac{\partial u_z(r,t)}{\partial r} + \frac{\partial^2 u_z(r,t)}{\partial r^2}. \tag{2.77}$$

For simplicity the time dependent pressure gradient will be taken as a simple harmonic motion

$$-\frac{\partial p(t)}{\partial z} = A^c e^{i\omega t}. \tag{2.78}$$

Note that an arbitrary piecewise continuous and square-integrable pressure gradient could be expressed with a Fourier series as sum of such harmonics. Inserting the pressure gradient into equation 2.77 gives

$$\frac{\partial^2 u_z}{\partial r^2} + \frac{1}{r}\frac{\partial u_z}{\partial r} - \frac{1}{\nu}\frac{\partial u_z}{\partial t} = -\frac{A^c}{\mu}e^{i\omega t}. \tag{2.79}$$

With the substitution

$$u_z(r,t) = w(r,t)e^{i\omega t} \tag{2.80}$$

$$\frac{\partial p(t)}{\partial z} = A^c e^{i\omega t}$$

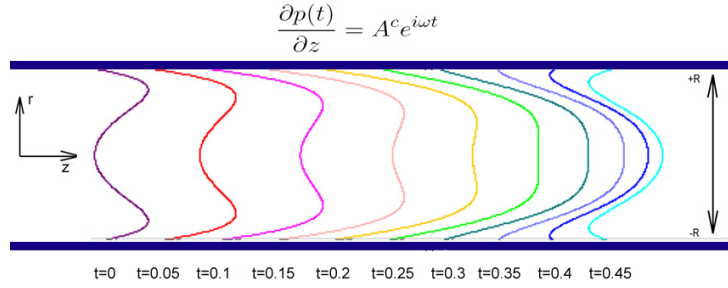t=0 t=0.05 t=0.1 t=0.15 t=0.2 t=0.25 t=0.3 t=0.35 t=0.4 t=0.45

Figure 2.9: *The time dependent velocity profile of a Womersley flow*

the following Bessel's equation is obtained:

$$\frac{d^2w}{w^2} + \frac{1}{r}\frac{dw}{dr} - \frac{i\omega}{\nu}w = -\frac{A^c}{\mu}. \tag{2.81}$$

The equation has the solution (see for example [39])

$$w(r) = \frac{A^c}{i\omega\rho}\left(1 - \frac{J_0(r\sqrt{i^{3/2}\omega/\nu})}{J_0(R\sqrt{i^{3/2}\omega/\nu})}\right), \tag{2.82}$$

where J_0 is a Bessel function of the first kind of order zero with a complex argument. It is given by

$$J_0(x) = \sum_{i=0}^{\infty} \frac{(-1)^m}{m\Gamma(m+1)}\left(\frac{x}{2}\right)^{2m}. \tag{2.83}$$

The number

$$\alpha = R\sqrt{\frac{\omega}{\nu}} \tag{2.84}$$

is referred to as Womersley number. It is a non-dimensional number and characterizes the kinematic properties of the fluid. With α, $y = \frac{r}{R}$ and resubstitution the solution

$$u_z(y,t) = \frac{A^c R^2}{i\mu\alpha^2}\left(1 - \frac{J_0(\alpha y i^{3/2})}{J_0(\alpha i^{3/2})}\right)e^{i\omega t} \tag{2.85}$$
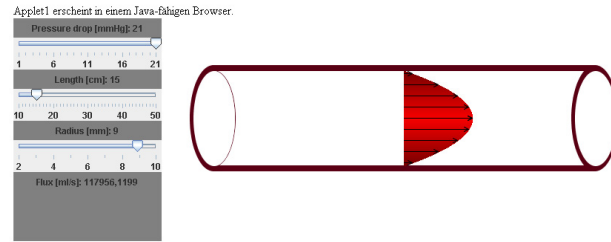
Figure 2.10: *Poiseuille flows*

is obtained. This is the typical profile of a Womersley flow, see figure 2.9. The velocity profile is often used to validate numerical solutions in two and three dimensions with time dependent boundary conditions.

2.2.5 Selected examples for education in hemodynamics

In the previous chapter a introduction to fluid dynamics has been given. The governing equations for fluids are the Navier-Stokes equations. These partial differential equations apply under certain assumptions for hemodynamics, see 2.2.1. Medical students studying hemodynamics often have not got the time to fully understand the occuring partial differential equations, but nevertheless they urgently need insights about the nature of blood flow. For this reason interactive Java Applets have been developed to present basic results and to teach the nature of Poiseuille and Womersley flows, see section 2.2.3 and 2.2.4.

The Applets have been developed in course of a thesis [40] and later have been extended to various flow types and geometries [41]. Every applet is a graphical representation of one or more physical laws that can be investigated by changing parameters interactively. This shall encourage students to experiment with the mathematical models and therefore get a deeper understanding of the topic.

The first Applet shows the velocity profile inside a rigid tube in respect to the tube radius, length and pressure gradient, see figure 2.10. Furthermore
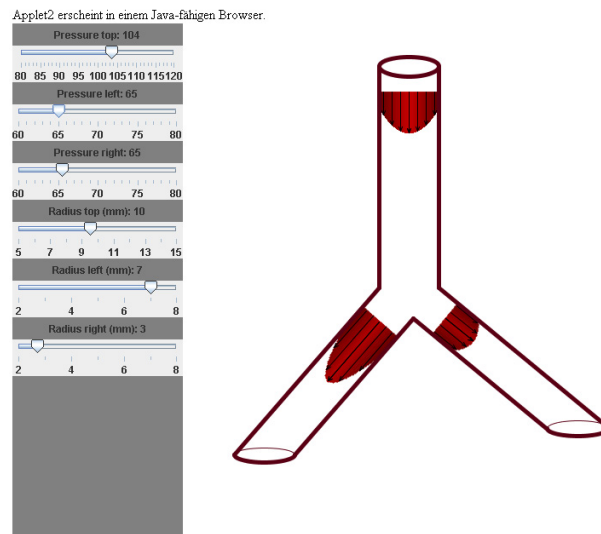
Figure 2.11: *Poiseuille flow in a bifurcation*

the Applet calculates the total flux through the tube. This is an important aspect, which shows for example that if the radius is doubled the flux increases eightfold. As a consequence a change of only 1% in the vessel causes a change in blood flow of approximately 4%. If the flux stays constant the pressure difference must increase 4%, thus tiny narrowing of vessels can lead to hypertension. These are simple but important insights derived from the Poiseuille equation 2.56.

The second applet explains the flow in a bifurcation, see figure 2.11. The radii and pressure differences can be chosen freely, the velocity profiles in the different sections are calculated and updated in realtime. The Applet shall encourage the students to experiment with the different parameters and gives an idea about pressure radius relationship in bifurcations.

The third applet explains the influence of elasticity, see figure 2.12. Steady flow in an elastic tube is calculated analytically, see section 2.2.3. Parameters are radius, length, pressure gradient and the Young modulus. The Young modulus is a measure of stiffness and is defined as the rate of change between
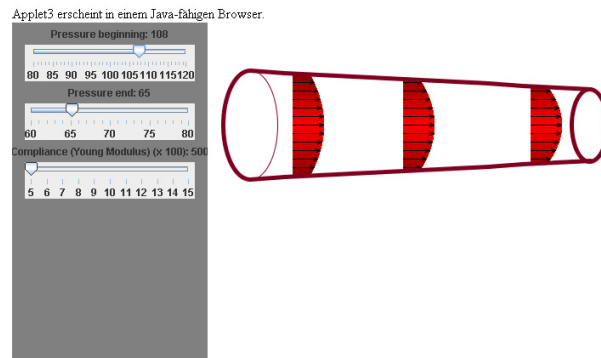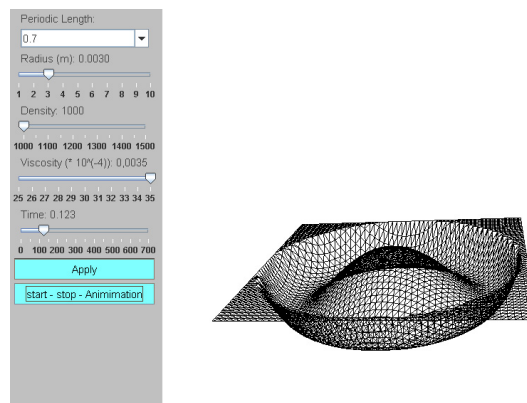
Figure 2.12: Poiseuille flow in elastic vessels

Figure 2.13: Flow profile of a pulsatile flow in three dimensions

stress and strain. The influence of the pressure gradient and the flow to the tubes geometry is of major importance in hemodynamics. Another important aspect is the influence of the compliance on the velocity profile.

For understanding the influence of a time dependent pressure gradient to the velocity profile two Applets have been developed representing equation 2.77. One applet calculates the velocity profiles in two spatial dimensions drawing all profiles over one period. The resulting figure is similar to the representation in figure 2.9.

The second applet calculates the velocity profiles in three spatial dimensions.

This is done in realtime and animated with Java3D, see figure 2.13. The Applet draws a realistic picture of velocity profiles in arteries. In the first and the second Applet viscosity and frequency of the pulsation are important parameters changing the shape of the velocity profiles.

Chapter 3

The Lattice Boltzmann Equation

The incompressible Navier-Stokes equation can only be solved analytically in special occasions. For this reason numerical methods must be developed to simulate blood flow. The method must work for relevant Reynolds and Womersley numbers and must handle time dependent pressure gradients in arbitrary geometries.

There is a huge amount of different methods to calculate the Navier-Stokes equations. The introduction gives a short summary and comparison of the most common methods. After that general Lattice Boltzmann models are introduced. From these models Lattice Bhatnagar Gross and Krook (LBGK) methods are investigated in more detail. LBGK methods are simple and very stable explicit schemes to calculate the Navier-Stokes equations numerically in two and three dimensions.

3.1 Introduction

The numerical treatment of the Navier-Stokes equations in general is complicated. There is a multitude of different numerical schemes and methods that have certain advantages depending on the Reynolds and Womersley numbers under investigation. Recently the LBGK method has been applied to blood flow simulation successfully. In this section the problems solving the Navier-Stokes numerically are discussed and the benefits of the LBGK method are examined.

3.1.1 Numerical methods for the Navier-Stokes equations

The Navier-Stokes equations are a set of nonlinear partial differential equations. When applying standard methods for numerical calculation special care must taken because of the following properties of the equations:

- Physical constraints: The numerical scheme has to consider the conservation of mass and momentum.

- Nonlinearity: In the nonlinear advection term high velocities can lead to numerical instabilities.

- Complex boundary conditions: In fluid dynamics often problems with both complex geometrical boundaries and complex dynamic boundary values appear.

In the domain of blood flow simulation more difficulties arise due to:

- Unusual Reynolds numbers: The Reynolds numbers in the arterial systems are just about laminar, in big arteries turbulence can occur.

- The vessel trees have a big amount of bifurcations: Through branching the amount of vessel sections grows very fast (2^{depth} end sections).

- Unusual properties of the vessel walls: The elasticity is higher than in common engineering applications.

- Unusual instationary effects because of the dynamic nature of pressure and flow.

The classical approach to develop numerical schemes happens in a top down way. This means the Navier-Stokes equations are the starting point, then certain discretization and approximations are performed until an implicit or explicit set of equations are obtained that can be calculated numerically. The most common top down approaches can be summarized in the following way [42]:

- Finite Differences: This is the simplest approach, differential quotients are replaced by difference quotients.

- Finite Volumes: The differential equations are integrated over the spatial domain, the volume integrals are transformed to surface integrals, describing the behavior of the boundary surfaces of discrete cells.

- Finite Elements: The solution is approximated in a weak sense with certain basis functions.

The numerical method presented in this work uses another approach. The fluid is described in a bottom-up way. Instead of developing the discrete scheme from the continuous Navier-Stokes equations a numerical scheme is developed from the underlying Boltzmann equation by basic considerations about molecule behavior.

3.1.2 Description of fluids on different scales

Fluids can be described on different scales. The smallest possible scale is to describe single molecules as point like structureless particles that move along trajectories. This is described by the Newton equations and can be simulated with lattice gas cellular automata (LGCA). On a larger scale, the so called mesoscopic scale, a statistical description of the particles is used. This is done in the Liouville and the Boltzmann equation. The discretization of the Boltzmann equation leads to the Lattice Boltzmann equation (LBE). This equation can be approximated with schemes that are very similar to cellular
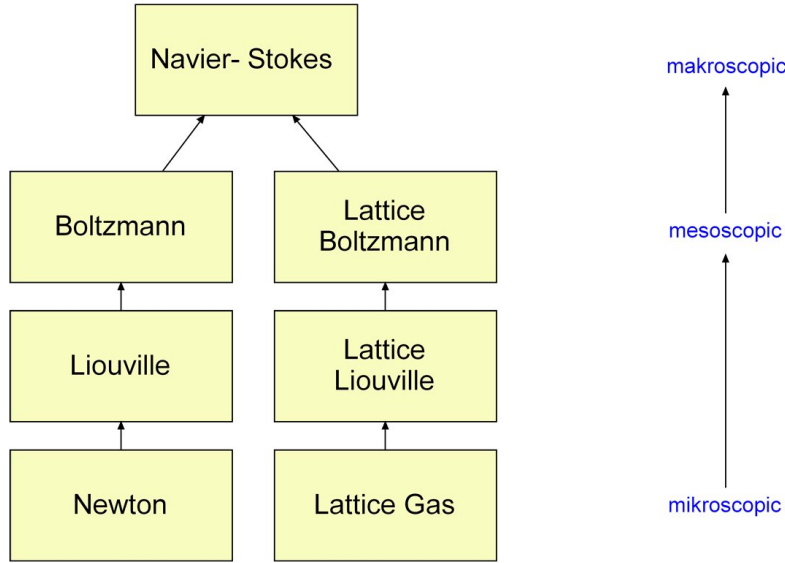
```
         ┌──────────────┐
         │ Navier- Stokes│                          makroscopic
         └──────────────┘                               ↑
           ↗          ↖                                  │
  ┌──────────┐   ┌──────────┐                            │
  │ Boltzmann│   │ Lattice  │                            │
  │          │   │ Boltzmann│               mesoscopic   │
  └──────────┘   └──────────┘                            │
       ↑              ↑                                   │
  ┌──────────┐   ┌──────────┐                            │
  │ Liouville│   │ Lattice  │                            │
  │          │   │ Liouville│                            │
  └──────────┘   └──────────┘                            │
       ↑              ↑                                   │
  ┌──────────┐   ┌──────────┐                            │
  │  Newton  │   │Lattice Gas│              mikroscopic
  └──────────┘   └──────────┘
```

Figure 3.1: *Description of fluids on different scales*

automaton, but have continuous state variables. The macroscopic description of fluids uses arguments of continuum mechanics and yields in the Navier-Stokes equations describing the fluid by relating macroscopic properties, see figure 3.1.

Historically the LBE has developed from LGCA. It has been shown that simple Cellular Automata called FHP can be used to calculate the Navier-Stokes equations [43] and therefore can mimic the complex behavior of fluids. The cellular automata approach is amazing for its simplicity but has some drawbacks like numerical noise and fixed viscosity. Soon after the development of LGCA the LBE has been presented for the first time by G. R. McNamara and G. Zanetti [44]. The LBE lifts many limitations of the LGCA while staying sufficiently simple. LBE can be interpreted as a special discretization of the Boltzmann equation and therefore can be seen as a self-contained theory without the need of LGCA theory. In this work this approach is favored, thus the LBE is derived as a discretization of the Boltzmann equation in the following section.

The Boltzmann equation is used to develop a scheme in a bottom-up way for solving its fluid limit, which are the Navier-Stokes equations. Before the exact derivation of the method is done in chapter 3.2 some advantages of the resulting scheme will be presented.

3.1.3   Advantages of the LBGK method

In the next chapter the Lattice Boltzmann equation and especially the LBGK method will be examined in detail. The main advantages of the LBGK method are:

- LBGK is a bottom-up approach. Starting point are distribution densities of particles. This enables a physical interpretation of every step in the resulting algorithm.

- The physical constraints are fulfilled in a natural way, conservation of mass and momentum are assured.

- LBGK is an explicit scheme, this makes the calculation and implementation very simple, while it is stable enough to deal with Reynolds and Womersley numbers relevant for blood flow simulation.

- LBGK can be calculated very fast and due to its strictly local nature the method is highly feasible for parallel computing.

- Because of the physical interpretation of the method complex boundary conditions can be developed in a heuristic way.

3.2 The Lattice Boltzmann Equation for solving the incompressible Navier-Stokes equations

The main focus of this section lies on the presentation of the LBGK method, a stable explicit method used to solve the incompressible Navier-Stokes equations numerically. First the Lattice Boltzmann Equation (LBE) will be derived from the Boltzmann equation which is the starting point of the development of the LBGK method. In the following section it is proved that the resulting explicit scheme solves the Navier-Stokes equations.

3.2.1 From Boltzmann to Lattice Boltzmann Equation

In 1872 Ludwig Boltzmann has developed his most famous formulas, the Boltzmann equation and the H-theorem. This has been the foundation of classical statistical mechanics. In this section only a few aspects, which are needed for the derivation of the LBE can be shown. An introduction to statistical mechanics is not in scope of this work, a good introduction can be found in [45] and or in [46], where the connection to fluid dynamics is investigated.

The classical Newtonian equations describe molecules as point like structureless particles. The equations cannot be used for practical computations of fluids because there are just too many molecules even on small scales. Usually the number of molecules is in order of the Avogadro number, thus $\approx 10^{23}$, and for computation their paths would have to be tracked over time. Since this is clearly not possible a statistical description is favored.

For this reason distribution functions $f(\mathbf{x}, \mathbf{v}, t)$ are introduced expressing the probable number of molecules around $\mathbf{x}$ with velocity $\mathbf{v}$ at a specific time t. Boltzmann was able to describe the evolution of these distribution functions

over time with the so called Boltzmann equation:

$$\left(\frac{\delta}{\delta t} + \mathbf{v} \cdot \nabla \right) f(\mathbf{x}, \mathbf{v}, t) = \mathcal{C}(f, f) \tag{3.1}$$

The left hand side of the kinetic equation describes the streaming motion, the right hand side the collision $\mathcal{C}(f, f)$.

A link to hydrodynamics is easily obtained, the macroscopic quantities can be calculated as

$$\rho(\mathbf{x}, t) = \int m f(\mathbf{x}, \mathbf{v}, t) d\mathbf{v}$$

$$\mathbf{j}(\mathbf{x}, t) = \rho(\mathbf{x}, t)\mathbf{u}(\mathbf{x}, t) = \int (m\mathbf{v}) f(\mathbf{x}, \mathbf{v}, t) d\mathbf{v}$$

$$\Pi_{\alpha\beta}(\mathbf{x}, t) = \int (m v_\alpha v_\beta) f(\mathbf{x}, \mathbf{v}, t) d\mathbf{v}. \tag{3.2}$$

were ρ is the density, $\mathbf{j}$ the momentum, $\mathbf{u}$ the velocity and Π the momentum flux tensor of the Euler equations, see chapter 2.1.5 and equation 2.40. The Navier-Stokes equations can be recovered by the Chapman Enskog multiscale expansion in section 3.2.3. The expansion will be performed for the LBGK equation. The Chapman Enskog procedure links the two different approaches of statistical mechanics and fluid dynamics.

An equilibrium of a distribution function is defined as the distribution function f^{eq} that is unchanged by the collision operator, thus

$$\mathcal{C}(f^{eq}, f^{eq}) = 0 \tag{3.3}$$

Maxwell showed that

$$f^{eq}(\mathbf{x}, \mathbf{v}, t) = \rho \left(\frac{m}{2\pi k_B T} \right)^{\frac{D}{2}} e^{-\frac{m(\mathbf{v} - \mathbf{u})^2}{2 k_B T}} \tag{3.4}$$

is an equilibrium distribution function, the so called Maxwell-Boltzmann distribution, where $\mathbf{v}$ is the particle velocity, m is the particle mass, T is

the temperature, k_B is the Boltzmann constant and D is the spatial dimension. The distribution function depends only implicitly on $\mathbf{x}$ and t via the macroscopic quantities $\rho(\mathbf{x}, t)$, the fluids density, and $\mathbf{u}(\mathbf{x}, t)$, the fluids mean velocity (see equation 3.2). With the H-theorem Boltzmann has shown that every initial distribution that satisfies the Boltzmann equation decays to the Maxwell-Boltzmann distribution:

$$\begin{aligned} H(t) &= -\int f \ln f \, d\mathbf{v} d\mathbf{x} \\ \frac{dH}{dt} &\leq 0. \end{aligned} \tag{3.5}$$

To derive the LBE from the Boltzmann equation first the phase space is discretized. Instead of all possible particle speeds and directions the phase space is reduced to a small set of allowed velocities. The Boltzmann equation then takes the form

$$\left(\frac{\delta}{\delta t} + \mathbf{c}_i \cdot \nabla \right) f_i(\mathbf{x}, t) = \mathcal{C}_i \tag{3.6}$$

with the set of velocities $\mathbf{c}_i$ and for simplicity $f_i(\mathbf{x}, t) \equiv f(\mathbf{x}, \mathbf{c}_i, t)$. Popular choices of the set $\mathbf{c}_i$ will be presented in the following section.

The next step is to discretize time and space using simple forward differences of first order:

$$\begin{aligned} &\frac{1}{\Delta t}(f_i(\mathbf{x}, t + \Delta t) - f_i(\mathbf{x}, t)) \\ &+\mathbf{c}_{ix}\frac{1}{\Delta x}(f_i(\mathbf{x} + \Delta x, t + \Delta t) - f_i(\mathbf{x}, t + \Delta t)) \\ &+\mathbf{c}_{iy}\frac{1}{\Delta y}(f_i(\mathbf{x} + \Delta y, t + \Delta t) - f_i(\mathbf{x}, t + \Delta t)) \\ &+\mathbf{c}_{iz}\frac{1}{\Delta z}(f_i(\mathbf{x} + \Delta z, t + \Delta t) - f_i(\mathbf{x}, t + \Delta t) = \mathcal{C}_i. \end{aligned} \tag{3.7}$$

The lattice spacing is chosen in a way that $\Delta \mathbf{x} = \mathbf{c}_i \Delta t$. This couples the spatial and temporal resolution and guaranties Lagrangian behavior. Inserted

into 3.7 the LBE is obtained:

$$f_i(\mathbf{x} + \mathbf{c}_i\Delta t, t + \Delta t) - f_i(\mathbf{x}, t) = \Delta t \mathcal{C}_i. \tag{3.8}$$

The velocities $\mathbf{c}_i$ and the collision operator $\mathcal{C}_i$ must be chosen carefully. The macroscopic hydrodynamic quantities are the zeroth, first and second moment of the discrete distribution function (in analogy to equation 3.2):

$$
\begin{aligned}
\rho(\mathbf{x}, t) &= \sum_i f_i(\mathbf{x}, t) \\
\mathbf{j}(\mathbf{x}, t) = \rho(\mathbf{x}, t)\mathbf{u}(\mathbf{x}, t) &= \sum_i \mathbf{c}_i f_i(\mathbf{x}, t) \\
\Pi_{\alpha\beta}(\mathbf{x}, t) &= \sum_i c_{i\alpha} c_{i\beta} f_i(\mathbf{x}, t).
\end{aligned}
\tag{3.9}
$$

When the LBE has been presented for the first time the collision operator has been chosen in strict analogy to the LGCA leading to a nonlinear collision operator, which is computational expensive, see [44]. First improvements have been done by F. Higuera and J. Jimenez [47] who have presented a linear collision operator, which has been constructed by linearization about a local equilibrium f^{eq}. The resulting LBE is called quasilinear LBE and the collision operator $\mathcal{C}_i$ can be described as

$$\mathcal{C}_i = \mathcal{A}_{ij}(f_j - f_j^{eq}). \tag{3.10}$$

For a detailed description of the construction of $\mathcal{A}_{ij}$ the reader may refer to [48].

In this work a coarser approximation of the collision operator is favored, the so called Bhatnagar Gross and Krook (BGK) approximation. The discrete version BGK approximation leads to the LBGK method. A detailed description of the method and the most popular choices of sets of velocities $\mathbf{c}_i$ and corresponding equilibria distribution functions f^{eq} are given in the next section.

3.2.2   LBGK schemes

The collision operator $\mathcal{C}$ in the Boltzmann equation (see 3.1) is of very complicated nature. P. L. Bhatnagar, E. P. Gross and M. Krook [49] and at the same time P. Welander [50] have approximated the collision with a movement towards an equilibrium:

$$\left(\frac{\delta}{\delta t} + \mathbf{v} \cdot \nabla\right) f(\mathbf{x}, \mathbf{v}, t) = -\frac{1}{\tau}(f(\mathbf{x}, \mathbf{v}, t) - f^{eq}(\mathbf{x}, \mathbf{v}, t))), \qquad (3.11)$$

where f^{eq} is the Maxwell distribution (see equation 3.4) and τ is the collision time and thus $\frac{1}{\tau}$ the collision frequency. The BGK approximation captures two important properties of the collision operator. First the collision invariants of the operator are conserved. These invariants are mass, moment and kinetic energy. Secondly the distribution function decays to the Maxwell distribution through collision. This means that the H-theorem (3.5) is still valid.

The discrete version of the Boltzmann equation with the BGK approximation of the collision operator has been presented by [51] and [52] and is usually called LBGK equation. It is obtained by inserting the BGK approximation into the discrete kinetic equation 3.8. Hence the LBGK equation takes the form

$$f_i(\mathbf{x} + \mathbf{c}_i\Delta t, t + \Delta t) - f_i(\mathbf{x}, t) = -\frac{\Delta t}{\tau}(f_i(\mathbf{x}, t) - f_i^{eq}(\rho(\mathbf{x}, t), \mathbf{j}(\mathbf{x}, t))) \ (3.12)$$

with $\rho(\mathbf{x}, t)$ and $\mathbf{j}(\mathbf{x}, t)$ from equation 3.9. The parameter τ is the collision time and the discrete equilibrium distribution function $f_i^{eq}(\mathbf{x}, t) \equiv f^{eq}(\mathbf{x}, \mathbf{c}_i, t)$ is an approximation of the Maxwell-Boltzmann distribution function (see equation 3.4). Often the LBGK equation is formulated as

$$f_i(\mathbf{x}, t + \Delta t) = (1 - \omega)f_i(\mathbf{x} - \mathbf{c}_i\Delta t, t) + \omega f_i^{eq}(\mathbf{x} - \mathbf{c}_i\Delta t, t) \qquad (3.13)$$

with the collision frequency $\omega = \frac{\Delta t}{\tau}$. This representation of the LBGK makes the explicit nature of the method more visible. In the following possible choices of the equilibrium distribution function f_i^{eq} and the velocities $\mathbf{c}_i$ are

discussed in more detail.

The approximated equilibrium distribution function is derived by applying the maximum entropy principle under the constraint of conservation of mass, momentum and momentum flux, see [52]. The result is a polynom of second order

$$f_i^{eq}(\rho, \mathbf{j}) = \frac{w_i}{\rho_0}(\rho + \frac{m}{k_B T}\mathbf{c}_i \cdot \mathbf{j} + \frac{m}{2\rho k_B T}(\frac{m}{k_B T}(\mathbf{c}_i \cdot \mathbf{j})^2 - \mathbf{j}^2)) \qquad (3.14)$$

with weighting factors w_i, mass density ρ_0, particle mass m, particle speed $\mathbf{v}$, Boltzmann constant k_B, temperature T and with density $\rho = \rho(\mathbf{x}, t)$ and moment $\mathbf{j} = \mathbf{j}(\mathbf{x}, t)$ from equation 3.9. Note that the conservation of mass and momentum of f_i^{eq} yields:

$$
\begin{aligned}
\rho(\mathbf{x}, t) &= \sum_i f_i^{eq}(\rho, \mathbf{j}) \\
\mathbf{j}(\mathbf{x}, t) &= \rho(\mathbf{x}, t)\mathbf{u}(\mathbf{x}, t) = \sum_i \mathbf{c}_i f_i^{eq}(\rho, \mathbf{j}).
\end{aligned}
\qquad (3.15)
$$

The weighting factors w_i must be chosen in accordance to the velocities $\mathbf{c}_i$ in a way that for vanishing velocities, thus $\mathbf{j} = \mathbf{0}$, the velocity moments up to fourth order of the approximated equilibrium function equals the velocity moments of the Maxwell-Boltzmann distribution. For vanishing velocities the Maxwell-Boltzmann distribution (equation 3.4) takes the form

$$f^{eq}(\mathbf{v}) = \rho_0 \left(\frac{m}{2\pi k_B T}\right)^{\frac{D}{2}} e^{-\frac{m\mathbf{v}^2}{2k_B T}}, \qquad (3.16)$$

where ρ_0 is the mass density, m the particle mass, $\mathbf{v}$ the particle speed, k_B the Boltzmann constant, T the temperature and D the spatial dimension.

The moments of the weighting factors on the left hand side equal the corresponding moments of the Maxwell-Boltzmann distribution for vanishing

velocities on the right hand side, thus

$$
\begin{aligned}
\sum_i w_i &= \rho_0 \\
\sum_i \mathbf{c}_{i\alpha} w_i &= 0 \\
\sum_i \mathbf{c}_{i\alpha} \mathbf{c}_{i\beta} w_i &= \rho_0 \frac{k_B T}{m} \delta_{\alpha\beta} \\
\sum_i \mathbf{c}_{i\alpha} \mathbf{c}_{i\beta} \mathbf{c}_{i\gamma} w_i &= 0 \\
\sum_i \mathbf{c}_{i\alpha} \mathbf{c}_{i\beta} \mathbf{c}_{i\gamma} \mathbf{c}_{i\delta} w_i &= \rho_0 \left(\frac{k_B T}{m} \right)^2 (\delta_{\alpha\beta}\delta_{\gamma\delta} + \delta_{\alpha\gamma}\delta_{\beta\delta} + \delta_{\alpha\delta}\delta_{\beta\gamma}).
\end{aligned} \tag{3.17}
$$

The weighting factors w_i and the value $k_B T/m$ must be calculated from the equations above. Note that $k_B T/m$ has no analogy in the macroscopic equations and is regarded to be constant. Valid solutions for w_i and $k_B T/m$ can be found whenever the number of velocities $\mathbf{c}_i$ is large enough. Qian has presented various solutions in [51] and [53] for different lattices.

The lattices used for LBGK methods are normally called DdQq, where d is the spatial dimension and q denoting the number of lattice velocities. The lattice velocities $\mathbf{c}_i$ are the same for every lattice node $\mathbf{x}$ and are given on cube $\Delta V = [-c, c]^D$, where the lattice velocity

$$
c = \frac{\Delta x}{\Delta t} \tag{3.18}
$$

couples the spatial resolution Δx to the temporal resolution Δt. In this way it is assured that $\mathbf{x} + \mathbf{c}_i \Delta t$ is again a lattice node.

In two spatial dimensions the most popular lattice is the D2Q9 lattice (see figure 3.2) with the corresponding weights from table 3.1. In this work the D2Q9 LBGK method is used for simulation in two dimensions.

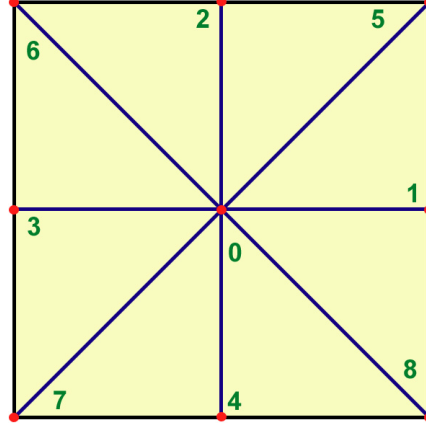In three spatial dimensions there are two popular choices, the D3Q15 LBGK

Figure 3.2: *The velocities $c_0 \ldots c_8$ of the D2Q9 lattice*

Index of $\mathbf{c}_i$	length of $\mathbf{c}_i$	Weights w_i	$k_B T/m$
0	0	$\frac{4}{9}$	$\frac{1}{3}c^2$
1,2,3,4	c	$\frac{1}{9}$	
5,6,7,8	$\sqrt{2}c$	$\frac{1}{36}$	

Table 3.1: *Weights of D2Q9 LBGK*

method and the D3Q19 LBGK method. In this work the D3Q15 LBGK method is favored. The D3Q15 lattice, see figure 3.3, needs less storage than the D3Q19 lattice and is computationally cheaper. The weights can be found in table 3.2.

In literature the D3Q19 LBGK method is frequently used, see figure 3.4 with the corresponding weights in table 3.3. The advantage of the higher number of lattice velocities is a higher stability range of the D3Q19 LBGK method. In the domain of blood flow simulation the D3Q15 method has proved to be sufficient.

The LBGK models described in this section are explicit schemes for calculating the incompressible Navier-Stokes equations 2.45. The LBGK consists
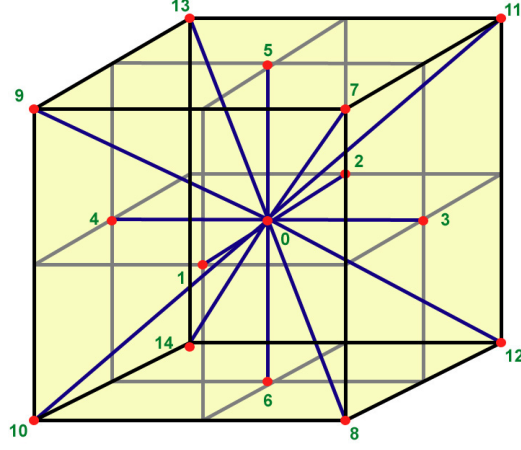
Figure 3.3: *The velocities $\mathbf{c}_0 \ldots \mathbf{c}_{14}$ of the D3Q15 lattice*

Index of $\mathbf{c}_i$	length of $\mathbf{c}_i$	Weights w_i	$k_B T/m$
0	0	$\frac{2}{9}$	$\frac{1}{3}c^2$
1,2,3,4,5,6	c	$\frac{1}{9}$	
7,8,9,10,11,12,13,14,15	$\sqrt{3}c$	$\frac{1}{72}$	

Table 3.2: *Weights of D3Q15 LBGK*

of the kinetic equation 3.13 and a set of velocities, which define the neighborhood of a lattice node and the corresponding weight of its equilibrium distribution f^{eq}. The velocity field $\mathbf{u}(\mathbf{x}, t)$ of the Navier-Stokes equations is then given by 3.9, the pressure field is obtained by

$$p(\mathbf{x}, t) = \rho(\mathbf{x}, t)\frac{k_B T}{m} = \frac{c^2}{3}\rho(\mathbf{x}, t), \qquad (3.19)$$

the viscosity ν can be adjusted with the parameter τ or ω respectively

$$\nu = \frac{c^2}{3}(\tau - \frac{\Delta t}{2}) = \frac{c^2}{3}(\frac{1}{\omega} - \frac{1}{2})\Delta t, \qquad (3.20)$$
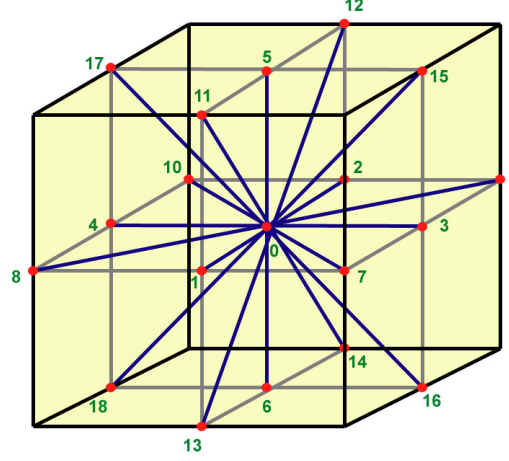
Figure 3.4: *The velocities $c_0 \ldots c_{18}$ of the D3Q19 lattice*

Index of $\mathbf{c}_i$	length of $\mathbf{c}_i$	Weights w_i	$k_B T/m$
0	0	$\frac{3}{9}$	$\frac{1}{3}c^2$
1,2,3,4,5,6	c	$\frac{1}{18}$	
7,8,9,10,11,12,13,14,15,16,17,18	$\sqrt{2}\ c$	$\frac{1}{36}$	

Table 3.3: *Weights of D3Q19 LBGK*

and the speed of sound c_s can be expressed as

$$c_s = \sqrt{\frac{dp}{d\rho}} = \frac{1}{\sqrt{3}}c. \qquad (3.21)$$

The LBGK methods have been derived by discretization of the Boltzmann equation and by a coarse approximation of the collision operator. In this section no proof has been done that this scheme can mimic the behavior of fluids. In the following section it will be shown that the presented LBGK methods actually approximate the Navier-Stokes equations with the pressure and viscosity from above, but as the Capman-Enskog expansion will reveal, only in the incompressible low Mach number limit.

3.2.3   Chapman-Enskog expansion

The Navier-Stokes equations can be derived from the Boltzmann equation by the Chapman-Enskog expansion. The multi scale expansion links statistical mechanics and fluid dynamics. In the discrete version the method is applied to the LBGK method deriving the incompressible Navier-Stokes equations in the low Mach number limit. For the sake of clarity external body forces have been neglected in the description of the LBGK method and in the multiscale expansion. For an expansion including external body forces the reader may refer to [54].

The main idea of the multiscale expansion is to pick out scales of interest. Three different spatial variations can be distinguished:

- Relaxation towards a local equilibrium (very fast, time scale ε^0)

- Sound waves and advection (normal, time scale ε^{-1})

- Diffusion (slow, time scale ε^{-2})

The Boltzmann equation describes the fluid on a mesoscopic scale, thus little spatial and short temporal scales (ε^0). The macroscopic description of the Navier-Stokes equations describes advection and diffusion. They act on different temporal scales (ε^1 and ε^2) but on the same spatial scale (ε^1). Therefore the following scaling is introduced:

$$
\begin{aligned}
t_0 & \quad \text{(discrete time step)} \\
t_1 = \varepsilon t_0 & \quad \text{(speed of sound and advection)} \\
t_2 = \varepsilon^2 t_0 & \quad \text{(diffusion)}
\end{aligned}
\tag{3.22}
$$

for temporal scales and

$$
\begin{aligned}
x_0 & \quad \text{(length of lattice node)} \\
x_1 = \varepsilon x_0 & \quad \text{(characteristic length scale of the flow)}
\end{aligned}
\tag{3.23}
$$

for spatial scales. Now the following scaling of the derivatives is applied:

$$
\begin{aligned}
\delta_t &\rightarrow \varepsilon \delta_t^{(1)} + \varepsilon^2 \delta_t^{(2)} \\
\delta_{x_\alpha} &\rightarrow \varepsilon \delta_{x_\alpha}^{(1)}.
\end{aligned}
\tag{3.24}
$$

This scaling neglects local relaxation processes. This contraction of the LBGK equation enables the recovery of macroscopic behavior and therefore the governing equations of fluid dynamics.

First the distributions $f_i(\mathbf{x}, t)$ are expanded around the equilibrium distributions $f^{eq}(\mathbf{x}, t)$ in the following way:

$$
f_i(\mathbf{x}, t) = f_i^{eq}(\mathbf{x}, t) + \varepsilon f_i^{(1)}(\mathbf{x}, t) + \varepsilon^2 f_i^{(2)}(\mathbf{x}, t) + O(\varepsilon^3)
\tag{3.25}
$$

with

$$
\begin{aligned}
\sum_i f_i^{(1)}(\mathbf{x}, t) = 0 \qquad & \sum_i c_i f_i^{(1)}(\mathbf{x}, t) = 0 \\
\sum_i f_i^{(2)}(\mathbf{x}, t) = 0 \qquad & \sum_i c_i f_i^{(2)}(\mathbf{x}, t) = 0,
\end{aligned}
\tag{3.26}
$$

thus $f_i^{(1)}$ and $f_i^{(2)}$ do not contribute to mass or moment but are only the derivation from the equilibria in the scales ε and ε^2. The parameter ε can be interpreted as the Knudsen number which is the ratio between mean free path length and the characteristic length scale of the flow. The parameter ε labels a perturbation of the equilibrium to a certain characteristic scale.

The kinetic equation is given by

$$
f_i(\mathbf{x} + \mathbf{c}_i \Delta t, t + \Delta t) = (1 - \omega) f_i(\mathbf{x}, t) + \omega f_i^{eq}(\mathbf{x}, t),
\tag{3.27}
$$

which is equivalent to 3.13. First the left hand side of the equation is ex-

panded into a Taylor series up to second order:

$$f_i(x + \mathbf{c}_i \Delta t, t + \Delta t) = f_i + \Delta t(\delta_t f_i + c_{i\alpha} \delta_{x_\alpha} f_i) +$$
$$\frac{1}{2} \Delta t^2(\delta_t^2 f_i + 2\delta_t c_{i\alpha} \delta_{x_\alpha} f_i + c_{i\alpha} c_{i\beta} \delta_{x_\alpha} \delta_{x_\beta} f_i) + O(\Delta t^3). \qquad (3.28)$$

Now the scaling of the partial derivatives 3.24 is inserted into equation 3.28. This leads to

$$f_i(x + \mathbf{c}_i \Delta t, t + \Delta t) = f_i +$$
$$\varepsilon \Delta t(\delta_t^{(1)} f_i + \varepsilon \delta_t^{(2)} f_i + c_{i\alpha} \delta_{x_\alpha}^{(1)} f_i) +$$
$$\varepsilon^2 \frac{1}{2} \Delta t^2(\delta_t^{(1)} \delta_t^{(1)} f_i + 2\varepsilon \delta_t^{(1)} \delta_t^{(2)} + 2\delta_t^{(1)} c_{i\alpha} \delta_{x_\alpha}^{(1)} f_i + \varepsilon \delta_t^{(2)} c_{i\alpha} \delta_{x_\alpha}^{(1)} f_i +$$
$$\varepsilon^2 \delta_t^{(2)} \delta_t^{(2)} f_i + c_{i\alpha} c_{i\beta} \delta_{x_\alpha}^{(1)} \delta_{x_\beta}^{(1)} f_i) + O(\Delta t^3). \qquad (3.29)$$

The expanded $f_i(\mathbf{x}, t)$ (equation 3.25) is inserted into 3.29. Sorted by ε up to second order this yields

$$f_i(x + \mathbf{c}_i \Delta t, t + \Delta t) =$$
$$\varepsilon^0 f_i^{eq} +$$
$$\varepsilon(f_i^{(1)} + \Delta t(\delta_t^{(1)} f_i^{eq} + c_{i\alpha} \delta_{x_\alpha}^{(1)} f_i^{eq})) +$$
$$\varepsilon^2(f_i^{(2)} + \Delta t(\delta_t^{(1)} f_i^{(1)} + \delta_t^{(2)} f_i^{eq} + c_{i\alpha} \delta_{x_\alpha}^{(1)} f_i^{(1)}) +$$
$$\frac{1}{2} \Delta t^2(\delta_t^{(1)} \delta_t^{(1)} f_i^{eq} + 2\delta_t^{(1)} c_{i\alpha} \delta_{x_\alpha}^{(1)} f_i^{eq} + c_{i\alpha} c_{i\beta} \delta_{x_\alpha}^{(1)} \delta_{x_\beta}^{(1)} f_i^{eq})) +$$
$$O(\varepsilon^3). \qquad (3.30)$$

Next the scaled Taylor expansion 3.30 is inserted into the kinetic equation 3.27 on the left hand side, on the right hand side the expanded distribution function 3.25 is inserted. The scaled kinetic equation then takes the form

$$0 = \varepsilon E_i^{(0)} + \varepsilon^2 E_i^{(1)} + O(\varepsilon^3) \qquad (3.31)$$

with

$$
\begin{aligned}
E_i^{(0)} \quad &:= \quad \delta_t^{(1)} f_i^{eq} + c_{i\alpha} \delta_{x_\alpha} f_i^{eq} + \frac{\omega}{\Delta t} f_i^{(1)} \\
E_i^{(1)} \quad &:= \quad \delta_t^{(1)} f_i^{(1)} + \delta_t^{(2)} f_i^{eq} + c_{i\alpha} \delta_{x_\alpha}^{(1)} f_i^{(1)} + \\
& \qquad \frac{\Delta t}{2} \left(\delta_t^{(1)} \delta_t^{(1)} f_i^{eq} + 2 \delta_t^{(1)} c_{i\alpha} \delta_{x_\alpha}^{(1)} f_i^{eq} + c_{i\alpha} c_{i\beta} \delta_{x_\alpha}^{(1)} \delta_{x_\beta}^{(1)} f_i^{eq} \right) + \\
& \qquad \frac{\omega}{\Delta t} f_i^{(2)}.
\end{aligned} \tag{3.32}
$$

From this representation of the scaled kinetic equation the macroscopic equations of fluid dynamic can be obtained by taking the zeroth and first moment of E_i in first order (describing advection) and second order (describing diffusion) of ε. The zeroth moments yield macroscopic equations about density ρ, the second moments about the fluid's moment $\mathbf{j}$:

$$
\begin{aligned}
\sum_i E_i^{(0)} \quad &\rightarrow \quad \text{continuity equation} \\
\sum_i \mathbf{c}_i E_i^{(0)} \quad &\rightarrow \quad \text{Euler equations} \\
\sum_i E_i^{(1)} \quad &\rightarrow \quad \text{no mass diffusion} \\
\sum_i \mathbf{c}_i E_i^{(1)} \quad &\rightarrow \quad \text{momentum diffusion} \\
&\Rightarrow \quad \text{Navier-Stokes equations}
\end{aligned} \tag{3.33}
$$

From the zeroth moment of $E_i^{(0)}$ (first order in ε), the compressible continuity equation is derived:

$$
\begin{aligned}
0 = \sum_i E_i^{(0)} \quad &= \quad \sum_i \delta_t^{(1)} f_i^{eq} + c_{i\alpha} \delta_{x_\alpha} f_i^{eq} + \frac{\omega}{\Delta t} f_i^{(1)} \\
&= \quad \delta_t^{(1)} \rho + \delta_{x_\alpha}^{(1)} j_\alpha + 0 \\
&= \quad \delta_t \rho + \nabla \cdot \mathbf{j}.
\end{aligned} \tag{3.34}
$$

The sum is calculated using the conservation of mass and moment of f_{eq} given in 3.15. The conservative properties of the equilibrium density function will be frequently used in the following calculations. In the incompressible limit $\delta_t \rho$ can be neglected, yielding the incompressible continuity equation

$$0 = \nabla \cdot \mathbf{u}. \tag{3.35}$$

From the first moment of $E_i^{(0)}$ (first order in ε), the Euler equations are obtained by

$$
\begin{aligned}
0 &= \sum_i c_{i\alpha} E_i^{(0)} \\
&= \sum_i c_{i\alpha} (\delta_t^{(1)} f_i^{eq} + c_{i\beta} \delta_{x_\beta} f_i^{eq} + \frac{\omega}{\Delta t} f_i^{(1)}) \\
&= \delta_t^{(1)} j_\alpha + \delta_{x_\beta}^{(1)} \Pi_{\alpha\beta} + 0
\end{aligned}
\tag{3.36}
$$

with the momentum flux tensor (see chapter 2.1.5, equation 2.40)

$$\Pi_{\alpha\beta} = \frac{1}{\rho} j_\alpha j_\beta + p \delta_{\alpha\beta}. \tag{3.37}$$

For the calculation of the momentum flux tensor the structure of the equilibrium function is needed, see 3.14. Therefore the momentum flux tensor takes the form

$$
\begin{aligned}
\Pi_{\alpha\beta} &= \sum_i c_{i\alpha} c_{i\beta} f_i^{eq} \tag{3.38} \\
&= \sum_i c_{i\alpha} c_{i\beta} \frac{w_i}{\rho_0} (\rho + \frac{m}{k_B T} \mathbf{c}_i \cdot \mathbf{j} + \frac{m}{2\rho k_B T} (\frac{m}{k_B T} (\mathbf{c}_i \cdot \mathbf{j})^2 - \mathbf{j}^2)).
\end{aligned}
$$

Four sums arise:

1.

$$\frac{\rho}{\rho_0} \sum_i c_{i\alpha} c_{i\beta} w_i = \rho \frac{k_B T}{m} \delta_{\alpha\beta} \tag{3.39}$$

The sum is calculated using the definition of the weighting factors w_i in 3.17.

2.

$$\frac{1}{\rho_0}\frac{m}{k_BT}\sum_i c_{i\alpha}c_{i\beta}(\mathbf{c}_i\cdot\mathbf{j})w_i = \frac{1}{\rho_0}\frac{m}{k_BT}j_\gamma\sum_i c_{i\alpha}c_{i\beta}c_{i\gamma}w_i = 0 \quad (3.40)$$

Note that on the right hand side the summation convention applies to γ. The sum vanishes because it is an odd sum in $\mathbf{c}_i$, see 3.17.

3.

$$\frac{1}{2\rho_0\rho}(\frac{m}{k_BT})^2\sum_i c_{i\alpha}c_{i\beta}(\mathbf{c}_i\cdot\mathbf{j})^2 w_i =$$
$$\frac{1}{2\rho_0\rho}(\frac{m}{k_BT})^2 j_\gamma j_\delta\sum_i c_{i\alpha}c_{i\beta}c_{i\gamma}c_{i\delta}w_i =$$
$$\frac{1}{2\rho}\sum_{\gamma,\delta} j_\gamma j_\delta(\delta_{\alpha\beta}\delta_{\gamma\delta}+\delta_{\alpha\gamma}\delta_{\beta\delta}+\delta_{\alpha\delta}\delta_{\beta\gamma}) =$$
$$\frac{1}{2\rho}(\mathbf{j}^2\delta_{\alpha\beta}+2j_{\alpha\beta}) \quad (3.41)$$

In the second line the summation convention applies to γ and δ, further the definition of the weighting factors w_i is used, see 3.17. The result can be easily obtained first by inserting $1\ldots D$ for α and β, where D is the spatial dimension, and then summing over γ and δ.

4.

$$\frac{1}{2\rho_0\rho}\frac{m}{k_BT}\mathbf{j}^2\sum_i c_{i\alpha}c_{i\beta}w_i = -\frac{1}{2\rho}\mathbf{j}^2\delta_{\alpha\beta} \quad (3.42)$$

The sum can be calculated using definition of the weighting factors w_i, see 3.17.

If the sums one to four are added together the momentum flux tensor (equa-

tion 3.37) is obtained, if the pressure term is set to

$$p = \rho \frac{k_B T}{m}, \tag{3.43}$$

thus LBGK fluids obey the ideal gas equation. Note that the momentum dependent part of the pressure term $\mathbf{j}^2 \delta_{\alpha\beta}$ in 3.41 and 3.42 cancels out. For this reason the terms of first order in ε yield in equation 3.34 and 3.36. In the incompressible limit these equations equal exactly the incompressible Euler equations:

$$\begin{aligned}
\nabla \cdot \mathbf{u} &= 0 \\
\frac{\delta}{\delta t}\mathbf{u} + (\mathbf{u} \cdot \nabla)\mathbf{u} &= -\frac{1}{\rho}\nabla p.
\end{aligned} \tag{3.44}$$

See section 2.1.5 for a physical interpretation of the macroscopic Euler equations and a derivation of its momentum flux tensor.

The terms of second order in ε give the dissipative terms (see 3.22) and will yield the Navier-Stokes equations in the low Mach number limit. First the zeroth moment of $E_i^{(1)}$ is investigated (second order in ε). This will show that there is no mass diffusion.

$$\begin{aligned}
0 &= \sum_i E_i^{(1)} \\
&= \sum_i \delta_t^{(2)} f_i^{eq} \\
&\quad + \frac{\Delta t}{2}(\delta_t^{(1)}\delta_t^{(1)} f_i^{eq} + 2\delta_t^{(1)}c_{i\alpha}\delta_{x_\alpha}^{(1)} f_i^{eq} + c_{i\alpha}c_{i\beta}\delta_{x_\alpha}^{(1)}\delta_{x_\beta}^{(1)} f_i^{eq})
\end{aligned} \tag{3.45}$$

Note that the terms $\sum_i \delta_t^{(1)} f_i^{(1)}$, $\sum_i c_{i\alpha}\delta_{x_\alpha}^{(1)} f_i^{(1)}$ and $\sum_i \frac{\omega}{\Delta t} f_i^{(2)}$ from $E_i^{(1)}$ vanish because of equation 3.26. Next it will be shown that the last term of the previous equation vanish, thus

$$\delta_t^{(1)}\delta_t^{(1)} \sum_i f_i^{eq} + 2\delta_t^{(1)}\delta_{x_\alpha}^{(1)} \sum_i c_{i\alpha} f_i^{eq} + \delta_{x_\alpha}^{(1)}\delta_{x_\beta}^{(1)} \sum_i c_{i\alpha}c_{i\beta} f_i^{eq} = 0. \tag{3.46}$$

To calculate the sums the temporal partial derivatives are substituted by spatial derivatives using equation 3.34 and 3.36:

$$\delta_t^{(1)}\delta_t^{(1)}\sum_i f_i^{eq} = \delta_t^{(1)}\delta_t^{(1)}\rho = \delta_t^{(1)}\delta_{x_\alpha}j_\alpha = \delta_{x_\alpha}^{(1)}\delta_{x_\beta}^{(1)}\Pi_{\alpha\beta}$$

$$2\delta_t^{(1)}\delta_{x_\alpha}^{(1)}\sum_i c_{i\alpha}f_i^{eq} = 2\delta_t^{(1)}\delta_{x_\alpha}^{(1)}(j_\alpha) = -2\delta_{x_\alpha}^{(1)}\delta_{x_\beta}^{(1)}\Pi_{\alpha\beta}$$

$$\delta_{x_\alpha}^{(1)}\delta_{x_\beta}^{(1)}\sum_i c_{i\alpha}c_{i\beta}f_i^{eq} = \delta_{x_\alpha}^{(1)}\delta_{x_\beta}^{(1)}\Pi_{\alpha\beta}. \tag{3.47}$$

Adding the sums together shows equation 3.46 and therefore

$$0 = \sum_i E_i^{(1)} = \sum_i \delta_t^{(2)}f_i^{eq} = \delta_t^2\rho, \tag{3.48}$$

expressing there is no mass diffusion.

The first moment of $E_i^{(1)}$ second order in ε yields the momentum diffusion of the Navier-Stokes equations in the incompressible low Mach number limit.

$$\begin{aligned} 0 &= \sum_i c_{i\alpha}E_i^{(1)} \\ &= \sum_i c_{i\alpha}\delta_t^{(2)}f_i^{eq} + c_{i\alpha}c_{i\beta}\delta_{x_\beta}^{(1)}f_i^{(1)} + \\ &\quad \frac{\Delta t}{2}(c_{i\alpha}\delta_t^{(1)}\delta_t^{(1)}f_i^{eq} + 2c_{i\alpha}c_{i\beta}\delta_t^{(1)}\delta_{x_\beta}^{(1)}f_i^{eq} + c_{i\alpha}c_{i\beta}c_{i\gamma}\delta_{x_\beta}^{(1)}\delta_{x_\gamma}^{(1)}f_i^{eq}) \end{aligned} \tag{3.49}$$

Again the terms $\sum_i c_{i\alpha}\delta_t^{(1)}f_i^{(1)}$ and $\sum_i \frac{\omega}{\Delta t}c_{i\alpha}f_i^{(2)}$ of $E_i^{(1)}$ vanish because of equation 3.26. The term $\sum_i c_{i\alpha}c_{i\beta}\delta_{x_\beta}^{(1)}f_i^{(1)}$ does not vanish but is rewritten in terms of the equilibrium distribution function f^{eq}. In the first order of ε equation 3.31 yields $E_i^{(0)} = 0$, thus with equation 3.32 the distribution function $f_i^{(1)}$ can be expressed as

$$f_i^{(1)} = -\frac{\Delta t}{\omega}\delta_t^{(1)}f_i^{eq} - \frac{\Delta t}{\omega}c_{i\alpha}\delta_{x_\alpha}^{(1)}f_i^{eq}. \tag{3.50}$$

When inserted into the first moment (second order in ε) this leads to

$$
\begin{aligned}
0 &= \sum_i c_{i\alpha} E_i^{(1)} \\
&= \sum_i c_{i\alpha} \delta_t^{(2)} f_i^{eq} + \frac{\Delta t}{2} c_{i\alpha} \delta_t^{(1)} \delta_t^{(1)} f_i^{eq} \\
&\quad + (\Delta t - \frac{\Delta t}{\omega}) c_{i\alpha} c_{i\beta} \delta_t^{(1)} \delta_{x_\beta}^{(1)} f_i^{eq} + (\frac{\Delta t}{2} - \frac{\Delta t}{\omega}) c_{i\alpha} c_{i\beta} c_{i\gamma} \delta_{x_\beta}^{(1)} \delta_{x_\gamma}^{(1)} f_i^{eq}
\end{aligned}
\tag{3.51}
$$

The occurring four sums are calculated:

1.

$$
\delta_t^{(2)} \sum_i c_{i\alpha} f_i^{eq} = \delta_t^{(2)} j_\alpha
\tag{3.52}
$$

2.

$$
\begin{aligned}
\frac{\Delta t}{2} \delta_t^{(1)} \delta_t^{(1)} \sum_i c_{i\alpha} f_i^{eq} &= \frac{\Delta t}{2} \delta_t^{(1)} \delta_t^{(1)} j_\alpha \\
&= -\frac{\Delta t}{2} \delta_t^{(1)} \delta_{x_\beta}^{(1)} \Pi_{\alpha\beta}
\end{aligned}
\tag{3.53}
$$

Where one temporal derivative is substituted with a spatial derivative using equation 3.36.

3.

$$
(\Delta t - \frac{\Delta t}{\omega}) \delta_t^{(1)} \delta_{x_\beta}^{(1)} \sum_i c_{i\alpha} c_{i\beta} f_i^{eq} = \Delta t (1 - \frac{1}{\omega}) \delta_t^{(1)} \delta_{x_\beta}^{(1)} \Pi_{\alpha\beta}
\tag{3.54}
$$

4.

$$
\begin{aligned}
(\frac{\Delta t}{2} - \frac{\Delta t}{\omega}) \delta_{x_\beta}^{(1)} \delta_{x_\gamma}^{(1)} \sum_i c_{i\alpha} c_{i\beta} c_{i\gamma} f_i^{eq} &= \\
\Delta t (\frac{1}{2} - \frac{1}{\omega}) \frac{m}{k_B T} \frac{1}{\rho_0} \delta_{x_\beta}^{(1)} \delta_{x_\gamma}^{(1)} \sum_i w_i c_{i\alpha} c_{i\beta} c_{i\gamma} (\mathbf{c}_i \cdot \mathbf{j}) & \\
\Delta t (\frac{1}{2} - \frac{1}{\omega}) \frac{m}{k_B T} \frac{1}{\rho_0} \delta_{x_\beta}^{(1)} \delta_{x_\gamma}^{(1)} j_\delta \sum_i w_i c_{i\alpha} c_{i\beta} c_{i\gamma} c_{i\delta} &
\end{aligned}
\tag{3.55}
$$

At this point the structure of the equilibrium function f^{eq} is used. Note that all terms except for the $(\mathbf{c}_i \cdot \mathbf{j})$ term vanish because they are odd moments of the weights w_i, see equation 3.17. When the fourth moment of w_i is inserted it yields

$$
\begin{aligned}
\Delta t(\frac{1}{2} - \frac{1}{\omega})\frac{k_B T}{m}\delta_{x_\beta}\delta_{x_\gamma} \sum_\delta j_\delta(\delta_{\alpha\beta}\delta_{\gamma\delta} + \delta_{\alpha\gamma}\delta_{\beta\delta} + \delta_{\alpha\delta}\delta_{\beta\gamma}) = \\
\Delta t(\frac{1}{2} - \frac{1}{\omega})\frac{k_B T}{m}(\delta_{x_\beta}\delta_{x_\beta}j_\alpha + 2\delta_{x_\alpha}\delta_{x_\beta}j_\beta) = \\
\Delta t(\frac{1}{2} - \frac{1}{\omega})\frac{k_B T}{m}(\nabla^2\mathbf{j} + 2\nabla(\nabla \cdot \mathbf{j})).
\end{aligned} \tag{3.56}
$$

First sum two and sum three are added together and following approximation is done:

$$
\begin{aligned}
(2) + (3) &= \Delta t(\frac{1}{\omega} - \frac{1}{2})\delta_t\delta_{x_b}\Pi_{\alpha\beta} \\
&\approx \Delta t(\frac{1}{\omega} - \frac{1}{2})\frac{k_B T}{m}\delta_t\delta_{x_b}\rho\delta_{\alpha\beta}.
\end{aligned} \tag{3.57}
$$

The approximation neglects terms of order $\mathcal{O}(\mathbf{j}^2)$. As a consequence the Navier-Stokes equations are only recovered in the low Mach number limit. Again the temporal derivation is substituted with spatial derivation (see equation 3.34):

$$
\begin{aligned}
(2) + (3) &\approx \Delta t(\frac{1}{\omega} - \frac{1}{2})\frac{k_B T}{m}\delta_t\delta_{x_\beta}\rho\delta_{\alpha\beta} \\
&= -\Delta t(\frac{1}{\omega} - \frac{1}{2})\frac{k_B T}{m}\delta_{x_\beta}\delta_{x_\alpha}j_\alpha \\
&= -\Delta t(\frac{1}{\omega} - \frac{1}{2})\frac{k_B T}{m}\nabla(\nabla \cdot \mathbf{j}).
\end{aligned} \tag{3.58}
$$

Putting everything together this yields the momentum diffusion of the Navier-

Stokes equations:

$$
\begin{aligned}
(1) &= [(2) + (3)] + (4) \\
\delta_t^{(2)}\mathbf{j} &= \Delta t(\frac{1}{\omega} - \frac{1}{2})\frac{k_B T}{m}(\nabla^2\mathbf{j} + \nabla(\nabla \cdot \mathbf{j})).
\end{aligned}
\tag{3.59}
$$

The Navier-Stokes equations are obtained by combining the first and second order terms of ε, thus 3.34, 3.36 and 3.59 yield:

$$
\begin{aligned}
\delta_t\mathbf{u} + (\mathbf{u} \cdot \nabla)\mathbf{u} &= -\frac{1}{\rho}\nabla p + \nu\nabla^2\mathbf{u} \\
\nabla \cdot \mathbf{u} &= 0,
\end{aligned}
\tag{3.60}
$$

when density fluctuations can be neglected, with the pressure

$$
p = \rho\frac{k_B T}{m},
\tag{3.61}
$$

the corresponding speed of sound c_s

$$
c_s = \sqrt{\frac{dp}{d\rho}} = \sqrt{\frac{k_B T}{m}}
\tag{3.62}
$$

and the viscosity

$$
\nu = \frac{k_B T}{m}(\frac{1}{\omega} - \frac{1}{2})\Delta t = \frac{k_B T}{m}(\tau - \frac{\Delta t}{2}).
\tag{3.63}
$$

Note that $k_B T/m$ is dependent of the lattice velocities $\mathbf{c}_i$, in the cases discussed in the last section D2Q9, D3Q15 and D3Q19 the value is given by

$$
\frac{k_B T}{m} = \frac{c^2}{3},
\tag{3.64}
$$

and the velocity $c = \Delta x/\Delta t$ is dependent of spatial and temporal resolution, see 3.18.

3.3   Implementation

One of the big advantages of the LBGK method is that its implementation is relatively simple. Nevertheless there are different approaches implementing the method, each of them having different advantages. In this section first the implementation of the kinetic equation and the splitting of its operator is discussed. Next the most common data structures for LBGK simulations are presented and finally the methods ability of parallelization is examined.

3.3.1   Splitting of the collision operator

LBGK schemes can be implemented very efficiently because of their explicit nature. The pseudo code for the LBGK method can be formulated as

```
while(running) {
  for each node {
      calculate kinetic equation
  }
  for each node {
      calculate local equilibria
  }
}
```

First the structure of the kinetic equation will be discussed. The kinetic equation (in analogy to equation 3.12) is given by

$$f_i(\mathbf{x} + \mathbf{c}_i, t + 1) - f_i(\mathbf{x}, t) = -\frac{1}{\tau}(f_i(\mathbf{x}, t) - f_i^{eq}) \qquad (3.65)$$

The operator can be split into a collision step and a streaming step in the following way:

$$
\begin{aligned}
f^*(\mathbf{x}, t) &= (1 - \frac{1}{\tau})f_i(\mathbf{x}, t) + \frac{1}{\tau}f_i^{eq} \\
f_i(\mathbf{x} + \mathbf{c}_i, t + 1) &= f^*(\mathbf{x}, t).
\end{aligned}
\qquad (3.66)
$$

This splitting of the operator is called collide-and-stream update order. The operator could as well be split into stream-and-collide update order.

For the knowledge of the equilibrium density distribution $f_i^{eq}(\rho, \mathbf{j})$ only the node itself is required, no neighboring nodes are needed. The density ρ and moment $\mathbf{j}$ can be calculated with the aid of equation 3.9, the equilibrium is given in 3.14 and the weighting factors w_i can be found in the tables 3.1, 3.2 and 3.3 for D2Q9, D2Q15 and D2Q19 respectively.

Every step in the LBGK algorithm is very simple. Nevertheless the optimal low level implementation on certain CPUs is a hard task because the CPU cache must be used in an optimal way. A detailed work about optimization of computer codes for LBGK schemes can be found in [55] and with particulary regard to parallelization of the LBGK method in [56].

3.3.2   Data structures for LBGK schemes

For the implementation of the LBGK method an adequate data structure is needed to store the densities, equilibria and information about neighborhood. Basically there are three approaches for the representation of the data:

- The simplest approach is to store all states in a lattice. Two lattices are needed. In one time step the new values are calculated from lattice A to lattice B, in the following time step from B to A and so on, see figure 3.5c. There is no need to store extra information about neighborhood because the position of the data in the lattice and therefore the position in memory is known.

- A major drawback of the method with lattices is when small structures lie in a big volume, like arteries in tissue. Most of the nodes are boundary nodes and there is only a small percentage of fluid nodes that actually must be processed. The idea is to calculate and store only relevant nodes. Relevant nodes are fluid nodes and no-slip nodes

	D2Q9		D3Q15	
	int[n]	references	int[n]	references
Lattice	0	0	0	0
List	8*n	0	15*n	0
Objects	0	8*n	0	8*n
double[n]	$9 + 9 + 3 = 21$		$15 + 15 + 4 = 34$	

Table 3.4: *Storage demand in two and three dimensions using three different approaches*

neighboring fluid nodes. The data of the relevant nodes are written in a list. Two sets of states are needed, old states and new states. In addition extra information about neighborhood is needed, see figure 3.5a. Thus the indices of the neighbors must be stored in an extra table for each node in the list.

- A more intuitive but slightly slower and more storage demanding approach is to represent every node as an object. The states are stored within the object. Neighborhood is realized by storing the references to the neighbors, see figure 3.5b. The object oriented approach simplifies experiments with new node types. When feasible node types are found, a faster implementation can be favored.

Independently of the chosen approach every time step has a complexity of $O(n)$. The storage demands of the different approaches are listed in table 3.4. The required double values are the same for all three methods. In D2Q9 three and in D3Q15 four doubles per node are needed to store the density and velocity for the local equilibria.

The LBGK D2Q9 and LBGK D3Q15 methods have been implemented in Java and were tested on one to four processors. The algorithm scales nearly linear. A discussion of parallelization and an example with the D3Q15 method are presented in the following section.
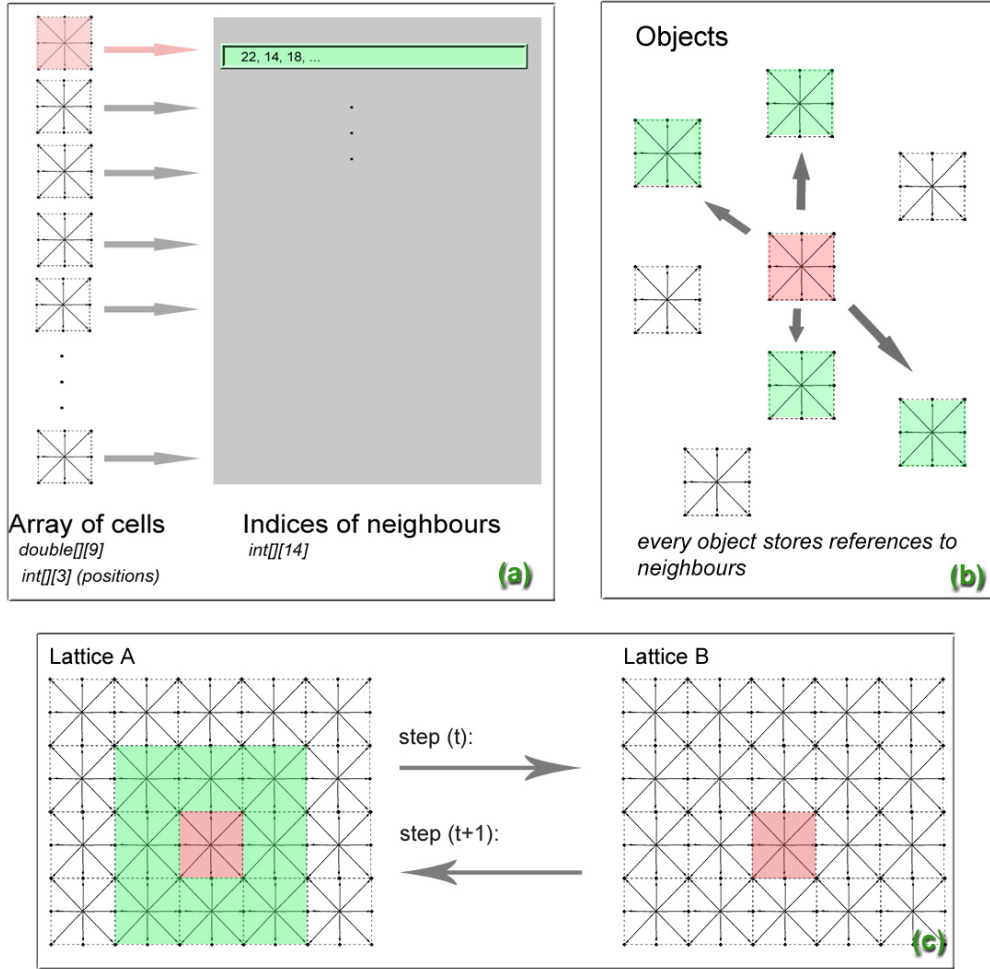
Figure 3.5: *Three different representations of the data needed for the D3Q15 LBGK computation*

3.3.3 Parallelization of LBGK schemes

A great advantage of the LBGK method is its simple parallelization, which is possible due to the strictly local nature of the method. Considering CPUs with multiple cores this property is of increasing importance.

To adjust the method for multiple threads the set of nodes must be distributed on the processors. In each calculated time step the threads must

wait for each others two times.

```
while(running) {
  for each thread {
        calculate kinetic equation for all nodes
  }
  wait for all threads
  for each thread {
        calculate equilibrium for all nodes
  }
  wait for all threads
}
```

The example models are boxes of 20*20 nodes with a length of 20, 100 and 200 nodes. The boxes are surrounded with no-slip nodes describing the walls, see section 4.1.1. At the top and bottom of the box a boundary condition describes the time dependent pressure gradient. The results of the simulation are in best accordance with the analytic solution by Womersley, see 2.2.4.

The simulation is done on a Dell Precision 670 containing two Intel Xeon dual core processors with 2.8 GHz with Windows XP SP2 and J2SE 5 Update 7. Time is measured over 100 time steps. The simulation is done 20 times on one to four processors. The run times are compared to the calculation time of one processor. Thus ideally two processors should work exactly with twice the performance as one. The blue line in the following plots is the regression line of all sample points, the red line is the regression line of all points except the three worst results.

Simulation of the box with 20*20*20 nodes: The smallest experiment with only 8000 nodes works very well and scales nearly linear. Eye catching is that two CPUs have more than twice the performance than one CPU, see figure 3.6(a). An explanation for this behavior can be found looking at computer layout. When two threads are used they run on the cells of only one CPU, while the second CPU can serve the operation system. The threads on the
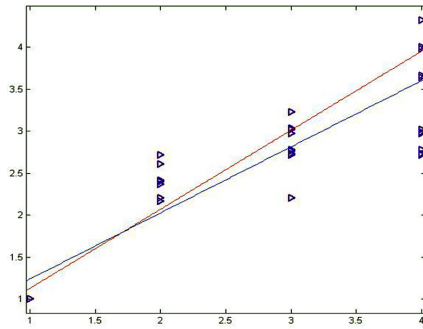
(a) *8000 nodes*
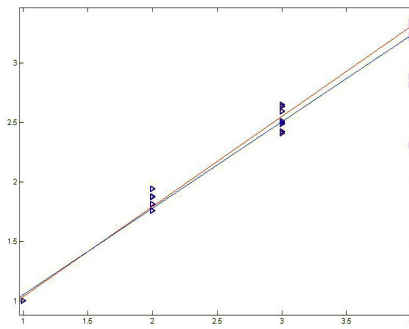
(b) *20000 nodes*
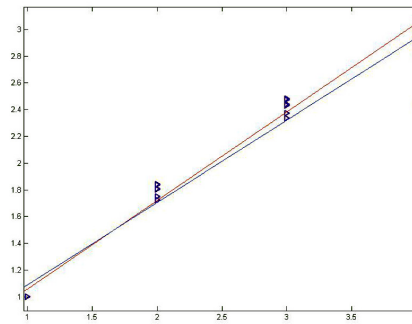
(c) *40000 nodes*

***Figure 3.6:** Simulation run times for using one to four cores*

two cells can use the cache in an optimal way. This small example shows that four threads are able to solve the problem four times faster than only one thread.

Simulation of the box with 20*20*50 nodes: The slightly bigger example with 20000 nodes shows a different behavior. In this case the simulation time is longer, thus more influences from the operation system can affect the simulation. Further performance is lost because the cache usage is not as good as in the smaller model. This results in slower simulation times than in the first example. Four threads are only three times faster than one thread, see figure 3.6(b).

Simulation of the box with 20*20*100 nodes: The biggest example with 40000
nodes shows similar behavior than the model with 20000 nodes. Four threads
have nearly the same performance as three threads, see figure 3.6(c). The
reason for this is that system services take a lot of time from one processor
and therefore all other threads have to wait.

Chapter 4

LBGK schemes applied to hemodynamics

In the previous chapter an explicit scheme has been presented to calculate the Navier-Stokes equations numerically. Main focus of this section is to point out how LBGK schemes can be applied to hemodynamics. Therefore feasible boundary conditions must be developed. Special care is taken of the treatment of elastic vessel walls and it is shown that the LBGK method can be used with the Reynolds and Womersley numbers relevant for blood flow simulation.

LBGK schemes have been successfully applied to arterial blood flow simulation [57]. Using the LBGK method has two main benefits: The first is the simplicity and the explicit nature of the method, which enables an easy implementation and parallelization. In two spatial dimensions interesting observations have been made investigating shear stress patterns in bifurcations [58] and the influence of stenosis [59]. The second benefit is that LBGK schemes work on a cartesian lattice. Generally this is a drawback, but when geometry is obtained from tomographic methods every voxel is simply assigned to a corresponding lattice node. This simplifies the process of data acquisition. Some experiments have been performed by A. M. M. Artoli, who simulated the flow in the abdominal aorta in [60] and [61].

4.1   Boundary Conditions

S. Chen et al. [62] state that achieving self-consistent boundary conditions with a given accuracy is to a certain degree as important as developing numerical schemes themselves.

A strong advantage of the LBGK method is that the state variables of the algorithm have a physical interpretation. For this reason boundary conditions can be developed in intuitive and heuristic way.

4.1.1   Elementary boundary conditions

S. Succi differences between elementary and complex boundary conditions [48]. Elementary boundary conditions are those where the boundary is aligned with the grid coordinates. Complex boundaries are more accurate than the grid, as a result the boundaries lie between the lattice nodes. In this work elementary boundary conditions are more important than complex boundary conditions, because the surface is obtained from tomographic images and is represented by voxels. In the following section the most common elementary boundary conditions are discussed in detail, more information can be found in [63].

- No-slip

  The most important boundary condition in LBGK simulations is surely the no-slip boundary condition. It describes a rigid wall and uses the fact that near a wall there is a no-slip situation, thus direct at the wall the fluid's velocity is zero. This effect is achieved by simply reflecting every incoming distribution function f_i, thus

$$f_i(\mathbf{x}, t + 1) = f_{-i}(\mathbf{x}, t) \tag{4.1}$$

  where $-i$ denotes the index in the opposite direction of index i. A distinction is drawn between complete bounce back schemes, where the boundary is aligned at the lattice node, see figure 4.1(b), and half

(a) *Complete bounce back*   (b) *Half-way bounce back*
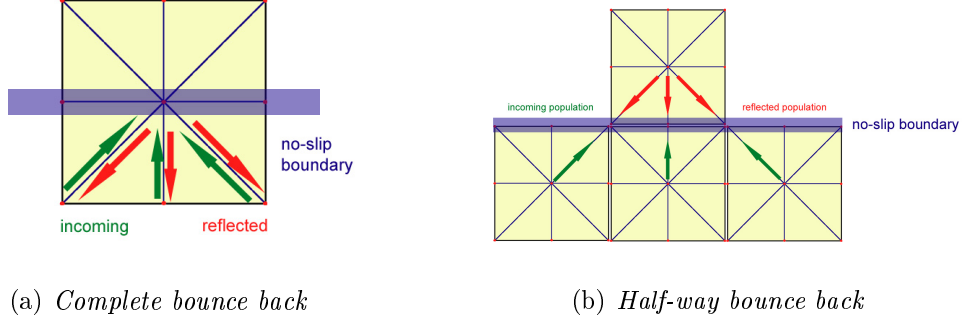
Figure 4.1: *Bounce back schemes*

way bounce back schemes, where the boundary is aligned between two lattice nodes, see figure 4.1(a).

- Periodic
  In many experiments periodic domains are useful, for example when fully developed flows in theoretically infinite tubes are under investigation, see section 2.2.3 and 2.2.4. Periodic boundary conditions can be implemented very easy:

$$
\begin{aligned}
f_i(\mathbf{x}_{in}, t+1) &= f_{-i}(\mathbf{x_{out}}, t) \qquad \text{and} \\
f_i(\mathbf{x}_{out}, t+1) &= f_{-i}(\mathbf{x_{in}}, t).
\end{aligned}
\tag{4.2}
$$

This rule applies to all indices i where the nodes $\mathbf{x}_{in}$ or $\mathbf{x}_{out}$ have no neighbors in direction $-\mathbf{c}_i$. Thus all outgoing distribution functions f_i^{out} are clued together with the corresponding incoming distribution functions f_i^{in} on the opposite side of the domain, see figure 4.2.

- Velocity and flow
  In blood flow simulation based on realistic data periodic boundary conditions often cannot be used. Instead of periodic boundary conditions in- and outflow profiles are predetermined. These profiles are not known and must be chosen in a realistic way. A simple approach how to choose the profiles will be discussed in the following section. When a velocity
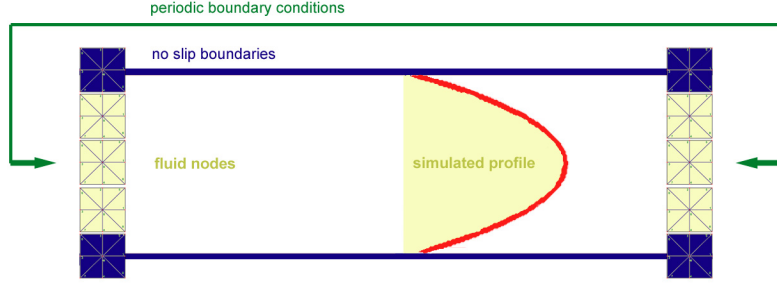
Figure 4.2: *Velocity profiles of unsteady flow*

profile is predetermined the distribution functions f_i^{in} are set to the equilibrium populations of the corresponding velocity profiles:

$$f_i^{in} = f_i^{eq}(\rho_0(\mathbf{x}, t), \mathbf{u}_0(\mathbf{x}, t)) \tag{4.3}$$

where $\rho_0(\mathbf{x}, t)$ is the density of f_i^{in}, if the domain is periodic or set to one if the boundary represents an in- or outflow.

- Pressure
  In LBGK simulations density and pressure have to be handled carefully. The problem is that the pressure p is linearly related to the density ρ with $p = \rho \frac{k_B T}{m}$. Since the flow is incompressible density fluctuations must stay negligible. The pressure gradient is a result of small density fluctuation on a density ρ_0. Nevertheless it can be useful to change the density of certain nodes to achieve a predetermined pressure. The nodes distribution functions can be updated in two ways, one is to conserve the nodes momentum:

$$f_i^{new}(\mathbf{x}_p, t) = f_i^{eq}(\rho_0(\mathbf{x}, t), 0), \tag{4.4}$$

the other one is to conserve the nodes velocity:

$$f_i^{new}(\mathbf{x}_p, t) = f_i^{eq}(\rho_0(\mathbf{x}, t), u(\mathbf{x}, t)). \tag{4.5}$$
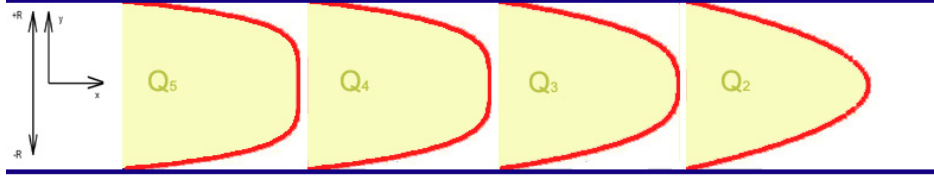
Figure 4.3: *Velocity profiles at an inlet* $N = \{5, 4, 3, 2\}$ *from left to right*

The boundary condition must be used in a way so that mass conservation is ensured. Over a certain time span the added density must equal the density that is removed from the lattice nodes.

In the following the in- and outflow boundary conditions for blood flow simulation are discussed in detail and a numerical validation of the proposed methods is presented. Furthermore a short summary of complex boundary conditions is given.

4.1.2   The in- and outflow of a vessel

The inflow boundary condition for the LBGK methods works very simple. In every discrete time step the inflow is set with the velocity boundary condition, see equation 4.3.

The difficult task is to choose the right velocity or flow profile. The velocity profiles for blood flow simulation can be obtained from analytical considerations. As derived in the sections 2.2.3 and 2.2.4 a fully developed laminar steady flow is called a Poiseuille flow and is given by:

$$u_z^P(r) = \frac{(R^2 - r^2)(P_1 - P_2)}{4\mu L} \tag{4.6}$$

and a fully developed laminar pulsatile flow is called a Womersley flow and is given by:

$$u_z^W(r, t) = \frac{A^c R^2}{i\mu\alpha^2} \left(1 - \frac{J_0(\alpha(r/R)i^{3/2})}{J_0(\alpha i^{3/2})} \right) e^{i\omega t}. \tag{4.7}$$

The two equations can be used to create realistic flows at the in- and outlets. The Poiseuille flow is used when steady flows are under investigation, whereas Womersley flow can be used when a dynamic model is calculated. A problem is that especially Poiseuille flow is often not fully established in realistic settings [4]. As a result the flow at the inlet has a flatter profile than the fully developed flow. This can be approximated with

$$u_z^{app}(r) = (R^N - r^N)c_0 \tag{4.8}$$

with a constant c_0 for scaling and $N \geq 2$, see figure 4.3.

The velocity profiles must be scaled to yield the predetermined flow $q(t)$ which can be a prediction from a coarser model of the cardiovascular system, see chapter 1.3.2. The influence of different choices of the inflow velocity profile to the overall simulation has been discussed in [64].

4.1.3 Numerical validation

For numerical validation of the method Poiseuille and Womersley flows, which have bee presented in section 2.2.3 and 2.2.4, have been simulated in two and three spatial dimension with lengths and velocities, which are relevant for blood flow simulation, thus with relevant Reynolds and Womersley numbers. The flow has been simulated in a rigid tube with a radius of 0.5 cm and a length of 5 cm. The relaxation parameter τ is chosen in a way that the simulated fluid has a viscosity of 0.04 Poise, which is a good approximation for the viscosity of blood.

Δx	Δt	speed of sound c_s	relaxation parameter τ (for 0.04 Poise)
0.1 cm	1E-4 s	577.35 cm/s	0.501202887
0.04 cm	1E-4 s	230.94 cm/s	0.52999788
0.02 cm	2E-5 s	577.35 cm/s	0.505996053

Table 4.1: *Parameters that are used for simulation of Poiseuille and Womersley flows.*
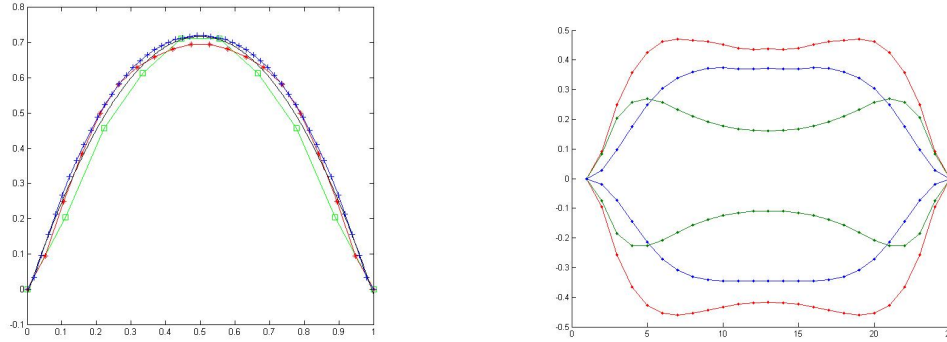
(a) *Poiseuille flow with node sizes: 0.1 cm (green), 0.04 cm (red), 0.02 cm (blue), exact (black)*

(b) *Womersley flow with node size 0.04 cm and equal time spacing $\frac{1}{6}$ s*

Figure 4.4: *LBGK D2Q9 solutions in a rigid tube*

For the Poiseuille flow a constant in- and outflow velocity of 10 cm/s has been predetermined. The flow has been calculated with different spatial resolutions, ranging from the size of 0.1 cm to 0.02 cm per lattice node, see table 4.1. The simulation results are in best agreement with the analytical solution, see figure 4.4(a) for two dimensions and figure 4.5 for three dimensions.

For the Womersley flow the pressure boundary condition has been used. A sinus shaped pressure gradient of 1 mmHg over a time period of 1 second has been applied. In figure 4.4(b) the results in two dimensions for a spatial resolution of 0.04 cm per lattice node are presented. In three spatial dimensions the flow profiles are plotted in figure 4.6.

4.1.4   Complex boundary conditions

Complex boundary conditions are those where the boundary is not aligned with the grid coordinates. Thus the boundary can be placed arbitrary within the lattice nodes. There are basically two different approaches to handle this situation:
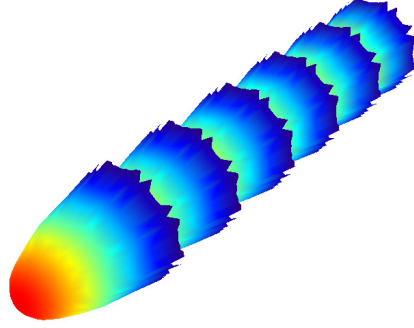
Figure 4.5: *Poiseuille flow: LBGK D3Q15 solution with node size 0.04 cm*
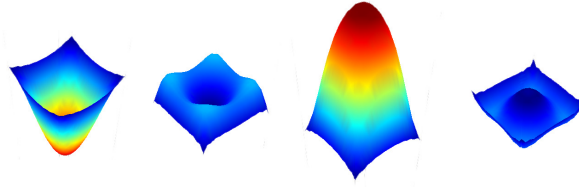
Figure 4.6: *Womersley flow: LBGK D3Q15 solution with node size 0.04 cm*

The first approach is to calculate the outgoing distribution functions f_i^{out} of the boundary node from the incoming distributions functions f_i^{in} according to the curved wall inside the node. Different methods have been proposed which in generally use extrapolation of the distribution densities, see R. Mei [65] [66] and R. Verberg [67] [68].

The second approach is to use grid refinement near the curved wall to increase the spatial resolution. The problem of this approach is that in LBGK schemes the temporal and spatial resolution are coupled. For this reason the LBGK method becomes a nested time scheme, thus the different lattices have different time steps Δt which increases the complexity of the implementation. A detailed description of the LBGK method with grid refinement can be found in [69] or [70].

4.2   Elasticity

In blood flow simulation it is important to consider the compliance of vessels. Therefore a boundary condition must be developed that describes the movement of the vessel wall in dependence of pressure. Fang et al. [71] have proposed a method which parameterizes the walls and uses a special treatment for curved boundaries. The method has been tested and successfully applied to pulsatile flow in two spatial dimensions [34].

The problem of this method is that the description of the vessel walls with the aid of surfaces is very complicated in three dimensions. The problem is comparable to the creation of feasible grids for FEM or FVM computation from tomographic images, which is avoided using the LBGK method. Thus using this method the simplicity and advantages of the LBGK method are partly lost. Therefore in this work a simpler approach is chosen [26], which does not require parameterized walls but works on the voxel representation of the geometrical domain.

4.2.1   Introduction

In the following method elasticity is basically described by displacement of voxels, which represents the boundary as a solid wall. The displacement is dependent of the local pressure in the surrounding nodes. Every boundary node has a fixed threshold. When the surrounding pressure exceeds this threshold the node is replaced by a fluid node. On the other hand if the surrounding pressure goes below a certain threshold the fluid node is replaced by a solid node. The boundary conditions are updated in every time step. Thus the method is a realization of the hemoelastic feedback system described by Fung in [35], see figure 4.7.

To avoid a rupture of the vessel wall a cellular automaton (CA) is used to update the walls in every time step. For more information about CA the reader may refer to [72]. The proposed method offers some advantages compared to the classical approach:
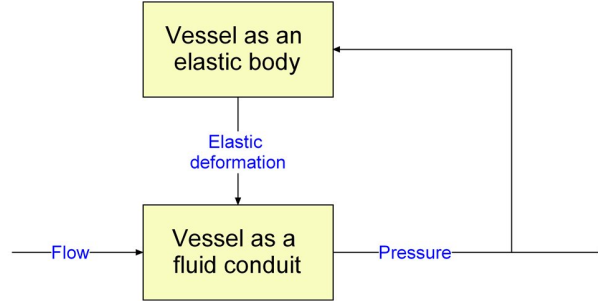
Figure 4.7: *A hemoelastic system analyzed as a feedback system of two functional units: an elastic body and a fluid mechanism [35]*

1. It avoids a surface representation of the geometrical domain but works directly on the voxel representation.

2. The method does not increase the complexity of the algorithm because it works strictly local like the LBGK method.

3. The approach enables a simple implementation in two and three dimensions.

In the following the steps of the algorithm are explained in more detail. First the representation of the volume with voxels is explained, next in which way the threshold values for the displacement are chosen and finally how the CA works which prevents rupture of the vessel wall.

4.2.2   Voxel representation

The geometrical data in the LBGK method are represented with the aid of voxels. The data structure that is used for the representation depends on the chosen implementation, see section 3.3. For simplicity it is assumed that the geometrical data are stored in a two or three dimensional array. This array works as a look up table for the fluid dynamical computation. Note that the CA will work on the geometrical data array containing the boundary conditions, while the LBGK method will use the look up array to check if boundary conditions have to be applied.
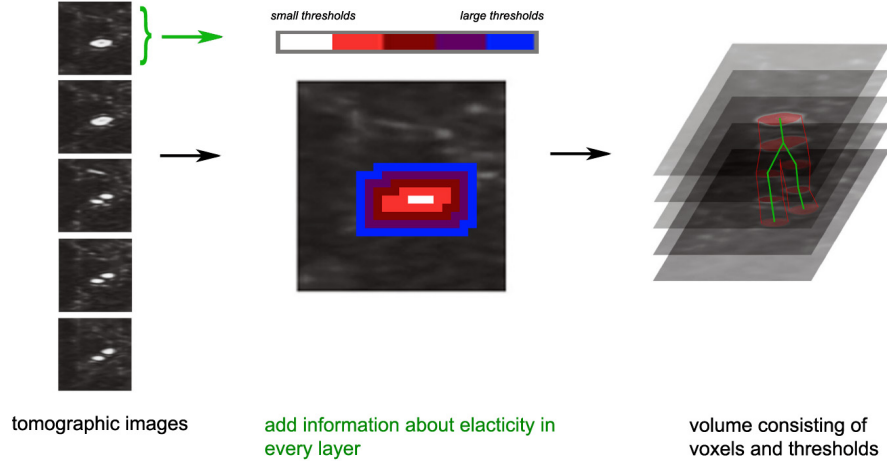
Figure 4.8: *Elastic boundaries are created from tomographic images*

When the vessel walls are considered to be rigid the layer of solid nodes that surrounds the fluid domain has a thickness of one. When elasticity is considered the layer of elastic nodes has to have the thickness of maximal circumference plus maximal narrowing. To set up the geometrical data in two dimensions is an easy task. Every solid node simply has to be replaced by a column of elastic nodes. In three dimensions more care must be taken when establishing the elastic layer.

In three dimensions the volume is created by binary segmentation from tomographic images, see section 5.1.1. The nodes inside the vessel are fluid nodes, the nodes describing the tissue are no-slip nodes. The elastic layer is built from this rigid layer in every cross section image, see figure 4.8. This is done in a recursive way. The nodes of the first layer are exactly the no-slip nodes which are neighbors to fluid nodes. The following layers consist of the no-slip nodes next to elastic nodes. When the cross section images are put together the resulting geometry has the desired elastic layer in three dimensions. The result is comparable to an onion skin. The outside layers

have large thresholds, which are descending moving inside the vessel. In the following section the choice of threshold values will be examined.

4.2.3 Identification of the threshold values

When the pressure is higher than a certain value the no-slip boundary condition shall be replaced by a normal fluid node and vice versa. In this section it is described in which way the threshold values can be assigned.

For the simulation a linear pressure radius relationship is assumed as presented in the end of section 2.2.3:

$$r(z) = r_0 + \alpha \frac{p(z)}{2}, \qquad (4.9)$$

where r_0 is the radius when the transmural pressure $p(z)$ is zero. The parameter α is a compliance constant, thus the threshold values are set to:

$$p(z) = \frac{2}{\alpha}(r(z) - r_0). \qquad (4.10)$$

The parameters r_0 and α must be chosen carefully. In two spatial dimensions the radius r_0 can be set to the distance of the wall to the center line. The compliance constant α can be calculated from the maximal extension of the vessel.

In three spatial dimensions the situation is more complicated because the center line is not known in advance. In the voxel representation of the geometrical data the elastic boundary layer has a certain predetermined thickness, which predefines the maximal expansion and maximal contraction of the vessel. Two values for pressure must be chosen, p_{max}, the pressure where the maximal expansion occurs and p_{min}, the pressure where the maximal

contraction occurs, thus

$$
\begin{aligned}
r_{max}(\mathbf{x}) - r_0 &= \alpha \frac{p_{max}(\mathbf{x})}{2} \quad \text{and} \\
r_{min}(\mathbf{x}) - r_0 &= \alpha \frac{p_{min}(\mathbf{x})}{2}.
\end{aligned}
\tag{4.11}
$$

From the two equations the values r_0 and α can be easily calculated and the thresholds for the elastic layer can be chosen accordingly.

4.2.4 Cellular Automaton for coherence of the vessel wall

The solid nodes are displaced when the pressure exceeds its threshold value. In this section a CA is developed to avoid rupture of the vessel wall introduced by this displacement process.

Note that the LBGK method and CAs are closely related. Historically LBGK schemes have even been developed from LGCA. The main difference between the two approaches is that the LBGK method has continuous state variables on its lattice nodes, while CA have discrete state variables in its cells. Appropriate update rules for the elastic walls boundary condition should therefore be strictly local and should have the same discretization in time and in the spatial domain as the LBGK model. The boundary conditions used by the LBGK method are normally defined in a separate lattice. This lattice can be interpreted as a CA with its own update rules which interact with the fluid dynamical model, see figure 4.9.

The CA has two different states, one is representing the fluid node and one is representing a no-slip boundary node as presented in section 4.1.1. The update rules of these states are divided into two steps:

In the first step the pressure $p_{ca}(\mathbf{x}, t)$ is compared to the threshold value t_p. If the nodes state is 'fluid' its pressure is used. If the node state is 'solid' the
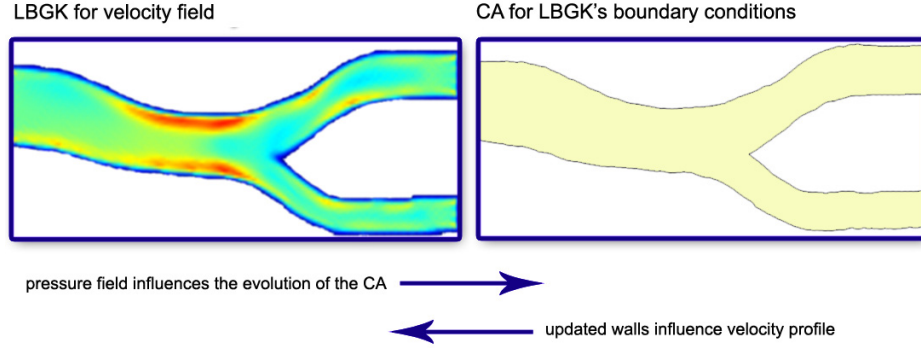
Figure 4.9: *The LBGK Model and the CA are discretized in the same spatial and temporal domain*

pressure of the neighboring fluid nodes are averaged, thus

$$p_{ca}(\mathbf{x}, t) = \begin{cases} p(\mathbf{x}, t) & \text{fluid node} \\ \frac{1}{\#f} \sum_{i=1}^{N} p(\mathbf{x} + \mathbf{c}_i, t) & \text{solid node,} \end{cases} \quad (4.12)$$

where value $\#f$ is the number of fluid nodes surrounding the solid node $\mathbf{x}$. The pressure $p(\mathbf{x}, t)$ of a solid node is defined to be zero. The value N is four in two dimensions and six in three dimensions corresponding to the four and six neighbors of the Neumann neighborhood. Every node $\mathbf{x}$ in the CA has a certain threshold value t_p which is chosen according to the previous section. The boolean value P_{ca} is introduced:

$$P_{ca}(\mathbf{x}, t) = \begin{cases} 1 & p_{ca}(\mathbf{x}, t) \geq t_p \\ 0 & p_{ca}(\mathbf{x}, t) < t_p. \end{cases} \quad (4.13)$$

The cells state is set to 'fluid node' if $P_{ca}(x, t) = 1$ and set to 'solid node' if $P_{ca}(x, t) = 0$.

In the second step the following rotational symmetric scheme is applied in two dimensions, see figure 4.10. The rules are chosen in a way that holes are closed, thus solid nodes diminish in fluid nodes and the other way around.
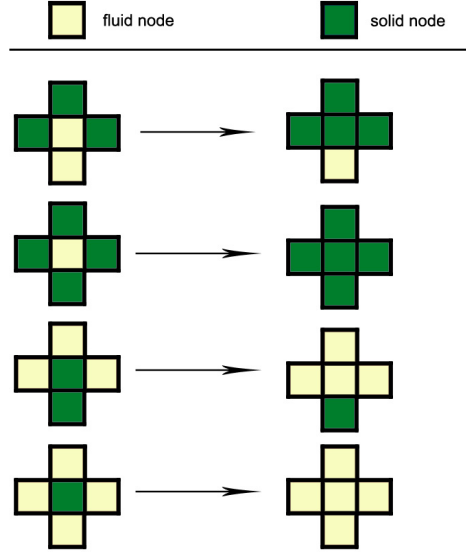
Figure 4.10: *Rules of the boundary conditions CA, the given rules are rotational symmetric*

In three spatial dimensions the rules are chosen in a similar way as in two dimensions. In general the method can be formulated as change of states when the following conditions are met:

$$\text{change from fluid to solid :} \qquad \sum_i^N P_{ca}(\mathbf{x}, t) < t_{fs}$$

$$\text{change from solid to fluid :} \qquad \sum_i^N P_{ca}(\mathbf{x}, t) > t_{sf} \qquad (4.14)$$

with $t_{fs} = 2$ and $t_{sf} = 2$ in two dimensions ($N = 4$) and $t_{fs} = 2$ and $t_{sf} = 4$ in three dimensions ($N = 6$).

When the LBM switches from 'solid node' to 'fluid node' the fluid node is set to $f^{eq}(\rho, \mathbf{u})$, where $\mathbf{u}$ is zero and ρ is determined on the basis of the threshold value t_x. This simple numerical scheme leads to the analytical behavior representing linear pressure radius relationship as introduced in section 2.2.3.

4.2.5 Numerical validation

In this section Poiseuille flow in an elastic tube will be investigated and the numerical results are compared with the analytical solution, see equation 2.76.

In two dimensions the flow field has been calculated in a tube of 2 cm length and a radius of 0.225 cm at a transmural pressure of 0 mmHg. A resolution of 400*70 nodes is used, thus one lattice node equals 0.01 mm^2. Between the inlet and the outlet a pressure gradient of 1 mmHg is applied. The elastic boundary conditions evolve to a steady state which is represented in figure 4.11(a). The radius $r(z)$ is plotted in figure 4.11(b). The simulated result is in good accordance with the analytical results that have been presented in section 2.2.3.

In three dimensions a rigid tube with 20 cm length and 2 cm radius at maximal expansion and a radius of 1.25 cm at transmural pressure of 0 mmHg is under investigation. This has been realized with a lattice of 40*40*200 nodes with a predetermined pressure gradient of 1 mmHg. Again a steady state evolves after a certain time. The three dimensional pressure and velocity is given in figure 4.12.

In this chapter it has been explained in which way the LBGK method can be applied to blood flow simulation. In the next chapter a software environment
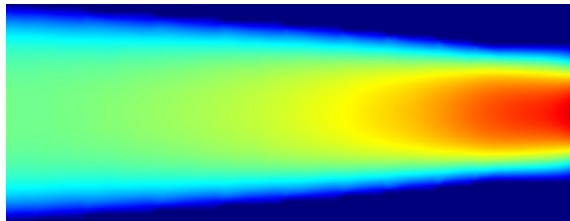
(a) *Velocity field in an elastic tube*
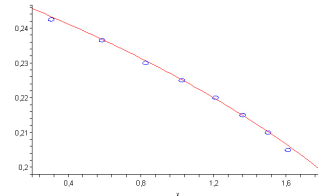
(b) *Analytical values $r(z)$ (line) and calculated values (circles)*

Figure 4.11: *An elastic tube in two dimensions*
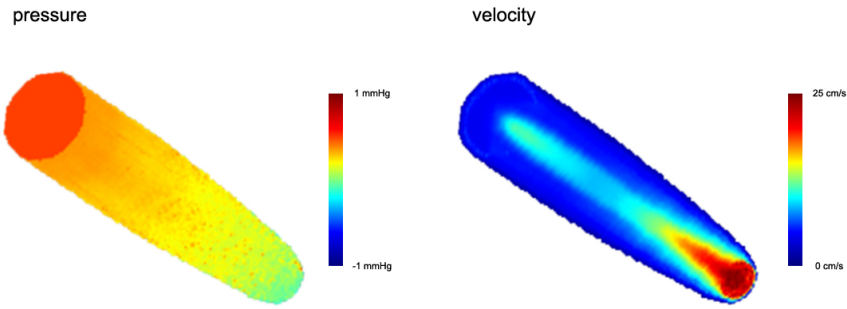
Figure 4.12: *Maximum intensity projection of velocity and pressure field in an elastic tube*

will be presented, which offers an implementation of the proposed methods. Further dynamic blood flow is investigated in selected case studies.

Chapter 5

Results

In this chapter the developed simulation environment is presented. Some of the single steps that are needed for simulating blood flow in three dimensions are examined in more detail. First the data acquisition and the creation of the cartesian lattice are explained, then the placement of time dependent boundary nodes and last the possibilities visualizing the results are demonstrated.

In the second part selected applications are investigated. First the effect of arteriosclerosis is examined in two dimensions. In three spatial dimensions flow through the abdominal aorta is simulated. Furthermore the influence of stenosis is demonstrated for different flow speeds and different magnitudes of the narrowing.

5.1 Computational Framework

The section explains important steps which have to be performed in blood flow simulation. The simulation of the flow field itself is not in scope of this section, selected examples will be presented in the next section. The methods and algorithms that are used in the following have been explained in the previous chapters.

5.1.1 Data acquisition

In three dimensional blood flow simulation geometrical boundaries can be obtained from magnetic resonance angiography. The geometric structure can be revealed by the use of paramagnetic contrast agents. The acquired data are cross section images and are normally stored in the DICOM format, which is widely used for medical applications. To import these images into Java programs they are first converted into JPG images.

The JPG images are imported into the software and a volume consisting of
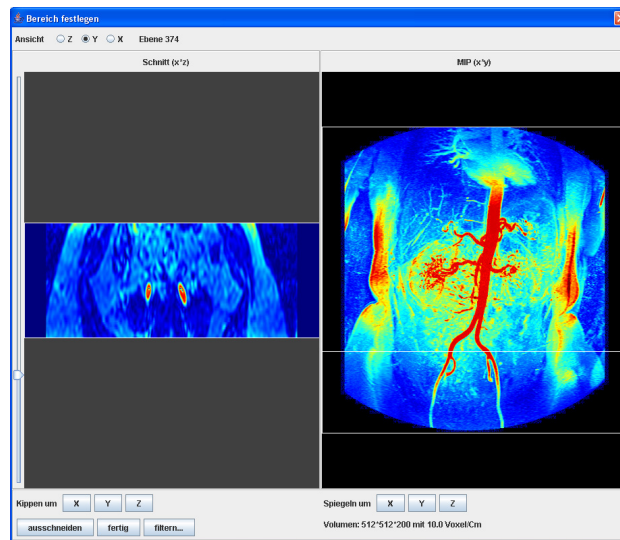
Figure 5.1: A cross section of the data (left) and a maximum intensity projection of the volume (right)
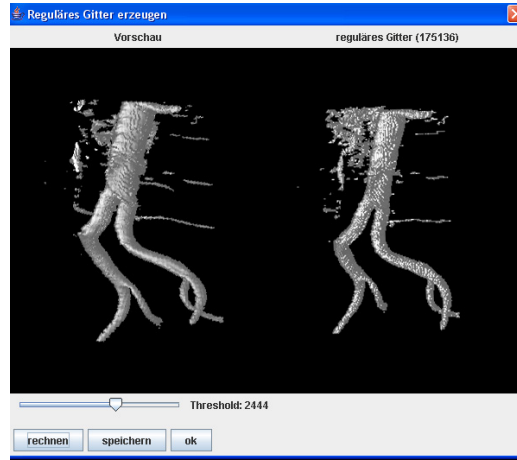
Figure 5.2: *The first hit projection of the volume (left) acts as a preview of the resulting lattice (right)*

voxels is created. Depending on the number of cross section images additional slices have to be created by interpolation. The result is a box consisting of voxels representing different densities. This volume can be visualized with a maximum density projection (MIP), see figure 5.1.

In the representation first the region of interest (ROI) is chosen by determining a rectangular domain, either in the cross section area on the left or in the MIP of the volume on the right, see figure 5.1. After this the volume is cropped to the ROI.

Finally a binary segmentation is performed. Every voxel is assigned to be solid or fluid in dependence of its density. If the density is above a certain threshold it is assigned to be 'fluid' otherwise it is assigned to be 'solid'. In figure 5.2 it is shown how the threshold value can be found. On the right side a first hit projection is used as a preview. When an adequate threshold value is chosen a cartesian lattice is created, in which only relevant nodes are stored. These nodes are fluid nodes and solid no-slip nodes, which have fluid nodes in their neighborhood.
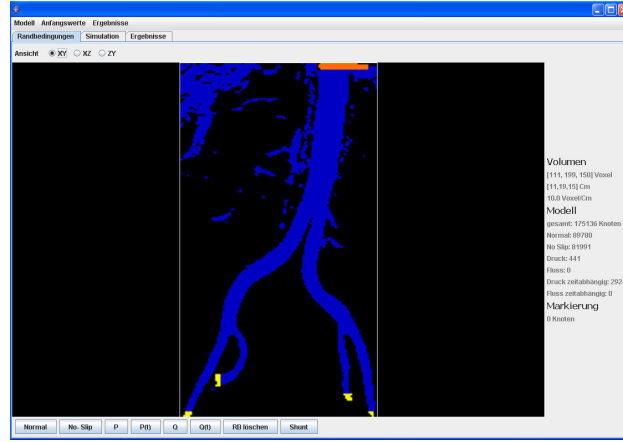
Figure 5.3: *Boundary nodes can be placed in the first hit projection of the segmented volume*

Geometrical artefacts are a common problem in blood flow simulation. There are basically two different approaches to remove artefacts:

1. A filter is applied to the volume before segmentation. Often the images contain numerical noise with high density. A low pass filter is a simple way to remove it.

2. After segmentation steady flow is simulated through the relevant fluid domain. All fluid nodes that have a velocity of zero are removed. In a second step all no-slip nodes with no fluid neighbors are removed. In practice this is a very powerful approach to remove both artefacts and vessels that can be neglected.

The two methods are normally sufficient to create feasible lattices for fluid dynamical computations.

5.1.2 Placing of boundary nodes

In section 4.1.1 the most common boundary conditions in the LBGK method have been presented. The different boundary conditions can be applied to
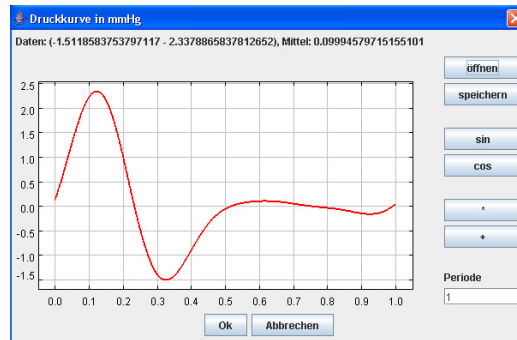
Figure 5.4: *A typical time dependent pressure gradient*

voxels that are selected in the first hit projection of the volume, see figure 5.3

The supported steady boundary conditions are:

- No-Slip

- Fixed pressure gradient

- Fixed flow,

and the time dependent boundary conditions are:

- Time dependent pressure gradient: The gradient can be chosen arbitrary, see figure 5.4. Particulary it can result from one dimensional global blood flow simulation or from measurements.

- Time dependent flow: Again a time dependent mean flow is chosen, from the mean flow different flow profiles can be created according to section 4.1.2.

Note that the elastic boundary condition cannot be placed but is created with the lattice, see section 4.2.

5.1.3 Visualization

For visualization of the simulation results different methods are used. During the calculation fast methods are needed. Simple direct volume visualization

techniques are applied to enable the user to get a quick impression of the running simulation. When the simulation is finished more elaborate methods can be used to visualize the results. Therefore the data under investigation are mapped to certain geometries and animation can be used to visualize time dependent velocity and pressure fields. In the following the implemented methods shall be summarized.

Direct volume visualization is used during simulation, the following ray casting techniques are applied:

- Maximum intensity projection: MIP maps the maximum value on a ray to a color. This is used to visualize velocity and pressure.

- First Hit Projection: When an intensity along a ray is higher than a certain threshold for the first time the intensity is mapped to a color. Additionally some lightning in dependence of the surrounding voxels can be introduced. First hit projection is used to visualize properties of the vessel wall like the wall shear stress.

The simulation results can be visualized with geometry based methods. The implementation uses Java3D, which is a scene graph based application programming interface on top of OpenGL:

- Animated particles: Particles like points, cubes or line segments float through the time dependent velocity field. The resulting animation is a very intuitive representation of the time dependent flow.

- Cross sections: Surfaces are used to visualize properties of cross sections along the main axis. This is the best way to visualize velocity or flow profiles in straight segments, see for example figure 4.5 or 4.6.

- Stream lines and Stream ribbons: They are a good way to visualize turbulence. A drawback is that the velocity field can only be visualized at a fixed time.

5.2   Case studies

In the following section selected case studies are presented. First the effect of atherosclerosis plaque on a flow field is investigated in two spatial dimensions with special focus on the time dependency of the flow. Next flow through the abdominal aorta is simulated in three dimensions with realistic in- and outflow boundary conditions, whereas the geometric boundaries are gained from tomographic images. Further the effect of stenosis is investigated in a three dimensional tube, where different mean velocities lead to different flow behavior.

5.2.1   Atherosclerosis

The following example is taken from [32] pp. 153-155. It describes the influence of atherosclerosis plaque to the dynamic flow field. The human abdominal aorta is simulated in two spatial dimensions, in which the geometric boundaries are taken from [73]. A two dimensional model with 35887 nodes is constructed and on the entrance of the flow a dynamic pressure gradient is predetermined, see figure 5.5(e).

The two dimensional flow fields are simulated over one cardiac cycle. Flow separation can occur behind the atherosclerotic plaque in the right common iliac artery, see 5.5 (red arrow). The colors denote the velocity of the flow field and the white lines represent the stream lines, which help to identify the region where the flow separation takes place.

Because of the dynamic pressure gradient the point and the size of the separation region varies with time. At the peak of the pressure gradient no flow separation occurs due to the acceleration of the fluid, see 5.5(a). In the next figure 5.5(b) the pressure gradient is zero. The fluid's mean velocity is higher than in figure 5.5(a) but the acceleration of the fluid is much smaller. For this reason strong flow separation occurs in figure 5.5(b) behind the red arrow. When the pressure gradient is on its minimum the flow collapses and therefore the velocities are very slow. As a result of the deceleration the flow

(a) *Peak of the pressure gradient*

(b) *Same pressure at entrance and exit*

(c) *Minimum of the pressure gradient*

(d) *Small pressure gradient during diastole*

(e) *Pressure gradient of the time dependent flow*
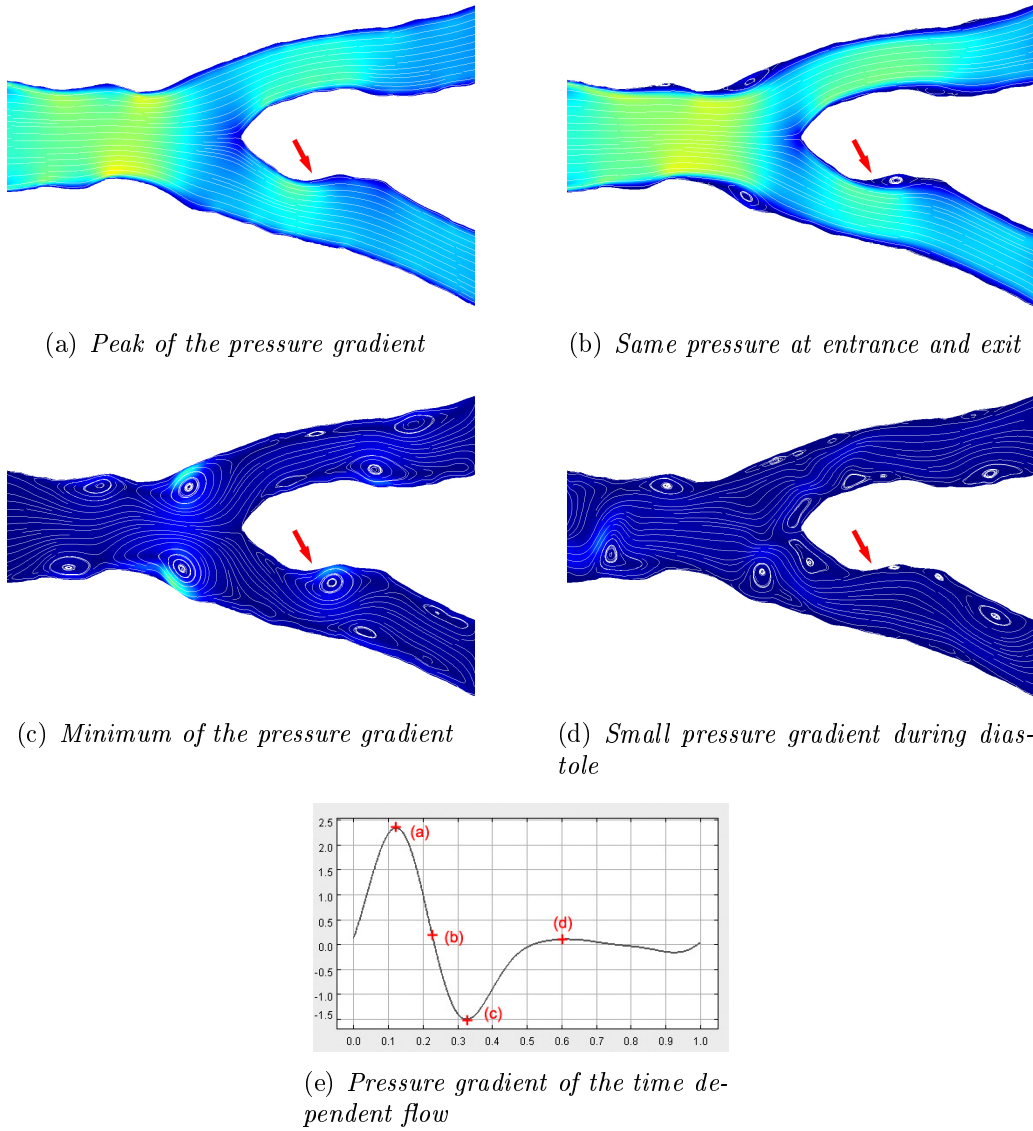
Figure 5.5: *Two dimensional flow in the abdominal aorta*

shows many eddies, see figure 5.5(c) which diminish during the diastole, see figure 5.5(d).

5.2.2 Abdominal Aorta

In three spatial dimensions the abdominal aorta is reconstructed from 50 images with a resolution of 512*512. After choosing the region of interest and removing artefacts with both methods described in 5.1.1 a lattice with 260451 nodes is obtained. The abdominal aorta lies in a bounding box of 13*27*14 cm^3.

(a) $t = 0.041\ s$ (b) $t = 0.124\ s$ (c) $t = 0.206\ s$

(d) $t = 0.329\ s$ (e) $t = 0.453\ s$ (f) $t = 0.576\ s$
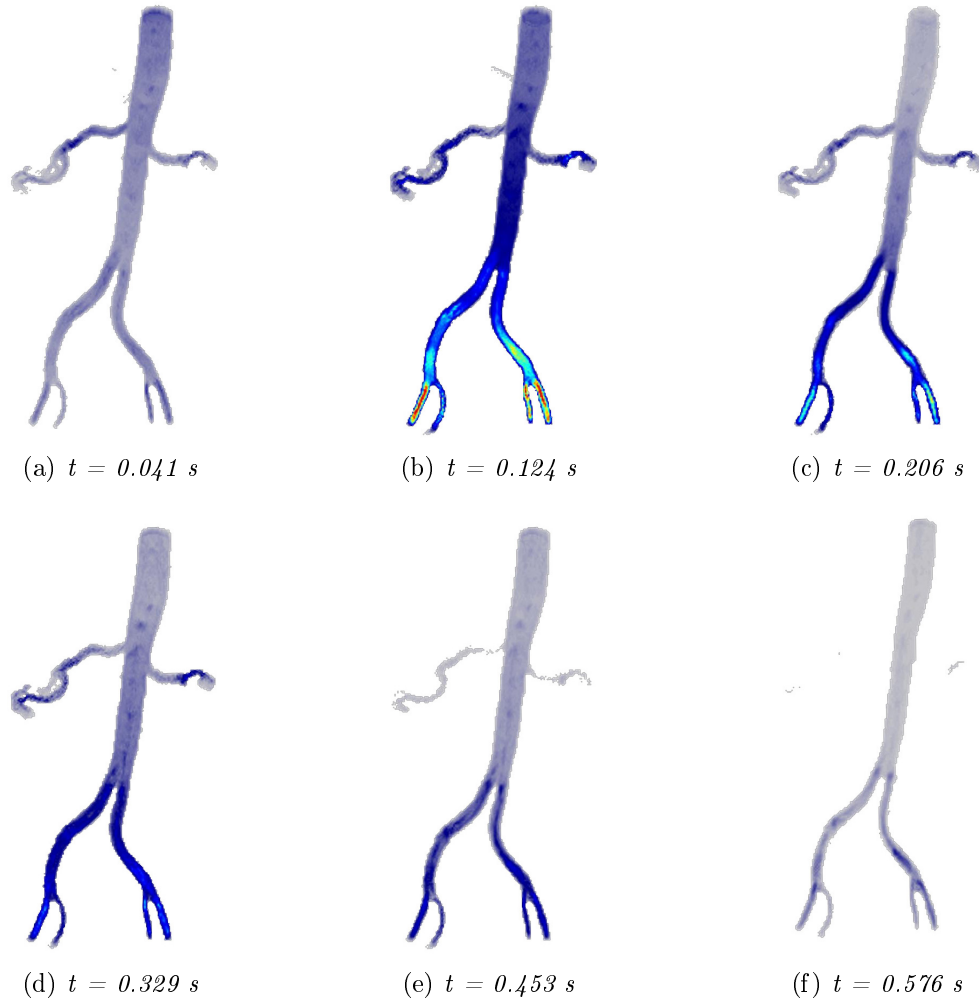
Figure 5.6: *Simulation of flow in the abdominal aorta during systole (upper row) and diastole (lower row)*

(a) *Cross sections above the above the bifurcation showing velocity profiles*

(b) *Stream lines showing vortex formation*
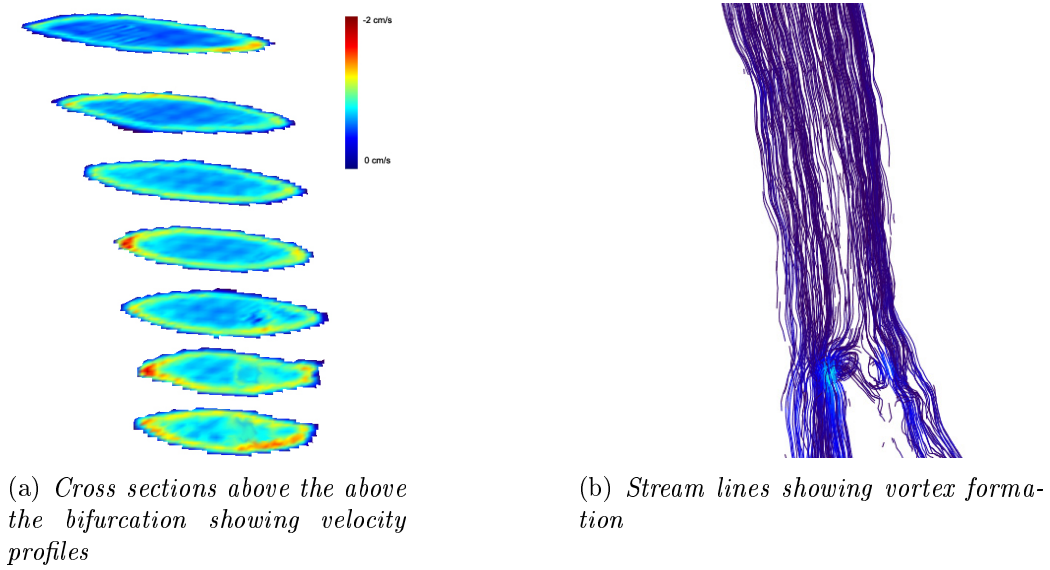
Figure 5.7: *The flow field in the abdominal aorta during diastole at t= 0.329*

At the inlet a pressure gradient is predetermined which has been taken from [4]. The resulting flow field is presented in figure 5.6 at different times during systole and diastole. During the systole high velocities can be observed in the right and left iliac due to the smaller radius of these arteries.

During the diastole two important properties can be observed: First their negative velocities appear, see figure 5.7(a). Second, due to the deceleration of the flow vortices occur, see 5.7(b). The results of the simulations show good agreements to the observations presented in [60], where a LBGK solver has been used on a realistic data set of an aorta.

5.2.3 Stenosis

The flow field in a stenosis is simulated. A tube with a radius of 3 cm and a length of 15 cm is approximated with 92262 nodes, every node has a size of 0.1 cm^3. In the middle of the tube is a narrowing reducing the radius to 2 cm over a length of 5 cm.
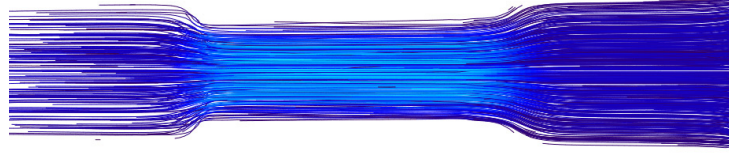
(a) *Mean velocity 0.8 cm/s, Re ≈ 60*
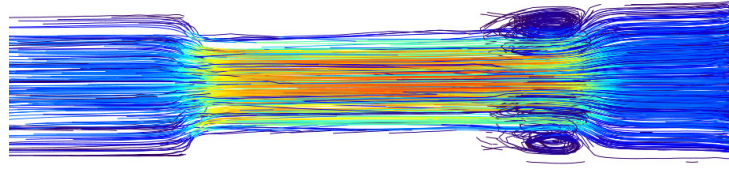
(b) *Mean velocity 4 cm/s, Re ≈ 300*
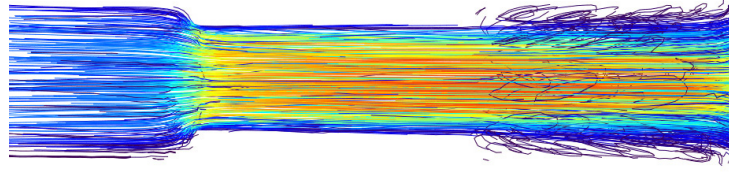
(c) *Mean velocity 8 cm/s, Re ≈ 600*

Figure 5.8: *Simulation of flow through a stenosis in three spatial dimensions*

Different mean velocities are predetermined, leading to different mean Reynolds numbers and therefore to different behavior of the flow, see figure 5.8. The flow with lowest mean velocity of 0.8 cm/s is represented in figure 5.8(a) and shows no flow separation. The size of the region of separation is dependent on the mean flow velocity. At a mean velocity of 4 cm/s the region of separation can clearly be identified, see figure 5.8(b). The region grows when the velocity is further increased, see 5.8(c) and can lead to turbulent behavior behind the narrowing.

In dynamic flow simulation stenosis can lead to eddies, which propagate through the vessels. Note that the narrowing leads to a massive pressure drop. This can be explained by the Poiseuille equation, see 2.2.3. Since mass transport has to stay constant, when the radius becomes smaller, the pressure gradient has to increase.

5.2.4 Conclusion

In this work a simulation environment has been developed which is able to simulate blood flow through arbitrary patient specific geometries. Tools for data acquisition as well as for postprocessing of simulation results have been presented. For calculating the flow numerically the LBGK method has been extended for a new type of boundary node supporting elastic vessel walls. A solver for two and three dimensional flow based on the LBGK method has been developed in Java working parallel on arbitrary multi-processor machines.

A drawback of the LBGK method is the coupling of spatial and temporal resolution, thus when the spatial resolution is increased time steps must be decreased. For an higher accuracy the software could be extended for grid refinement near the vessel walls. This approach would be very interesting in respect to the wall shear stress.

The LBGK method has proven to be feasible for hemodynamic calculations. The accuracy of the method is in good accordance to the accuracy of available boundary data like geometry, which is obtained from magnetic angiography, or pressure and velocities, which are obtained from in vivo measurements or global cardiovascular simulation. At the current resolution the method works very fast, in two spatial dimension it is even possible to calculate the fluid flow in realtime.

List of Figures

List of Tables

Bibliography

[1] Lippert H. *Lehrbuch Anatomie.* Texts in Applied Mathematics. Urban & Fischer, 5 edition, 2000.

[2] F. C. Hoppensteadt and C. S. Peskin. *Modeling and Simulation in Medicine and the Life Sciences.* Texts in Applied Mathematics. Springer, 2 edition, 2005.

[3] R. Klinke and S. Silbernagl. *Lehrbuch der Physiologie.* Thieme, Stuttgart, 4 edition, 2005.

[4] W.W. Nichols and M.F. O'Rourcke. *McDonald's blood flow in arteries.* Arnold, 4 edition, 1998.

[5] T.J. Pedley. *The fluid mechanics of large blood vessels.* Cambridge monographs on mechanics and applied mathematics. Cambridge Univ. Pr., 1 edition, 1980.

[6] A. Schermund and R. Erbel. New concepts of primary prevention require rethinking. *Med Klin*, 96:361–269, 2001.

[7] W. Rosamond, K. Flegal, G. Friday, K. Furie, A. Go, and al. Heart disease and stroke statistics - 2007 update: A report from the american heart association statistics committee and stroke statistics subcommittee. *Circulation*, 115(5):169–171, 2007.

[8] F. E. Cellier. *Continuous System Modeling.* Springer, 1 edition, 2006.

[9] F. E. Cellier and E. Kofman. *Continuous System Simulation.* Springer, 1 edition, 2006.

[10] F. Breitenecker and I. Troch. Development of modelling and simulation software - from basic time domain analysis to hybrid approaches and advanced event concepts. *Eurosim*, 2006.

[11] M.H. Song, M. Sato, and Y. Ueda. Three-dimensional simulation of coronary artery bypass grafting with the use of computational fluid dynamics. *Surgery Today*, 30(11):993–998, 2000.

[12] R. W. Alexander. Getting stents to go with the flow. *The Journal of Clinical Investigation*, 113(11):1532–1534, 2004.

[13] D. N. Ku, D. P. Giddens, C. K. Zarins, and S. Glagov. Pulsatile flow and atherosclerosis in the human carotid bifurcation. positive correlation between plaque location and low oscillating shear stress. *Arterioscler. Thromb. Vasc. Biol.*, 5:293–302, 1985.

[14] A. M. Shaaban and A. J. Duerinckx. Wall shear stress and early atherosclerosis: A review. *American Journal of Roentgenology*, 174:1657–1666, 2000.

[15] J. Suo, D. E. Ferrara, D. Sorescu, R. E. Guldberg, W. R. Taylor, and D. P. Giddens. Hemodynamic shear stresses in mouse aortas: Implications for atherogenesis. *Arterioscler. Thromb. Vasc. Biol.*, 27:346–351, 2007.

[16] V. K. Sud and G. S. Sekhon. Simulation of steady cardiovascular flow in the presence of stenosis using a finite element method. *Phys. Med. Biol.*, 35:947–959, 1990.

[17] M. S. Olufsen. Structured tree outflow condition for blood flow in larger systemic arteries. *Am J Physiol*, 276:H257–H268, 1999.

[18] M. S. Olufsen, C. S. Peskin, W. Y. Kim, E. M. Pedersen, A. Nadim, and J. Larsen. Numerical simulation and experimental validation of blood flow in arteries with structured-tree outflow conditions. *Annals of Biomedical Engineering*, 28(11):1281–1299, 2000.

[19] M. Suda. Die Computersimulation des arteriellen Kreislaufs als diagnostisches Instrument der Gefäßchirurgie: Endbericht. *OEFZS - Austrian Research Centers Seibersdorf*, 1995.

[20] M. Suda. Ein Computerprogramm zur Berechnung hydraulischer Transienten in komplexen Leitungssystemen. *GWF Wasser - Abwasser*, 128(7):371–378, 1987.

[21] Ch. Almeda. *Hydrodynamic Modelling and Simulation of the Human Arterial Blood Flow*. Number 8 in Fortschrittsberichte Simulation. ARGESIM Report, 2000.

[22] M. Wibmer. *Onedimensional simulation of the arterial blood flow with applications*. PhD thesis, Vienna University of Technology, 2003.

[23] J. Kropf. Dynamische Herzkreislaufsimulation unter Berücksichtigung verteilter Parameter. Master's thesis, Vienna University of Technology, 2002.

[24] J. Kropf. *Multiscale Blood Flow Simulation Concerning Various Termination Models*. PhD thesis, Vienna University of Technology, 2007.

[25] D. Leitner, J. Kropf, S. Wassertheurer, and F. Breitenecker. In F. H editor, *18th Symposium on Simulationtechnique ASIM 2005*.

[26] D. Leitner, S. Wasssertheurer, M. Hessinger, and A. Holzinger. A lattice boltzmann model for pulsative blood flow in elastic vessels. *Elektronik und Informationstechnik*, (4):152–155, 2006.

[27] D. J. Acheson. *Elementary Fluid Dynamics*. Oxford Applied Mathematics and Computer Science Series. Oxford University Press, 1990.

[28] L. Prandtl, K. Oswatitsch, and K. Wieghardt. *Führer durch die Strömungslehre*. Vieweg, 9 edition, 1942.

[29] R. L. Panton. *Incompressible Flow*. Wiley Interscience, 2 edition, 1996.

[30] R. Aris. *Vectors, Tensors and the Basic Equations of Fluid Mechanics.* Dover, 1989.

[31] P. Wesseling. *Principles of Computational Fluid Dynamics.* Springer Series in Computational Mathematics. Springer, 2001.

[32] Y.C. Fung. *Biodynamics. Circulation.* Springer, 1984.

[33] C. A. Taylor, T. J. R. Hughes, and C. K. Zarins. Finite element modeling of three-dimensional pulsatile flow in the abdominal aorta: Relevance to atherosclerosis. *Annals of Biomedical Engineering*, (26):975–987, 1998.

[34] A.G. Hoeksta, Jos van't Hoff, A.M.M. Artoli, and P.M.A. Sloot. Unsteady flow in a 2d elastic tube with the lbgk method. *Future Generation Computer Systems*, 20(6):917–924, 2004.

[35] Y.C. Fung. *Biomechanics, Mechanical Properties of Living Tissues.* Springer, 2 edition, 1993.

[36] J. R. Womersley. Oscillatory flow in arteries: Effect of radial variation in viscosity on rate of flow. *Journal of Physiology*, 127:38–39, 1955.

[37] J. R. Womersley. Method for the calculation of velocity, rate of flow and viscous drag in arteries when the pressure gradient is known. *Journal of Physiology*, 127:533–563, 1955.

[38] J. R. Womersley. Oscillatory flow in arteries: the constrained elastic tube as a model of arterial flow and pulse transmission. *Phys. Med. Biol.*, 2:178–187, 1957.

[39] L. A. Pipes. *Applied Mathematics for Engineers and Physicists.* McGraw-Hill, 3 edition, 1970.

[40] J. Puckmayr. Blutflussvisualisierung im Bereich medizinscher Lernsoftware. Master's thesis, Vienna University of Technology, 2004.

[41] M. Hessinger, A. Holzinger, D. Leitner, and S. Wassertheurer. Hemodynamic models for education in physiology. 2006.

[42] H Oertel and E. Laurien. *Numerische Strömungsmechanik.* Vieweg, 2 edition, 2003.

[43] U. Frisch, B. Hasslacher, and Y. Pomeau. Lattice- gas automata for the navier- stokes equation. *Phys. Revi. Lett.*, 56(14):1505–1508, 1986.

[44] G.R. McNamara and G. Zanetti. Use of the boltzmann equation to simulate lattice-gas automata. *Phys. Rev. Lett.*, 61(20):2332–2335, 1988.

[45] H. Babovsky. *Die Boltzmann Gleichung.* Teubner Verlag, 1998.

[46] Y. Sone. *Kinetic Theory and Fluid Dynamics.* Birkhäuser, 2002.

[47] F. Higuera and J. Jimenez. Boltzmann approach to lattice gas simulations. *Europhys. Lett.*, (20):663, 1989.

[48] S. Succi. *The Lattice Boltzmann Equation for Fluid Dynamics and Beyond.* Oxford University Press, 2001.

[49] P.L. Bhatnagar, E.P. Gross, and M. Krook. A model for collision processes in gases. i. small amplitude processes in charged and neutral one component system. *Phys. Rev. A.*, (94):511–525, 1954.

[50] P. Welander. On the temperature jump in rarefied gas. *Arkiv för Fysik,* 7(44):507–553, 1954.

[51] Y.H. Qian, D. D'Humières, and P. Lallemand. Lattice bgk models for navier-stokes equation. *Europhysics Letters*, 17:479–+, 1992.

[52] J.M.V.A Koelman. A simple lattice boltzmann scheme for navier-stokes fluid flow. *Europhysics Letters*, 15(6):603–607, 1991.

[53] Y.H. Qian and S.A. Orszag. Lattice bgk models for the navier-stokes equation: nonlinear deviation in compressible regimes. *Europhysics Letters*, 21:255–+, 1993.

[54] D.A. Wolf-Gladrow. *Lattice-Gas Cellular Automata and Lattice Boltzmann Models - An Introduction (Lecture Notes in Mathematics).* Springer, 2000.

[55] M. Kowarschik. *Data locality optimizations for iterative numerical algorithms and cellular automata on hierarchical memory architectures.* SCS Publishing House, 2004.

[56] J. Wilke, T. Pohl, M. Kowarschik, and U. Rüde. Cache performance optimizations for parallel lattice boltzmann codes. *Lecture Notes in Computer Science, LNCS*, 2790:441–450, 2003.

[57] J. M. Buick, J. A. Cosgrove, S.J. Tonge, A.J. Mulholland, B.A. Steves, and M.W. Collins. The lattice boltzmann equation for modelling arterial flows: review and application. *Biomedicine and Pharmacotherapy*, 56(7):345–346, 2003.

[58] A.M.M. Artoli, B.D. Kandhai, H.C.J. Hoefsloot, A.G. Hoekstra, and P.M.A. Sloot. Lattice bgk simulations of flow in a symmetric bifurcation. *Future Generation Computer Systems*, 20(6):909–916, 2004.

[59] H. Li, H. Fang, Z. Lin, S. Xu, and S. Chen. Lattice boltzmann simulation on particle suspensions in a two-dimensional symmetric stenotic artery. *Physical Review E*, 69(3), 2004.

[60] A.M.M. Artoli, A.G. Hoekstra, and P.M.A. Sloot. Mesoscopic simulations of systolic flow in the human abdominal aorta. *Journal of Biomechanics*, 39(5):873–884, 2006.

[61] A.M.M. Artoli. *Mesoscopic Computational Haemodynamics*. PhD thesis, University of Amsterdam, 2003.

[62] S. Chen, D. Martinez, and R. Mei. On boundary conditions in lattice boltzmann methods. *Physics of Fluids*, 8(9):2527–2536, 1996.

[63] S. Chen and G. D. Doolen. Lattice boltzmann method for fluid flow. *Rev. Fluid Mech*, 30:329–364, 1998.

[64] D. Leitner, J. Kropf, S. Wassertheurer, and F. Breitenecker. The inflow boundary condition in lbgk blood flow simulation. 2007.

[65] R. Mei, L.-S. Luo, and W. Shyy. An accurate curved boundary treatment in the lattice boltzmann method. *Journal of Computational Physics*, (155):307–330, 1999.

[66] R. Mei, L.-S. Luo, and W. Shyy. Lattice boltzmann method for 3-d flows with curved boundary. *Journal of Computational Physics*, (161):680–699, 2000.

[67] R. Verberg and A.J.C. Ladd. A lattice-boltzmann model with sub-grid scale boundary conditions. *Phys. Rev. Lett.*, 84:2148–2151, 2000.

[68] R. Verberg and A.J.C. Ladd. Accuracy and stability of a lattice-boltzmann model with sub-grid scale boundary conditions. *Phys. Rev. E*, 65(016701), 2001.

[69] O. Filippova and D. Hänel. Acceleration of lattice-bgk schemes with grid refinement. *J. Computational Physics*, 147(11), 2000.

[70] D. Yu, R. Mei, and W. Shyy. A multi-block lattice boltzmann method for viscous fluid flows. *Int. J. Numer. Methods Fluids*, 39(2), 2002.

[71] H. Fang, Z. Wang, Z. Lin, and M. Liu. Lattice boltzmann method for simulating the viscous flow in large distensible blood vessels. *Phys. Rev. E.*, 2001.

[72] S. Wolfram. *Cellular Automata and Complexity*. Westview, 1994.

[73] F. J. Walburn, H. N. Sabbah, and P. D. Stein. Flow visualization in a model of an atherosclerotic human abdominal aorta. *Journal of Biomechanical Engineering*, 103:168–170, 1981.

Curriculum Vitae

Name:	Johannes Daniel Leitner
Birth:	5th of January 1979, Salzburg
Nationality:	Austria
Address:	Blumauergasse 1c/3
	1020 Vienna

Education

since 2004	PhD studies at Vienna University of Technology, collaboration with Austrian Research Centers, Biomedical Engineering
10/2004	Master of Science
2003 - 2004	Academic term at the University of Groningen (Netherlands) within the scope of Socrates/Erasmus program for student mobility
1997 - 2004	Technical Mathematics, branch of study: Computer science at Vienna University of Technology
6/1997	Matura
1989 - 1997	High school in Salzburg
1985 - 1989	Elementary school in Salzbug

Professional Experience

2005 - 2006	Teaching Assistent at Vienna University of Technology, Institute for Analysis and Scientific Computing
since 2004	Austrian Research Centers, Biomedical Engineering
2001	Developing of graphical algorithms for Brainbows Gmbh
1998 - 1999	Community service at MOHI, Salzburg

Publications

[1]   D. Leitner, S. Wasssertheurer, M. Hessinger, A. Holzinger: *"A Lattice Boltzmann Model for Pulsative Blood Flow in Elastic Vessels"*; Elektronik und Informationstechnik E & I, **123** (2006), 4; pp. 152-155.

[2]   D. Leitner, M. Blaickner, H. Hötzendorfer, S. Wassertheurer: *"Simulation of Tumor Growth with Cellular Automaton"*; BMT 2006, Zürich, Switzerland; in: Proc. CD.

[3]   D. Leitner,S. Wassertheurer, F. Breitenecker: *"Simulation of Tumor Growth with Cellular Automaton and Subsequent Modeling of Response to Radiation Therapy"*; ENMA 2006, Bilbao, Spain; in: International Conference on Engineering and Mathematics, 84-95809-26-5; pp. 183-188.

[4]   D. Leitner, M. Hessinger, A. Holzinger, S. Wassertheurer, F. Breitenecker: *"Parallel Computation in Blood Flow Simulation Using the Lattice Boltzmann Method"*; Simulation News Europe SNE, **16** (2006), 2; pp. 64-68.

[5]   D. Leitner, S. Wassertheurer, F. Breitenecker: *"A Lattice Boltzmann Model for Pulsative Blood Flow in Elastic Vessels"*; MATHMOD 2006, Vienna, Austria; in: ARGESIM Report; **30** (2006), 3-901608-30-3.

[6]   J.Wöckel, D. Leitner: *"Modelling Advertising Effects - A Hybrid Approach using ODEs and Cellular Automata"*; MATHMOD 2006, Vienna, Austria; in: ARGESIM Report; **30** (2006), 3-901608-30-3.

[7]   M. Moczydlowska, L. Lapinski, D. Leitner: *"A Matrix-oriented Approach to CA Modelling in ARGESIM Comparison C17 'SIR-type Epidemic´ with MATLAB"*; Simulation News Europe SNE, **16** (2006), 1; pp. -38.

[8]   N. Popper, H. Hötzendorfer, D. Leitner, F. Breitenecker: *"Classical ODE Modelling versus Cellular Automata Modelling of a SIR-type Epidemic"*; MATHMOD 2006, Vienna, Austria; in: ARGESIM Report; **30** (2006), 3-901608-30-3.

[9]   D. Leitner, J. Kropf, S. Wassertheurer, F. Breitenecker: *"Lattice Boltzmann Methode zur Simulation vom Strömungsverhalten in Arterien"*; ASIM 2005, Erlangen, Germany; in: Frontiers in Simulation - ASIM Fortschritte in der Simulationstechnik / SCS Publishing House, **18** (2005), 3-936150-41-9, pp. 768-773.

[10]   D. Leitner, J. Kropf, S. Wassertheurer, F. Breitenecker: *"Ein Lattice Boltzmann Modell zur Simulation von lokalem Blutfluss"*; ÖGBMT 2005, Innsbruck, Austria; in: Proc. CD.

[11]   D. Leitner: *"Segmentierung und Visualisierung von MR-Daten zur Modellierung des arteriellen Blutflusses"*; Master's Thesis. Vienna University of Technology, 2004.

Fields of Research

Biomedical Engineering, Numerical Modeling and Simulation, Fluid Dynamics, Biofluid Mechanics, Visualization, Java, Java3D, C/C++, OpenGl, Matlab

Languages

German (mother tongue), English (fluent)

Interests

Travel, Streetball, Music, Photography